Trinity College Dublin
Coláiste na Tríonóide, Baile Átha Cliath
The University of Dublin

Emissions and Energy Requirements of Current and Future Aircraft Operations

Author: Conor Gallagher

Supervisor: Dr. Charles Stuart

Department of Mechanical, Manufacturing & Biomedical Engineering

School of Engineering

Trinity College Dublin

The University of Dublin

A Thesis submitted in partial fulfilment of the requirements
for the degree of
Doctor of Philosophy

May, 2026

Declaration

I declare that this thesis has not been submitted as an exercise for a degree at this or any other university and it is entirely my own work. I confirm that the work has been completed in full compliance with relevant university policies, including the Academic Integrity policy, the Trinity Policy on Good Research Practice, and the guidance on AI and GenAI in Teaching, Learning, Assessment and Research.

I agree to deposit this thesis in the University's open access institutional repository or allow the Library to do so on my behalf, subject to Irish Copyright Legislation and Trinity College Library conditions of use and acknowledgement.

I consent to the examiner retaining a copy of the thesis beyond the examining period, should they so wish (EU GDPR May 2018).

Signed: Conor Gallagher Date: 20/05/2026

Abstract

Aviation faces significant challenges in achieving environmental objectives due to continued traffic growth and the complexity of reducing both CO_2 and non-CO_2 climate impacts. Existing aircraft performance and emissions assessments often rely on empirical modelling approaches and idealised design missions, limiting their applicability to future aircraft technologies and real-world airline operations. This thesis develops an integrated modelling framework that combines physics-based aircraft, propulsion, and combustion models with real-world airline operational data to enable robust, large-scale evaluation of aircraft energy use, emissions, and climate impacts.

The framework coupled physics-based aerodynamic and propulsion system models with surrogate modelling techniques to achieve computational efficiency suitable for simulating complete airline operating schedules. Real-world operational fidelity was introduced through reconstruction of flight missions from airline data, capturing variability in mission range and operating conditions. The framework was applied to evaluate aviation decarbonisation pathways, with a particular focus on liquid hydrogen and synthetic sustainable aviation fuels, using a fleet-wide operational case study for a short-haul European airline. Comparative analyses of hydrogen-powered configurations highlighted the importance of accurate aircraft performance modelling when analysing prospective designs, while variation in results from off-design missions reinforced the need to account for real-world operational behaviour.

As part of this modelling framework, physics-based methods for non-CO_2 emissions were developed using chemical reactor network models to predict NO_x, CO_2, and H_2O emissions as a function of engine operating condition. These models were integrated within the flight simulation framework and compared against conventional empirical approaches, demonstrating material differences in predicted emissions and associated climate impacts. The framework was further applied to assess the climate benefits of fleet renewal under realistic operational conditions, accounting for both near-term and long-term climate effects. The results show that fleet renewal can deliver substantial climate impact reductions, particularly for near-term warming, driven primarily by reductions in NO_x emissions. In addition, pathways for extending the framework towards physics-based contrail formation modelling were demonstrated.

The results demonstrate that operationally realistic, physics-based aircraft modelling can significantly alter the assessment of decarbonisation pathways and climate mitigation strategies compared to design-mission-based and empirical approaches. The modelling framework developed in this thesis provides a scalable and physically representative tool

for evaluating future aircraft technologies, fuels, emissions, and fleet transition strategies under real-world operating conditions.

Acknowledgements

I would like to express my sincere thanks to my supervisor, Dr. Charles Stuart, for his guidance, technical insight, and consistent support throughout the course of this research. His expertise and direction were instrumental in shaping the scope and quality of the work presented in this thesis. I am also grateful to my co-supervisor, Prof. Stephen Spence, for his valuable advice, constructive feedback, and support during the project.

Thank you to Ryanair for the financial and technical support of this study through the Sustainable Aviation Research Centre at Trinity College Dublin, along with the permission to use their data. In particular, I would like to thank Stephen Fitzgerald for his help in procuring data and providing technical support throughout the project.

Additional thanks are extended to Dr. Harry Smith and Dr. Dominic Barone for their technical assistance and valuable feedback during various stages of the research.

Finally, thank you to all my family, friends, and colleagues at Trinity College Dublin who supported me along the way.

Contents

List of Figures

List of Tables

Nomenclature

Abbreviations

AEA	All-Electric Aircraft
ANN	Artificial Neural Network
ASK	Available Seat Kilometres
ASTM	American Society for Testing and Materials
ATAG	Air Transport Action Group
AtJ	Alcohol-to-Jet
ATR	Average Temperature Response
ATR_{100}	100-year Average Temperature Response
B737-MAX	Boeing 737-8200 aircraft
B737-NG	Boeing 737-800NG aircraft
BEMT	Blade Element Momentum Theory
BFFM	Boeing Fuel-Flow Method
BLI	Boundary Layer Ingestion
BPR	Bypass Ratio
BWB	Blended-Wing Body
CASK	Cost per Available Seat Kilometre
CFD	Computational Fluid Dynamics
CG	Centre of Gravity
CoCiP	Contrail Cirrus Prediction Model
CRN	Chemical Reactor Network
DAC	Direct Air Capture
DLR	German Aerospace Center empirical NO_x prediction method
DZ	Dilution Zone
EDB	Emissions Databank
EDS	Environmental Design Space

EI	Emission Index
EIS	Entry Into Service
ERF	Effective Radiative Forcing
ETS	Emissions Trading System
EU	European Union
FAR	Fuel-Air Ratio
FEM	Finite Element Modelling
FLOPS	Flight Optimisation System
FPR	Fan Pressure Ratio
FRL	Fuel Readiness Level
FT	Fischer-Tropsch
GE	General Electric
GI	Gravimetric Index
GSP	Gas Turbine Simulation Programme
GTP	Global Temperature change Potential
GWP	Global Warming Potential
HEA	Hybrid-Electric Aircraft
HEFA	Hydrogenated Esters and Fatty Acids
HEX	Heat Exchanger
HPC	High-Pressure Compressor
HPT	High-Pressure Turbine
IC	Intercooled
ICAO	International Civil Aviation Organization
ICCT	International Council of Clean Transportation
IRE	Intercooled Recuperated Engine
ISSR	Ice Supersaturated Region
Jet A-1	Jet Fuel
LCOE	Levelised Cost Of Electricity
LES	Large Eddy Simulation
LH_2	Liquid Hydrogen
LNG	Liquefied Natural Gas
LPC	Low-Pressure Compressor
LPT	Low-Pressure Turbine
MAE	Mean Absolute Error

MAPE	Mean Absolute Percentage Error
MDAO	Multidisciplinary Design Analysis and Optimization
MDP	Multi-Design Point
MEA	More-Electric Aircraft
MLI	Multi-Layer Insulation
MRV	Monitor, Report and Verify
MTOW	Maximum Take-Off Weight
NEATS	Non-CO_2 Aviation Effects Tracking System
NM	Nautical Mile
NPSS	Numerical Propulsion System Simulation
nvPM	Non-volatile Particulate Matter
OEW	Operating Empty Weight
OPR	Overall Pressure Ratio
P2L	Power-to-Liquid
P3-T3	Pressure-Temperature empirical NO_x prediction method
PEM	Proton Exchange Membrane
PR	Pressure Ratio
PROOSIS	Propulsion Object Oriented Simulation Software
PSR	Perfectly Stirred Reactor
PtL	Power-to-Liquid
PZ	Primary Zone
QAR	Quick Access Recorder
RANS	Reynolds-Averaged Navier-Stokes
RC	Recuperated
RF	Radiative Forcing
RMSE	Root Mean Square Error
RPK	Revenue Passenger Kilometre
RQL	Rich-Quench-Lean
RTO	Rolling Take-Off
SAC	Schmidt-Appleman Criterion
SAF	Sustainable Aviation Fuel
SDP	Single-Design Point
SLS	Sea-Level Static
SMR	Steam-Methane Reforming

SOEC	Solid Oxide Electrolyser Cell
SUAVE	Stanford University Aerospace Vehicle Environment
SZ	Secondary Zone
TAPS	Twin-Annular Premixing Swirler
TASOPT	Transport Aircraft System Optimisation
TCT	Thermochemical Conversion Technologies
TLAR	Top-Level Aircraft Requirements
TOC	Top-Of-Climb
TOW	Take-Off Weight
TSFC	Thrust Specific Fuel Consumption
TTBW	Transonic Truss-Braced Wing
TtW	Tank-to-Wake
UDF	Unducted Fan
UHAR	Ultra-High Aspect Ratio
UHBPR	Ultra-High Bypass Ratio
UHC	Unburned Hydrocarbons
VLM	Vortex Lattice Method
WtT	Well-to-Tank
WtW	Well-to-Wake

Thermodynamic Variables

FAR	Fuel-air ratio	–
FAR_{st}	Stoichiometric fuel-air ratio	–
LHV	Lower heating value	$\mathrm{MJ\,kg^{-1}}$
$\dot{Q}$	Rate of heat transfer	kW
T	Static temperature	K
T_t	Total temperature	K
T_{t_1}	LPC inlet total temperature	K
T_{t_2}	LPC exit total temperature	K
T_{t_3}	HPC exit total temperature	K
T_{t_4}	Combustor exit total temperature	K
U_∞	Freestream velocity	$\mathrm{m\,s^{-1}}$
U_{out}	Exhaust velocity	$\mathrm{m\,s^{-1}}$

W_c	Compressor work	J
$\dot{W}$	Rate of work	kW
c_p	Specific heat at constant pressure	$\mathrm{J\,kg^{-1}\,K^{-1}}$
m	Mass	kg
$\dot{m}$	Mass flow rate	$\mathrm{kg\,s^{-1}}$
$\dot{m}_f$	Fuel mass flow rate	$\mathrm{kg\,s^{-1}}$
p	Static pressure	Pa
p_t	Total pressure	Pa
p_{t3}	Compressor exit total pressure	Pa
γ	Specific heat ratio	–
η_{th}	Thermal efficiency	–
η_{pr}	Propulsive efficiency	–
ρ	Density	$\mathrm{kg\,m^{-3}}$
ϕ	Equivalence ratio	–

Aircraft Performance

AR	Aspect Ratio	–
D	Drag	N
C_L	Lift coefficient	–
C_D	Drag coefficient	–
C_{D_0}	Zero-lift drag coefficient	–
C_{D_p}	Parasitic drag coefficient	–
$C_{D_{inviscid}}$	Inviscid drag coefficient	–
$C_{D_{total}}$	Total drag coefficient	–
C_f	Skin friction coefficient	–
C	Drag correction factor	–
E	Energy	MWh
L	Lift	N
L/D	Aerodynamic Efficiency	–
M	Mach number	–
S	Reference area	$\mathrm{m^2}$
T	Thrust	N
T/W	Thrust-to-Weight ratio	–

V_H	Horizontal tail volume coefficient	–
V_V	Vertical tail volume coefficient	–
W	Weight	N
W/S	Wing loading	–
b	Wing span	m
$\bar{c}$	Mean aerodynamic chord of the wing	m
e	Span efficiency	–
k	Induced drag factor	–
k_{fuse}	Fuselage form factor	–
k_{wing}	Wing form factor	–
l_H	Distance from CG to horizontal tail aerodynamic centre	m
l_V	Distance from CG to vertical tail aerodynamic centre	m
r	Radius of curvature	m
t/c	Thickness-to-chord ratio	–
θ	Flight path angle	deg
ϵ	Thrust misalignment angle	deg
Λ	Quarter-chord wing sweep	deg

Emissions

CH_4	Methane	kg
CO	Carbon monoxide	kg
CO_2	Carbon dioxide	kg
H_2O	Water vapour	kg
NO	Nitric oxide	kg
NO_2	Nitrogen dioxide	kg
NO_x	Nitrogen oxides	kg
nvPM	Non-volatile particulate matter	kg
O_{3L}	Long-lived Ozone	kg
O_{3S}	Short-lived Ozone	kg
PM	Particulate matter	kg
SO_2	Sulphur dioxide	kg
SO_4	Sulphate aerosols	kg
SO_x	Sulphur oxides	kg
UHC	Unburned hydrocarbons	kg

Hydrogen Aircraft Design

D_{ext}	External diameter	m
D_{int}	Internal diameter	m
D_h	Hydraulic diameter	m
G_{air}	Mass flux	$\mathrm{kg\,s^{-1}\,m^{-2}}$
L_x	HEX length in air-flow direction	m
V	Volume	$\mathrm{m^3}$
f	Friction factor	–
η_{grav}	Gravimetric efficiency	–
σ_{air}	Ratio of HEX free-flow to frontal area	–

CRN Parameters

A_g	Ignition pulse amplitude	–
A	Combustor cross-sectional area	$\mathrm{m^2}$
A_i	CRN reactor area ratio	–
AR_i	CRN reactor air ratio	–
FF_i	CRN reactor fuel-flow ratio	–
L	Combustor axial length	m
L_i	CRN reactor length ratio	–
$g(t)$	Gaussian ignition function	–
t_0	Ignition start time	s
τ	Ignition characteristic timescale	s

Climate Metrics

A_i	Radiative efficiency of species i	$\mathrm{W\,m^{-2}\,kg^{-1}}$
ATR	Average temperature response	K
ATR_{100}	100-year average temperature response	K
E	Emissions	kg
Eff_i	Efficacy of species i	–
ERF	Effective radiative forcing	$\mathrm{W\,m^{-2}}$
$G_T(t)$	Temperature impulse response function	–
$G_{\chi,\mathrm{CO_2}}$	$\mathrm{CO_2}$ impulse response function	–

H	Humidity correction factor	–
L	Distance flown in ice-supersaturated regions	km
RH	Relative humidity	–
RF	Radiative forcing	$\mathrm{W\,m^{-2}}$
RF^*	Normalised Radiative forcing	$\mathrm{W\,m^{-2}}$
p_{sat}	Saturation vapour pressure	Pa
$s_i(h)$	Altitude-dependent forcing factor for species i	–
t'	Year of emission event	years
α_j	CO_2 concentration coefficient	–
δ_{amb}	Ambient pressure ratio	–
$\delta_{amb,t}$	Total pressure ratio	–
θ_{amb}	Ambient temperature ratio	–
$\theta_{amb,t}$	Total temperature ratio	–
λ_i	Climate sensitivity of species i	$\mathrm{K\,W^{-1}\,m^2}$
τ	NO_x perturbation lifetime	years
τ_j	CO_2 response time coefficient	–
$\chi_{CO_{2_0}}$	Pre-industrial atmospheric CO_2 concentration	ppm
ω	Humidity ratio	–
$\Delta T(t)$	Surface temperature response	K
$\Delta\chi_{CO_2}$	Change in atmospheric CO_2 concentration	ppm

Chapter 1

Introduction

1.1 Context and Motivation

1.1.1 Societal Impact of Aviation

Aviation faces possibly the most difficult challenge of all sectors in terms of reducing its impact on global warming. Islands such as Ireland are in a unique position where there is no alternative to air travel in the context of the Flight-Path 2050 interconnectivity goals, which aim for a 4-hour door-to-door journey anywhere in Europe [1]. Inaction on aviation will further strain the country's ability to achieve European Union (EU) climate objectives, such as the 'Fit for 55' [2] targets for 2030, and the European goal of net-zero flights by 2050, as described in Destination 2050 [3]. These climate targets are set in the context of a growing aviation industry that could reach 10 billion passengers by 2050 [4], making the challenge more complex and the solution more urgent.

Ireland is a global player in the aviation sector, being the home of Europe's largest airline and the global hub of the aircraft leasing business (50% of the market share [5]). As a result, aviation plays a critical role in economic activity in Ireland. In 2019, Ireland's main airports employed 143,747 people, with the airports contributing €10.2 billion to the Irish economy, which represents 5.1% of the Gross National Income (GNI) and 3.5% of Gross Domestic Product (GDP) [6]. Since more than 90% of all travel to Ireland is by air [7], Ireland's tourism industry is highly dependent on aviation and is estimated to employ over 220,000 people [6]. The global impact of aviation is generally positive, as it provides substantial societal and economic value by enabling global connectivity, trade, and mobility, supporting activities aligned with 15 of the 17 United Nations Sustainable Development Goals [8]. However, the urgent need to address the imminent climatic crisis is the most significant challenge of our times.

1.1.2 Ryanair Sustainable Aviation Research Centre

This research forms part of a collaborative programme between Trinity College Dublin and Ryanair within the Ryanair Sustainable Aviation Research Centre. The overarching objective of this collaboration is to support the development of technically and economically viable pathways toward a more sustainable aviation sector, accounting for both carbon and non-carbon environmental impacts through the evaluation of advanced aircraft technologies, operational strategies, and alternative fuels. A key component of the collaboration is access to a substantial repository of real-world airline flight data provided by Ryanair, enabling modelling approaches that reflect actual operational behaviour rather than idealised mission assumptions.

Consequently, a central aim of this thesis is to identify and develop modelling frameworks capable of fully exploiting this operational data to assess the feasibility and system-level impacts of sustainable aviation technologies. In particular, the research focuses on quantifying both carbon and non-carbon emissions under realistic operating conditions, thereby providing insights that are directly relevant to airline decision-making and policy development. By grounding the analysis in real-world operations, the work seeks to bridge the gap between academic modelling studies and the practical challenges faced by commercial airlines in improving the environmental sustainability of their operations.

1.1.3 Energy Carriers

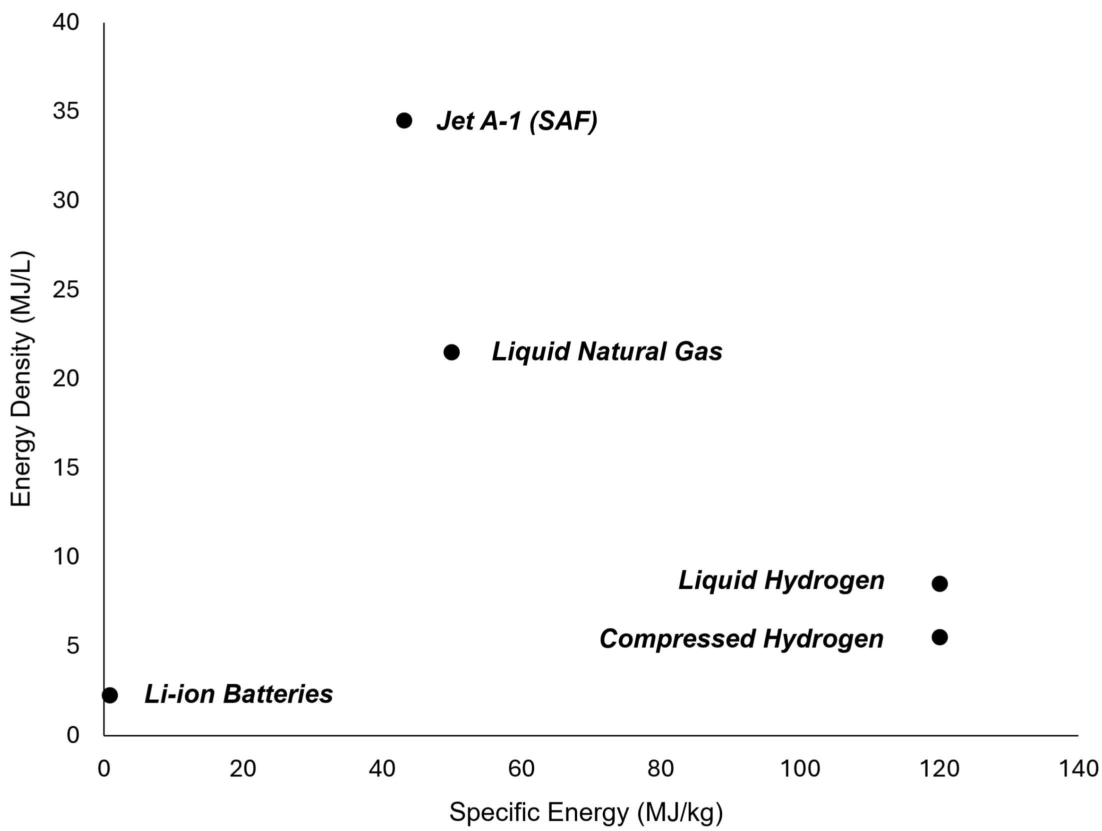

Figure 1.1: Comparison of specific energy and volumetric energy density of various energy carriers

Before examining the energy consumption and emissions associated with aircraft operations, it is important to establish context regarding potential energy carriers for aviation. Figure 1.1 presents a comparative overview of the specific energy and volumetric energy density of current and prospective energy sources proposed for aviation applications. Conventional jet fuel (Jet A-1), which accounts for the vast majority of commercial aviation fuel consumption, represents an effective energy carrier due to its favourable balance between high specific energy and high volumetric energy density, providing a fuel that is both lightweight and compact enough to support efficient aircraft design and operation.

Hydrogen has been widely proposed as a future aviation energy carrier due to its zero-carbon composition and exceptionally high specific energy, which is nearly three times that of Jet A-1. However, even when stored as a compressed gas at 700 bar or as a cryogenic liquid at $-253\,^{\circ}\mathrm{C}$, hydrogen exhibits a volumetric energy density more than four times lower than that of jet fuel. This limitation introduces significant challenges for aircraft integration, including increased tank volume, structural mass penalties, and airframe design constraints, which are discussed in subsequent sections.

Electrochemical energy storage using Lithium-ion (Li-ion) batteries offers the potential for zero-emission operation at the point of use; however, the low specific energy and volumetric energy density of current battery technologies make them unsuitable for commercial aircraft beyond very short-range applications. Sustainable Aviation Fuel (SAF) represents a lower-carbon alternative that closely matches the properties of Jet A-1, enabling compatibility with existing aircraft and infrastructure. Despite these advantages, large-scale deployment of SAF is constrained by production capacity and energy intensity. Liquid Natural Gas (LNG) has been proposed as an alternative aviation fuel, but it retains many of the volumetric storage challenges associated with hydrogen without eliminating carbon emissions.

Given the objectives of this research, which focus on evaluating pathways toward more sustainable aircraft operations, subsequent analyses regarding decarbonisation focus on comparative assessments of SAF and hydrogen as prospective aviation energy carriers.

1.1.4 Decarbonisation Challenge

With increasing climate concerns and pressure to meet ambitious goals and objectives, it is necessary to undergo a major revolution to reduce emissions in the aviation sector if sustainable economic growth is to be achieved. This is particularly challenging as global airline traffic continues to outpace technology improvements, which continuously leads to an annual net increase in emissions. It has been suggested that airline traffic could increase as much as 3–5% per year, while efficiency improvements in terms of fuel consumption per passenger-kilometre have historically averaged around 1.5% per year [9]. Disruptive technologies and environmentally friendly energy sources will be required to curb these emissions.

Not only does an increase in emissions also raise taxes through the EU's Emissions Trading System (ETS) [11], increasing the effective cost of fuel, but it also contributes to damaging public perception of the aviation industry. Although the aviation industry only accounts for approximately 5% of the global impact on anthropogenic warming [12] including CO_2 and non-CO_2 effects, this figure could increase rapidly with the relative decrease in emissions in other industries. This has already been observed from 2013 to 2018, as highlighted by the growing share of aviation-related ETS emissions in Figure 1.2.

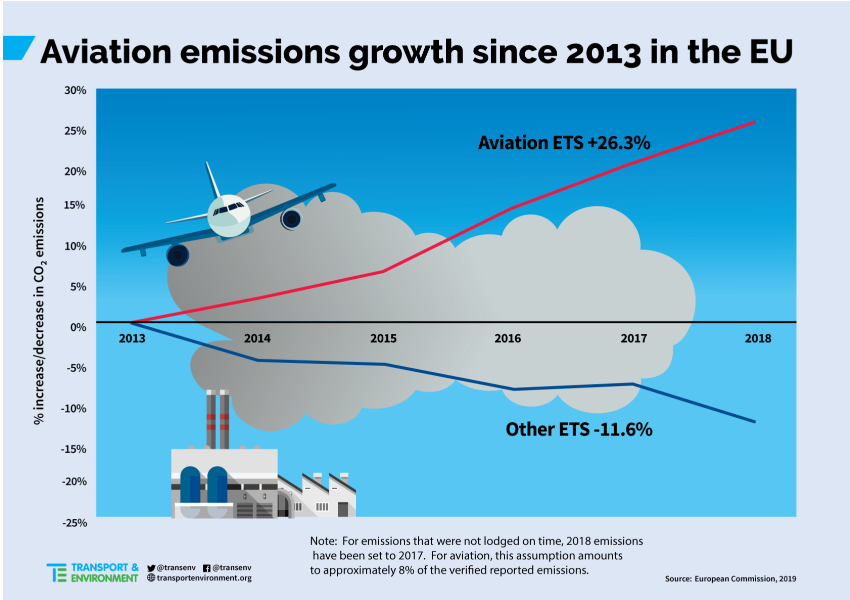

Figure 1.2: Aviation ETS emissions compared to other sectors from 2013 to 2018 [10]

If aviation does not find a solution to sustainable growth, there is a fear that market growth could stagnate or even fall over the next decades. This would result in airlines going into liquidation and jobs being lost, while many customers would lose access to air travel, and tourism would be affected resulting in the loss of globalisation benefits around the world.

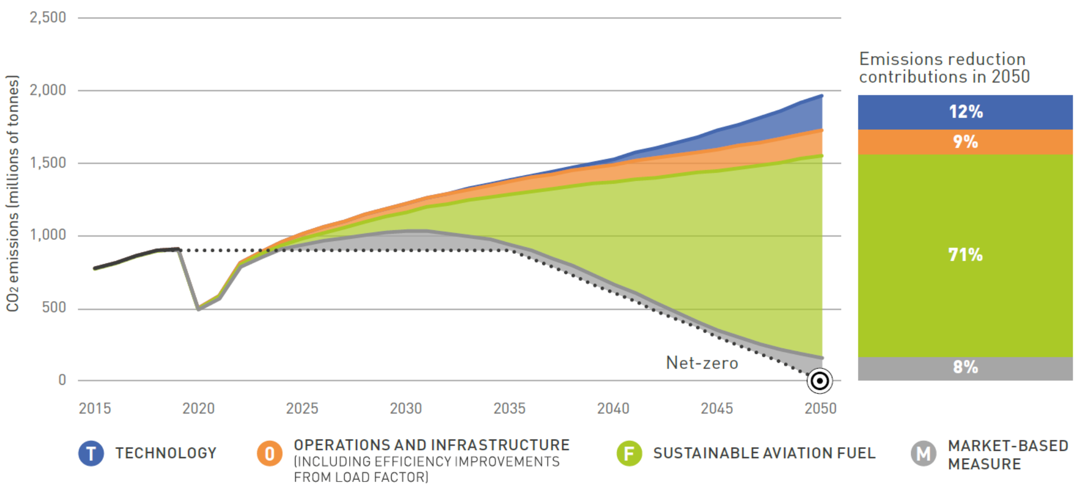

Figure 1.3: Projected CO_2 emission reductions from technology, operations, SAF, and market-based measures [4]

Figure 1.3 shows the projected Carbon Dioxide (CO_2) emission reductions that could be achieved toward 2050 through technological improvements, operational improvements, Sustainable Aviation Fuel (SAF), and market-based measures when deploying an aggressive SAF strategy [4]. Although technological and operational improvements have a crucial role to play in reducing the overall energy demand of aviation (and therefore mitigating the increased cost of alternative fuels), they are not expected to be the main driver of decarbonisation. In order to achieve net-zero carbon emissions within the aviation industry, net-zero carbon fuels such as SAFs or zero-carbon fuels such as hydrogen must be implemented on a global scale. However, there is significant debate and uncertainty surrounding the optimal decarbonisation pathways for commercial aviation. This is observed through the contrasting technology roadmaps of Boeing [13] and Airbus [14], who intend to predominantly adopt SAF and hydrogen for future aircraft, respectively. Accurate modelling techniques are required to provide a clear scientific direction in terms of the most feasible pathways towards decarbonisation, which should be centred around minimising the overall energy demand and cost of implementation. This requires consideration of both alternative energy sources and advanced technologies, as sustainable energy sources will be expensive and supply constrained, therefore more efficient aircraft are required to reduce the overall fuel demand and cost of future aircraft operations.

1.1.5 Non-Carbon Emissions

Considerable focus has been placed on decarbonising the aviation sector in order to meet the goals of the Paris agreement, which aims to limit the increase in global surface temperature between 1.5 °C and 2 °C [15]. Although CO_2 emissions are a significant contributing factor to climate change, there are several non-carbon aircraft emissions that also harm the environment, as illustrated in Figure 1.4. Recent studies suggest that the impact of these non-CO_2 emissions (i.e., Nitrogen Oxides (NO_x), Sulphur Dioxide (SO_2), Carbon Monoxide (CO), Particulate Matter (PM), and water vapour (H_2O)), and contrail formation induced by these emissions, could be up to two times greater than CO_2 emissions in the context of global warming [16]. Such studies have prompted the EU to introduce new measures in which aircraft operators are required to Monitor, Report, and Verify (MRV) their annual non-CO_2 emissions with an expectation to legislate within the ETS by 2028, as described in the MRV non-CO_2 guidance document for aircraft operators [17]. The heightened interest in non-CO_2 emissions is further supported by the joint statement by the chief technology officers of major aviation companies, calling for increased research funding to accelerate scientific understanding of non-CO_2 effects [18].

Although methods have been developed to predict non-CO_2 emissions and their impact on the climate, scientific understanding remains limited and the uncertainty associated with existing techniques is high [12]. The EU has proposed that airline operators will use a commission IT tool – 'Non-CO_2 Aviation Effects Tracking System (NEATS)' – to predict their non-CO_2 emissions in compliance with MRV regulations [17]. Further inspection of the proposed methods used by NEATS shows that non-CO_2 emissions are predicted using empirical methods. Although empirical methods are useful for predicting pre-existing aircraft designs, accurate physics-based methods are desirable for aircraft operators to further validate their non-CO_2 emissions throughout the full spectrum of route, range, and payload combinations, while providing a tool to evaluate the emissions of future flight schedules with the introduction of new prospective aircraft designs and energy carriers, enabling data-driven fleet planning to achieve environmental objectives.

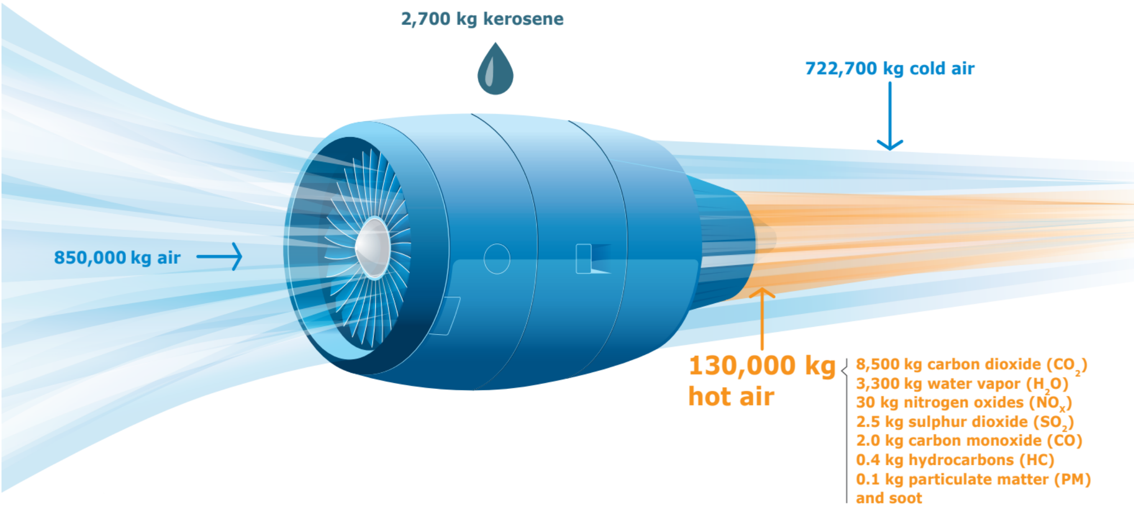

Figure 1.4: Emissions from a typical two-engine jet aircraft during a 1-hour flight with 150 passengers [19]

1.2 Aircraft Fundamentals

Aircraft flight is governed by the balance of aerodynamic, propulsive, and gravitational forces. The resulting motion can be described using Newton's laws and aerodynamic principles, while propulsion systems are governed by thermodynamic cycles that convert fuel energy into useful mechanical and kinetic work. This section outlines the physical principles underlying aircraft motion, aerodynamics, and propulsion thermodynamics, which together form the foundation for subsequent analyses of aircraft performance and emissions. In addition, a brief introduction to aircraft fuels and the associated climate impact of combustion-related emissions is provided.

1.2.1 Aerodynamics

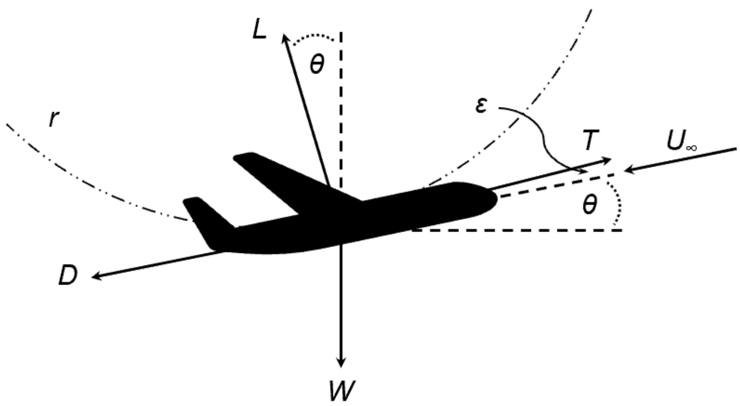

Figure 1.5: Forces and motion of an aircraft in climbing flight

The aerodynamic behaviour of an aircraft determines how forces are generated and balanced during flight. The motion of the aircraft is dictated by the four fundamental forces highlighted in Figure 1.5: Lift (L), Drag (D), Weight (W), and Thrust (T). In the vertical plane, lift acts perpendicular to the freestream velocity (U_∞) and counteracts the aircraft weight, enabling sustained flight, while weight acts downward towards the centre of the Earth. Drag acts parallel and opposite to the direction of motion, representing aerodynamic resistance, and thrust is generated by the propulsion system to overcome drag and sustain velocity. In general, thrust does not necessarily act in the freestream direction, as highlighted by the thrust misalignment angle ϵ in Figure 1.5.

Acceleration parallel to the flight path is given by Equation 1.1, where m is the aircraft mass and θ is the climb angle, which is illustrated in Figure 1.5. $T\cos\epsilon$ represents the component of thrust contributing to forward motion, while drag and the axial component of weight oppose motion during climb. This equation shows that longitudinal acceleration results from a thrust surplus relative to aerodynamic drag and gravitational effects.

$$m\,\frac{dU_\infty}{dt} = T\cos\epsilon - D - W\sin\theta \tag{1.1}$$

Acceleration perpendicular to the flight path governs changes in the direction or curvature of the flight path. Resolving forces normal to the flight path in the vertical plane yields Equation 1.2, where r is the local radius of curvature of the flight path as illustrated in Figure 1.5. The left-hand side of the equation represents the centripetal acceleration required to follow a curved trajectory, while the right-hand side shows the net force normal to the flight path. Lift provides the dominant contribution to this acceleration, with additional effects from the normal component of thrust and the projection of weight.

$$m\,\frac{U_\infty}{r} = L - W\cos\theta + T\sin\epsilon \tag{1.2}$$

In the case of steady, level flight, the aircraft experiences no acceleration and the flight path is straight and horizontal, and therefore, $\theta = 0$, $\frac{dU_\infty}{dt} = 0$, and $r \to \infty$. Under these conditions, and ignoring the thrust misalignment angle ϵ, the equations simplify to the familiar force balances given in Equation 1.3 and Equation 1.4 for the horizontal and vertical forces, respectively.

$$T = D \tag{1.3}$$

$$L = W \tag{1.4}$$

Aerodynamic forces arise from the pressure and shear stress distribution over the aircraft surfaces as air flows around them. The magnitude of lift and drag is calculated using the expressions outlined in Equation 1.5 and Equation 1.6, respectively, where ρ is the density, C_L and C_D are the coefficient of lift and drag, respectively, and S is the wing reference area.

$$L = \frac{1}{2}\cdot\rho\cdot C_L\cdot U_\infty^2\cdot S \tag{1.5}$$

$$D = \frac{1}{2} \cdot \rho \cdot C_D \cdot U_\infty^2 \cdot S \tag{1.6}$$

Aerodynamic efficiency, expressed as the lift-to-drag ratio (L/D), provides a key indicator of aircraft performance. A higher L/D ratio implies that less thrust is required to sustain flight, improving overall fuel efficiency [20]. The coefficients C_L and C_D depend on several parameters, including aerofoil shape, angle of attack, Mach number, and atmospheric conditions. The total drag coefficient of an uncambered aerofoil is typically represented as a quadratic function of lift coefficient, as outlined in Equation 1.7 where C_{D_0} is the zero-lift drag coefficient, determined by aircraft shape and surface friction, and k is the induced drag factor, calculated using Equation 1.8.

$$C_D = C_{D_0} + k \cdot C_L^2 \tag{1.7}$$

$$k = \frac{1}{\pi \cdot e \cdot AR} \tag{1.8}$$

Where e represents the span efficiency, and the Aspect Ratio (AR) of the aircraft wing is given by Equation 1.9, with b representing the wingspan. Increasing AR reduces induced drag and improves aerodynamic efficiency, particularly during low-speed flight where the lift coefficient is high (e.g., take-off, climb, and approach) [21]. At higher speeds, parasite drag, and eventually compressibility-related wave drag, become increasingly dominant, while induced drag decreases as the required lift coefficient reduces. In steady, level flight at fixed aircraft weight, the minimum drag condition occurs when induced drag and parasite drag are equal. This condition also corresponds to the maximum L/D ratio, and therefore represents the most aerodynamically efficient operating point under these assumptions [20].

$$AR = \frac{b^2}{S} \tag{1.9}$$

A drag polar curve, illustrated in Figure 1.6, plots C_D against C_L and is often used to characterise the aerodynamic behaviour of an aerofoil or aircraft configuration at a specific Mach number and angle of attack. This allows designers to identify optimum cruise conditions – corresponding to the maximum L/D ratio – and assess aerodynamic penalties associated with different flight regimes.

1.2.2 Propulsion

Aircraft propulsion systems convert chemical energy from fuel into useful thrust through a thermodynamic process. Modern aircraft engines operate on the basis of the Brayton cycle, which underpins gas turbine technology and its derivatives, including turbojets, turboprops, and turbofans.

Brayton Cycle

The ideal gas turbine power cycle is also known as the Brayton cycle and can be thermodynamically represented using a T-S diagram as shown in Figure 1.7 (a). This cycle

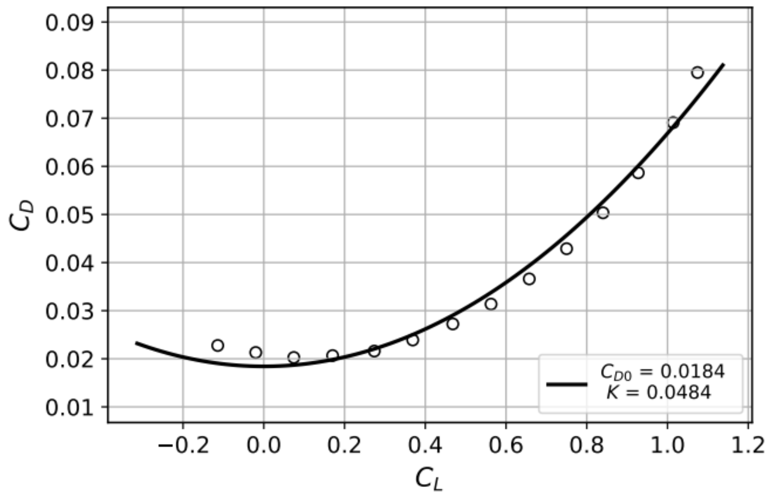

Figure 1.6: Drag polar of an aircraft [21]

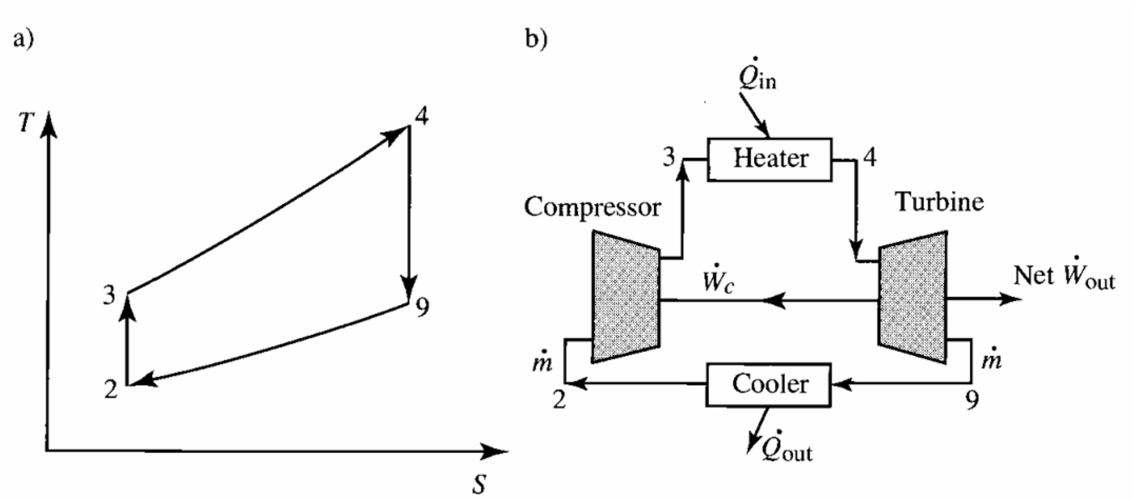

Figure 1.7: Ideal Brayton cycle for a gas turbine: (a) T-S diagram (b) Cycle schematic diagram [22]

consists of four fundamental processes [22]:

1. Isentropic compression (2 – 3) in the compressor
2. Constant-pressure heat addition (3 – 4) in the combustor
3. Isentropic expansion (4 – 9) in the turbine
4. Constant-pressure heat rejection (9 – 2) to the surroundings

Assuming a calorically perfect gas, the thermal efficiency of the cycle is defined by Equation 1.10, where PR is the compressor pressure ratio, and γ is the specific heat ratio of the working fluid [22]. Increasing the pressure ratio improves thermal efficiency but introduces practical limits due to material temperature constraints and compressor performance.

$$\eta_{th} = 1 - \left(\frac{1}{PR}\right)^{\frac{(\gamma-1)}{\gamma}} \tag{1.10}$$

Turbojet

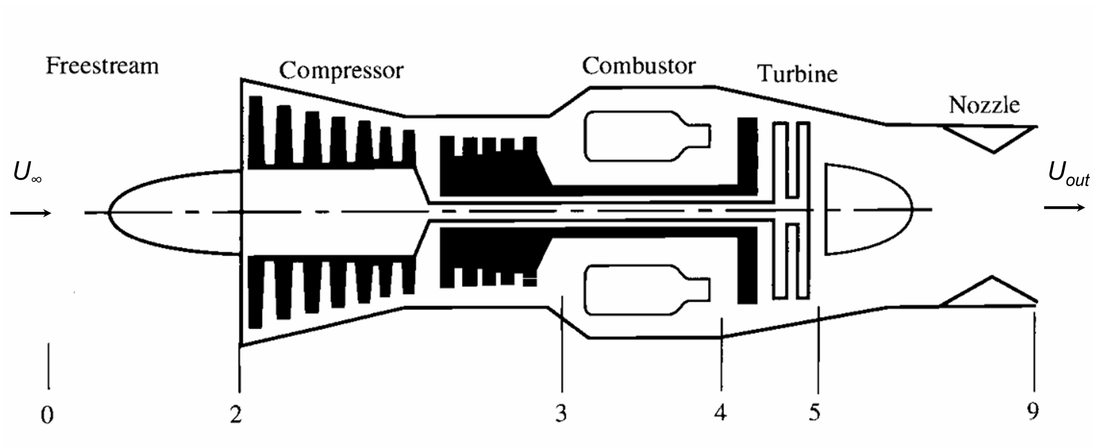

Figure 1.8: Turbojet engine, adapted from [22]

The turbojet pictured in Figure 1.8 is the simplest form of the gas turbine engine, implementing the Brayton cycle in practice. It consists of a diffuser inlet, multi-stage compressor, combustor, turbine, and exhaust nozzle. The compressor raises the air pressure; fuel is injected and burned at almost constant pressure in the combustor; and the turbine extracts energy to drive the compressor. The remaining energy accelerates the flow through the exhaust nozzle, producing thrust according to Equation 1.11, where $\dot{m}_{air}$ is the air mass flow rate and U_{out} is the exhaust velocity [22]. This definition of thrust assumes a fully expanded flow, an idealised control volume, and a negligible thrust contribution from fuel mass flow.

$$T = \dot{m}_{air} \cdot (U_{out} - U_\infty) \tag{1.11}$$

The propulsive efficiency represents the fraction of exhaust kinetic energy converted into useful thrust, which can be calculated for a single inlet, single exhaust engine using Equation 1.12 [22]. Engine design seeks an optimal trade-off between jet velocity and propulsive efficiency, as higher exhaust velocities increase thrust but reduce propulsive efficiency. Due to high exhaust velocities, turbojet engines are generally limited to supersonic and military applications.

$$\eta_{pr} = \frac{T \cdot U_\infty}{T \cdot U_\infty + \frac{1}{2} \cdot \dot{m} \cdot (U_{out}^2 - U_\infty^2)} = \frac{2}{1 + \frac{U_{out}}{U_\infty}} \tag{1.12}$$

Turboprop

Turboprop engines use the gas turbine to generate shaft power that drives a propeller through a reduction gearbox. This configuration achieves high propulsive efficiency at low flight speeds (typically below Mach 0.6) by accelerating a large mass of air at relatively low velocity. However, at higher speeds, compressibility effects at the propeller tips induce shock waves and performance losses, limiting their application to regional and short-haul aircraft, along with military transport aircraft due to their superior short take-off capabilities [22]. In August 2025, turboprop-powered aircraft comprised 9.4% of the global commercial transport fleet, but just 0.6% of the Available Seat Kilometres (ASK) [23]. Figure 1.9 illustrates the propulsive efficiency of various aircraft engines, where the advantage of turboprops for low-speed flight is clearly observed.

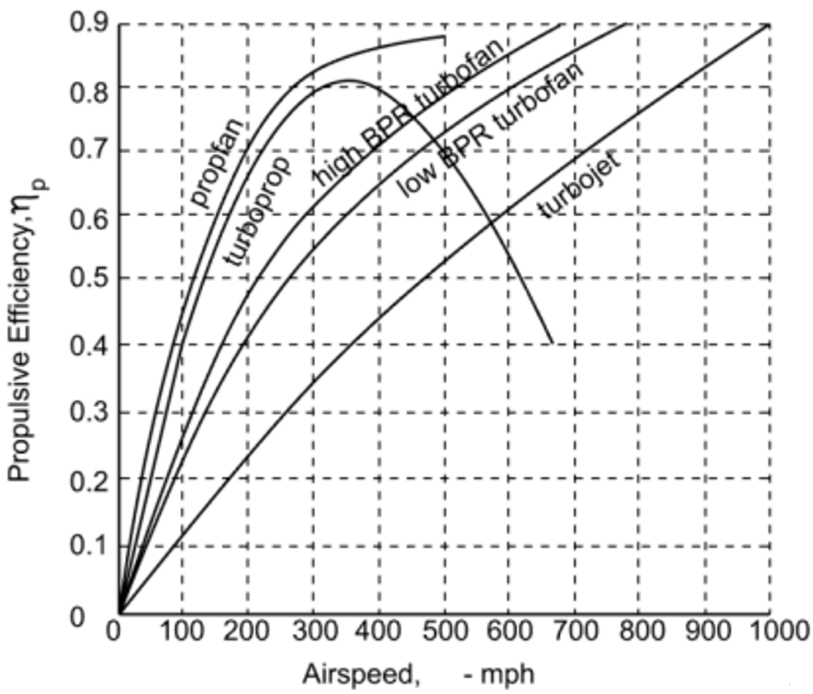

Figure 1.9: Propulsive efficiency with respect to airspeed for different aircraft engines, adapted from [24]

Turbofan

Turbofan engines dominate modern commercial aviation, comprising more than 90% of the global commercial transport fleet as of August 2025, and more than 99% of the ASK [23]. Turbofan engines are desirable for commercial applications as they provide a balance between specific thrust and propulsive efficiency. This is achieved through the generation of thrust using a ducted fan rather than external propellers, which improves aerodynamic performance, allowing transonic speeds without significant compressibility losses [22]. The Bypass Ratio (BPR), outlined in Equation 1.13, defines the proportion of air that passes through the fan relative to the core, and is a key performance parameter which drives the specific thrust and fuel efficiency of the engine [22].

$$BPR = \frac{\dot{m}_{bypass}}{\dot{m}_{core}} \tag{1.13}$$

Higher bypass ratios offer greater propulsive efficiency and lower noise by reducing the equivalent exhaust jet velocity. However, they also increase engine size and structural weight, resulting in performance trade-offs.

1.2.3 Performance Metrics

In general, aircraft efficiencies are compared using overall efficiency, or more commonly Thrust Specific Fuel Consumption (TSFC), which provides a direct indication of fuel consumption and a measure of overall efficiency to which it is inversely proportional [20]. The TSFC is defined in Equation 1.14, where $\dot{m}_f$ is the fuel mass flow.

$$TSFC = \frac{\dot{m}_f}{T} \tag{1.14}$$

Linked to the efficiency of the aircraft is the range, or the ground distance, that the aircraft can travel in a single trip. The Breguet range equation, defined by Equation 1.15, provides an estimate of the aircraft range based on overall efficiency, aerodynamic efficiency, fuel-to-overall weight ratio, and the specific energy of the fuel used [20]. The equation is derived from the force balance in steady, level flight.

$$Range \approx R_f = \frac{L}{D} \cdot \eta_{pr} \cdot \eta_{int} \cdot \eta_{th} \cdot \frac{LHV}{g} \cdot ln\left(\frac{1}{1 - \frac{m_f}{TOW}}\right) \tag{1.15}$$

Where η_{pr}, η_{int}, η_{th} denote propulsive efficiency, propulsion integration efficiency, and thermal efficiency, respectively, where the combined product equals the overall efficiency $\eta_{overall}$. LHV refers to the Lower Heating Value, while m_f denotes the fuel mass, and TOW is the Take-Off Weight of the aircraft. Engine thrust decreases with altitude due to the reduction in air density, which outweighs the increase in thrust associated with lower ambient temperatures. In contrast, TSFC improves with altitude as reduced ambient temperatures increase the corrected engine speed, shifting the operating point towards a higher mass flow and pressure ratio, thereby increasing thrust more rapidly than fuel flow [25]. However, TSFC improvements plateau above approximately 11 km, where the stratospheric temperature stabilises. For this reason, long-range commercial aircraft generally cruise near this altitude, balancing aerodynamic drag, thrust capability, and fuel economy.

1.2.4 Fuels

Jet Fuel

Conventional jet fuel, Jet A-1, is a kerosene-based hydrocarbon fuel that has underpinned commercial aviation for decades. Its widespread use is primarily due to its high gravimetric and volumetric energy density, as illustrated in Figure 1.1, together with favourable handling and operational properties, including thermal stability, low freezing point, and low viscosity [26]. In addition, there is a well-established infrastructure associated with its production and accessibility, which results in a low-cost energy source. However, its combustion contributes significantly to global CO_2 emissions and non-CO_2 effects. The amount of CO_2 emissions produced by the combustion of Jet A-1 is estimated using a fixed value given by the stoichiometric relationship of the combustion reaction defined in Equation 1.16, where m_{CO_2} is the CO_2 mass and 3.157 represents the CO_2 Emission Index (EI) [27]. However, this EI value assumes that all carbon is fully oxidised and ignores incomplete combustion at off-design conditions.

$$m_{CO_2} = 3.157 \cdot m_f \tag{1.16}$$

Sustainable Aviation Fuel

SAFs are hydrocarbon fuels produced from non-fossil feedstocks, such as biomass or captured carbon from the atmosphere. The production of these fuels is intended to be as close to 'net-zero' CO_2 emissions as possible, and can be manufactured through the production of synthesis gas using biomass products to produce biofuel, or artificial carbon sequestration combined with green hydrogen. Green hydrogen refers to hydrogen that has been produced using emission-free energy, i.e., renewable electricity. The synthesis of captured carbon with green hydrogen to produce a synthetic jet fuel is commonly referred to as synthetic SAF, Power-to-Liquid (P2L or PtL) SAF, or e-SAF, where an example production pathway of synthetic SAF is illustrated in Figure 1.10. Certified SAF pathways have demonstrated drop-in compatibility with current gas turbines [28], allowing incremental adoption without redesigning aircraft or fuel infrastructure – a key advantage for near-term deployment. However, the magnitude of climate benefit depends on the feedstock source, land-use, and emission intensity of the production processes [29], while availability and cost are the main challenges in terms of scalability [30].

Hydrogen

Hydrogen offers a higher specific energy than conventional fuels – up to three times that of Jet A-1, as highlighted in Figure 1.1 – enabling a reduced fuel weight and the possibility of new aerodynamic and propulsion concepts. However, its low volumetric energy density necessitates either cryogenic or high-pressure storage in larger and more complex tanks

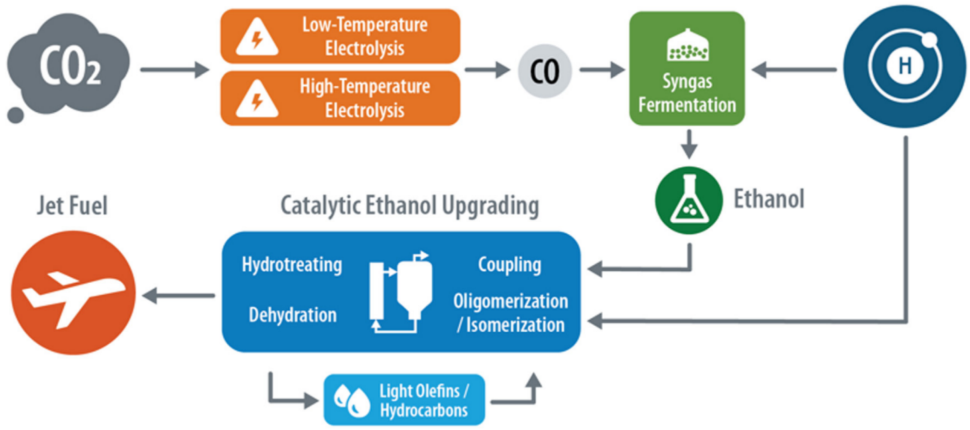

Figure 1.10: Block flow diagram representing the production process of synthetic SAF via ethanol to jet pathway [29]

than conventional kerosene systems, affecting aircraft integration, performance, and range. In addition, significant infrastructure investment would be required for the production and deployment of hydrogen within airports at scale. Hydrogen is the most abundant element in the universe; however, although hydrogen itself is a zero-carbon fuel, its production today yields high carbon intensity metrics due to its production methods, often linked to the processing of hydrocarbons such as Steam-Methane Reforming (SMR), coal gasification and oil/coal cracking [31]. In fact, studies show that blue hydrogen production, formed using SMR with carbon capture, produces more greenhouse gases with respect to the Global Warming Potential (GWP) than direct combustion of natural gas, as highlighted by Figure 1.11 [32]. In any scenario where hydrogen is used within aviation, it is crucial that the production of green hydrogen, which currently accounts for approximately 1% of the global hydrogen production [33], is sufficient to ensure that emission reductions are achieved.

1.2.5 Emissions and Climate Impact

The climate impact arising from aircraft emissions is summarised in Figure 1.12, where CO_2 and the net effects caused by NO_x emissions and contrail formation together cause the greatest impact on anthropogenic Radiative Forcing (RF) [12]. The following sections briefly introduce these aircraft emissions and their climate impact.

Carbon Dioxide

CO_2 emissions from aircraft arise directly from the combustion of hydrocarbon fuels and represent the primary long-term contributor to aviation's climate impact. Once emitted, CO_2 persists in the atmosphere for centuries, leading to cumulative and irreversible global warming [35]. Because aviation demand continues to grow, sectoral CO_2 emissions have increased despite improvements in aircraft efficiency and operational practices [9]. Consequently, reducing CO_2 emissions requires not only incremental efficiency gains through technology improvements but also a transition to low- or zero-carbon energy sources, such

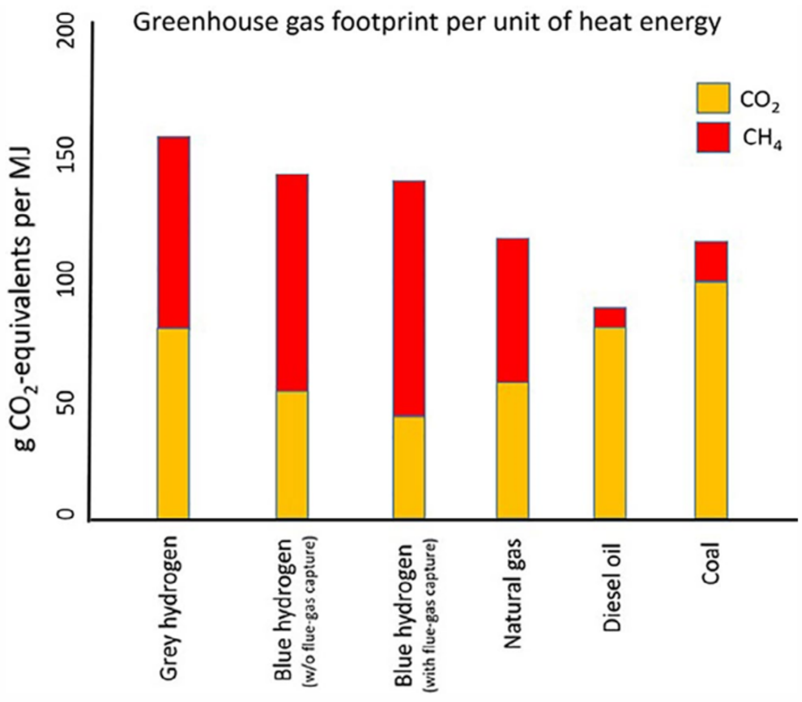

Figure 1.11: Comparison of equivalent CO_2 emissions for hydrogen production against hydrocarbon combustion [32]

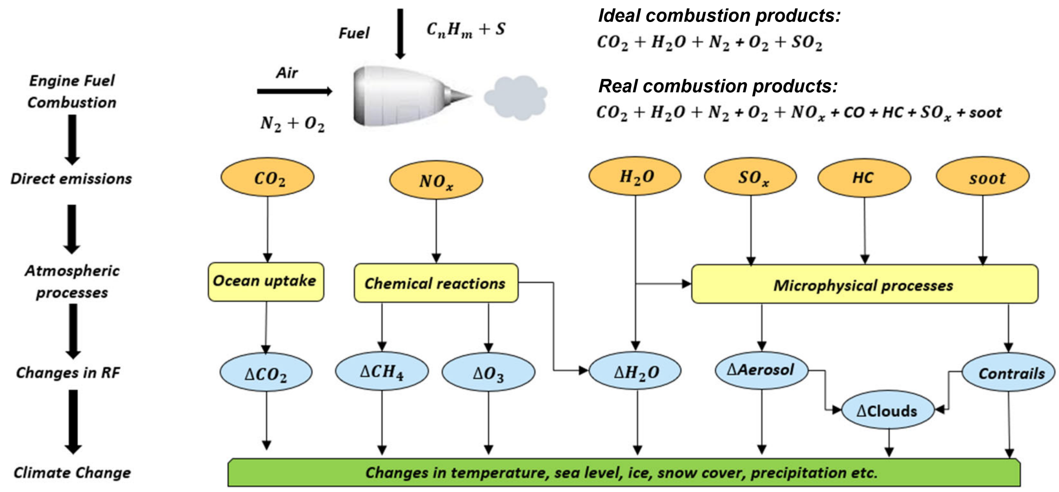

Figure 1.12: Overview of the aircraft engine emissions and their resultant effects and climate impacts, adapted from [34]

as SAF or hydrogen, making decarbonisation a central objective of future propulsion system development and fuel strategies.

Nitrogen Oxides

Nitrogen oxides (collectively NO_x, mainly NO and NO_2) are emitted during high-temperature combustion within gas turbine engines. Although NO_x itself is not a greenhouse gas, it contributes to global warming by increasing the concentration of short-lived ozone (O_3), resulting in near-term warming, while simultaneously reducing atmospheric methane (CH_4), a long-lived greenhouse gas, which produces a cooling effect that partially offsets the net NO_x-induced warming [12]. The net climate response of NO_x depends strongly on where and under what conditions the emissions occur, making accurate modelling techniques sensitive to altitude, latitude, meteorological conditions, and combustor characteristics [34]. As future fuels and combustor architectures evolve, high-fidelity emission modelling becomes essential to quantify how NO_x formation and its climate impacts will change under future aviation scenarios.

Contrail Formation

In addition to gas-phase emissions, aircraft engines produce water vapour and PM that can trigger the formation of condensation trails (contrails) when operated in cold, humid regions of the upper troposphere (8 – 13 km) [36]. An example of aircraft-induced contrail formation is shown in Figure 1.13. Persistent contrails can spread into contrail-induced cirrus clouds, which trap outgoing long-wave radiation and are widely considered the largest short-term contributor to aviation's radiative forcing apart from CO_2 [12]. The presence, persistence and associated climate impact of contrails depend on ambient conditions, engine emissions, flight routing, and time of day, resulting in high spatial and temporal variability [16]. Future fuels such as SAF and hydrogen can reduce particulate matter emissions, and therefore have the potential to mitigate contrail formation [37]. Therefore, it is important to develop physics-based models that can accurately predict the exhaust emissions of future propulsion concepts, alongside meteorological and operational models, to determine the climate footprint of future aircraft operations.

1.3 Research Aim

The overarching aim of this thesis is to develop a modelling framework that helps address the two main climate-related issues within the aviation industry, related to the decarbonisation of future aircraft operations, along with the understanding and evaluation of non-CO_2 effects and their associated climate impact. The research seeks to enhance the understanding of how emerging technologies, alternative fuels, and operational strategies influence aircraft performance and environmental impact when evaluated under realistic operating conditions. A further aim is to establish modelling approaches that are sufficiently accurate to capture the key physical behaviours of both current and prospective future aircraft, while remaining computationally efficient for large-scale scenario analysis.

Figure 1.13: An instance of aircraft-induced contrail formation [38]

Together, the thesis aims to provide a framework that supports comparative technology evaluation and informs long-term decisions for aircraft operators through data-driven fleet planning. This broad objective motivates the subsequent literature review, which examines the limitations of current modelling approaches and identifies the specific research questions addressed in this work.

1.3.1 Thesis Structure

Chapter 1

Chapter 1 introduces the context and motivation for the research, outlining the environmental challenges facing the aviation sector and the need for credible decarbonisation pathways. It summarises the fundamental principles of aircraft modelling, including aerodynamics, propulsion, and key performance metrics, and provides an overview of proposed alternative fuels. The chapter also introduces the climate impacts associated with major aircraft emissions, establishing the background for the detailed literature review in Chapter 2.

Chapter 2

Chapter 2 presents a comprehensive literature review covering emerging aircraft and propulsion technologies, alternative fuels such as SAF and hydrogen, and the formation and climate impacts of non-CO_2 emissions. It also reviews the modelling tools and methods commonly used in aircraft performance and emissions research. Particular attention is given to the assumptions and limitations of current modelling approaches, enabling the identification of key gaps that motivate the research questions addressed in this thesis.

Chapter 3

Chapter 3 outlines the methodology used to develop the baseline modelling framework, detailing the aerodynamic, propulsion, and mission analysis models used to represent real-world aircraft operations. It also presents fuel-flow validations with respect to the baseline aircraft configurations against operational airline data to establish model credibility. The resulting framework forms the foundation for the decarbonisation and emissions analyses conducted in Chapters 4 and 5.

Chapter 4

Chapter 4 presents an operational case study evaluating optimal decarbonisation pathways for short-haul airlines, focusing on a comparative assessment of liquid hydrogen and synthetic SAF across real-world flight operations. The chapter outlines the development of the hydrogen aircraft configurations and describes the case-study setup, where conventional and hydrogen-powered variants are simulated over an entire day of airline operations using the validated modelling framework from Chapter 3. The resulting analysis quantifies both in-flight and well-to-wake energy consumption, enabling a direct comparison of the energy performance and relative advantages of liquid hydrogen and SAF for short-haul fleet operations.

Chapter 5

Chapter 5 presents a second operational case-study focused on quantifying CO_2 and non-CO_2 emissions and the resulting climate response for real-world airline operations. The chapter describes the development of novel, physics-based combustion models that provide improved emission predictions compared to conventional methods. These models are integrated into the validated aircraft modelling framework established in Chapter 3, enabling high-fidelity emission predictions throughout complete flight profiles. The case-study simulates a full day of airline operations to evaluate species-specific climate metrics, where the results compare modelling techniques and assess the influence of fleet renewal on global warming.

Chapter 6

Chapter 6 presents the main contributions to knowledge, integrated conclusions, and answers to the research questions. It synthesises the decarbonisation pathway and non-CO_2 emissions studies, highlighting the role of operationally representative, physics-based modelling in evaluating future aircraft technologies. The chapter also discusses key sources of uncertainty, model limitations, and future research directions, including improved emissions validation, extended fuel and aircraft technology assessments, contrail and nvPM modelling, and fleet-level optimisation.

Chapter 2

Literature Review

The following chapter contains a literature review, which aims to summarise advancements and developments in airframe and propulsion systems for commercial aircraft, including alternative fuels to reduce carbon emissions, along with current modelling techniques concerning non-carbon emissions and their associated climate impact. Technology advancements throughout the published literature will be discussed in the context of the performance of previous generation aircraft, future emission goals and targets, and the expected future landscape of the aviation industry when considering traffic growth and proposed regulations.

2.1 Historical Development of Commercial Aircraft

The first commercial airline jet, the De Havilland Comet, first entered service in 1952 [39]. Although some 70 years have passed since this aircraft took flight, commercial aircraft today share a strikingly similar design. This is due to the nature of the civil transport aircraft design process, where evolvability and design reuse are the heart of design strategies [40]. This strategy is adopted as a consequence of the level of risk involved with a "clean-sheet" design, where the designer is said to effectively bet the company on the success of a new product. For this reason, aircraft manufacturers have designed their vehicles in a manner such that they possess the ability to add incremental improvements to either range, payload, or both, with simple tweaks to the baseline design rather than a complete redesign.

In a study investigating the evolvability of civil jet transport aircraft of Boeing, Airbus, and McDonnell Douglas, two distinguishable design patterns were identified: a "leap and branch" pattern, and a "Z" pattern [40]. A leap in this context refers to significant changes in both the propulsion system and the airframe, whereas branches refer to a stretch or shrinkage of the baseline. The 'Z' design pattern follows a similar analogy, but in terms of performance improvements. That is, a progressive increase in the range, followed by an increase in the payload by a stretch, followed by another increase in the range [40], enabled by the design changes illustrated in Figure 2.1. These low-risk design methods ensure a competitive price through savings in design and certification. Certification in particular is a significant risk for manufacturers, as even incremental aircraft designs can

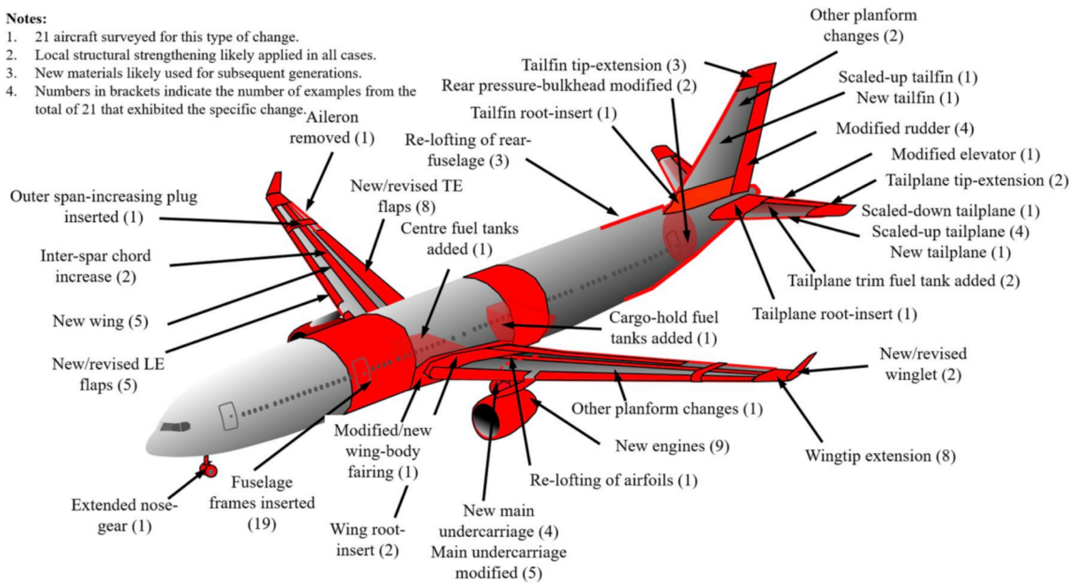

Figure 2.1: Typical design changes of commercial aircraft used to increase payload and range [40]

require certification timelines of up to 9 years [41]. It is crucial to understand the context surrounding aircraft certification challenges when considering the substantial changes required in aircraft design to achieve climate targets within a designated time frame.

2.2 Technology Development

2.2.1 Airframe

Airframe developments can generally be characterised by evolutionary and disruptive designs. Evolutionary designs consist of incremental improvements to the well-established tube and wing design, such as larger wingspans (resulting in a larger AR), lighter materials, and improved aerodynamic shapes. However, incremental design changes eventually yield limited gains without some step-change in the design; for example, AR increases stagnated in recent iterations due to structural constraints associated with large bending loads [42]. Ultra-High Aspect Ratio (UHAR) designs, increasing AR from 9–11 to 16–20, have been proposed to achieve >30% increase in aerodynamic efficiency [43]. The most notable UHAR design is the Transonic Truss-Braced Wing (TTBW) illustrated in Figure 2.2. This design mitigates UHAR structural issues by using a truss support structure, while implementing wing sweep to enable a cruise Mach number of 0.8, with a high-mounted wing to facilitate integration of advanced engine architectures due to the additional ground clearance. The proposed TTBW design provides fuel burn reductions of up to 10% as a result of improved aerodynamic efficiency [44].

Disruptive designs consist of a clean-sheet aircraft design, which strays significantly from the classic tube and wing configuration. The Blended-Wing Body (BWB) is the most commonly proposed disruptive airframe design, which consists of a wing blended with a central lift-producing fuselage generating higher aerodynamic and payload efficiencies,

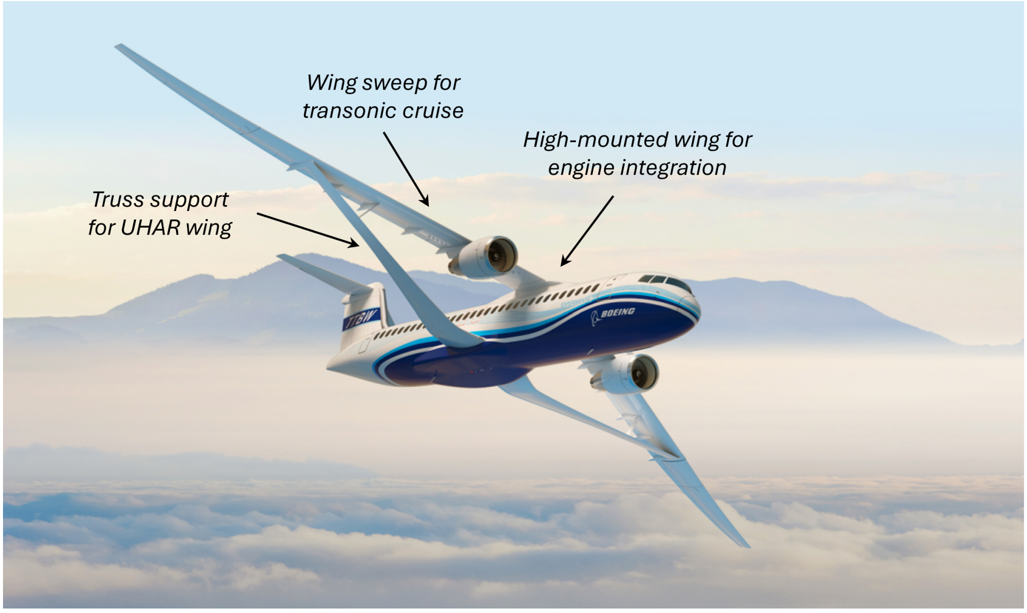

Figure 2.2: Boeing TTBW concept aircraft, adapted from [45]

resulting in an estimated 27% reduction in fuel burn per seat kilometre [46]. The NASA N3-X BWB design, which uses a hybrid-electric propulsion system through electrically-driven fans powered by superconducting generators, is shown in Figure 2.3. However, in the context of the discussion surrounding certification challenges in Section 2.1, it is difficult to envisage such disruptive designs entering service by 2050.

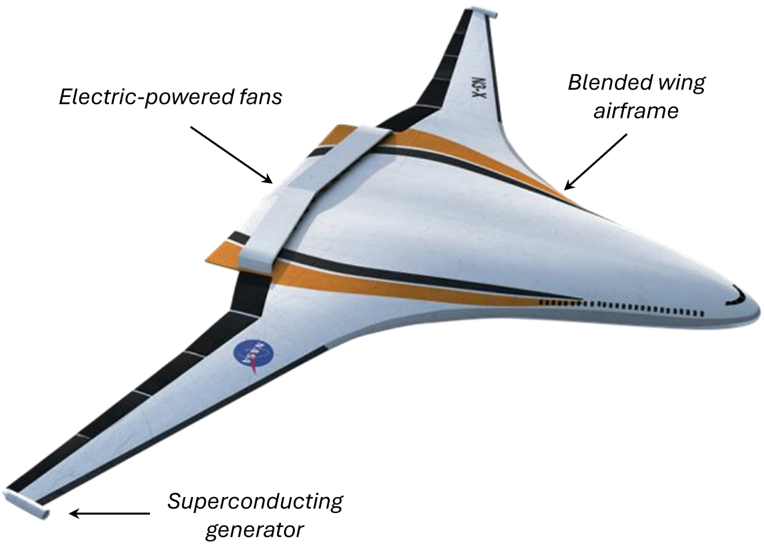

Figure 2.3: NASA N3-X concept aircraft, adapted from [47]

2.2.2 Propulsion

UHBPR Turbofan

Ultra-High Bypass Ratio (UHBPR) turbofans extend the efficiency gains of conventional high-BPR engines by further increasing propulsive efficiency through reduced jet velocities. However, BPR values above 15 introduce significant installation penalties that limit the achievable benefits [48]. These include increased nacelle drag, spillage losses, higher wave drag due to large fan diameters, and reduced fan stability requiring technologies such as variable-area nozzles or variable-pitch fans [48]. Geared architectures with a third spool are also required to mitigate incompatibility issues between the fan and core components caused by mismatched design speeds due to widely varying diameters [48]. These geometric and aerodynamic constraints become particularly problematic for narrow-body integration, where ground-clearance and wing structural limits restrict the maximum achievable fan diameter [48].

Despite these challenges, several recent studies indicate that UHBPR engines can deliver substantial reductions in TSFC relative to current turbofans. Reported improvements include 22–31% TSFC reductions at cruise for geared UHBPR concepts compared to a conventional CFM56 turbofan, as outlined in Table 2.1, and block-fuel reductions above 30% for medium-range missions [49]. These benefits depend strongly on assumed component efficiencies and installation effects. Notably, NASA's N+3 UHBPR design [50], shows higher TSFC than some industry concepts despite a BPR of 24.5 due to differing assumptions regarding compressor, turbine, and combustor performance. Overall, UHBPR engines remain a high-potential technology for next-generation aircraft, although the increased mass penalties and installation effects highlight the need for complete mission analysis rather than isolated TSFC predictions when assessing potential benefits.

Table 2.1: TSFC performance of UHBPR designs.

Engine Model	**EIS Year**	**Cruise TSFC** ($g/kN \cdot s$)	**Δ TSFC**
CFM56-5B (Baseline)	2000	17.52	–
UHBPR-1 [51]	2050	12.60	-28.08%
UHBPR-2 [49]	2025	12.16	-30.60%
UHBPR-3 [50]	2035	13.15	-24.94%
UHBPR-4 [52]	–	13.70	-21.80%

Open-Rotor

The open-rotor, or Unducted Fan (UDF) concept, was developed to bypass the aerodynamic limitations of very large turbofan nacelles by employing external, contra-rotating propellers with highly swept blades. Demonstrators such as the GE-36 in the 1980s delivered fuel-burn reductions of around 30% compared to conventional turbofans, but noise constraints, certification challenges, and falling fuel prices stopped further development [25]. Renewed interest driven by decarbonisation targets has led to new studies of open-rotor designs, incorporating improved propeller aerodynamics, advanced blade structures, and geared low-pressure turbine architectures [51, 53, 54]. Furthermore, CFM International [55] announced an open-rotor engine development programme for next-generation short-haul aircraft, where the proposed CFM RISE design is shown in Figure 2.4.

Figure 2.4: CFM RISE conceptual drawing [55]

Numerical studies show that open-rotor engines can outperform current and next-generation UHBPR turbofans in TSFC, achieving reductions between 31–41% at cruise compared to a conventional CFM56 turbofan, as outlined in Table 2.2. Performance benefits are particularly pronounced for short-haul operations due to increased propeller performance at higher power settings and higher propulsive efficiency at lower flight speeds [56], which was observed in Figure 1.9. Such operations are characteristic of climb segments, which account for a greater proportion of the total flight time for low-range missions. This was confirmed by the work of Gallagher et al. [57], where open rotor engines yielded pronounced performance benefits for mission ranges below 500 NM. However, the narrow TSFC operating loop also means that open-rotor engines are more sensitive to off-design sizing and may incur penalties at mid-cruise or reduced-load conditions [56]. Noise, safety certification, and integration constraints remain key risks, although improved TSFC benefits compared to UHBPR turbofans, particularly for low-range missions, make open-rotor configurations an attractive concept for next-generation short-haul aircraft.

Table 2.2: TSFC performance of open-rotor designs.

Engine Model	**EIS Year**	**Cruise TSFC** ($g/kN \cdot s$)	**Δ TSFC**
CFM56-5B (Baseline)	2000	17.52	–
Open-Rotor-1 [56]	2020	11.10	-36.64%
Open-Rotor-2 [52]	–	12.10	-30.94%
Open-Rotor-3 [51]	2025	11.50	-34.36%
Open-Rotor-4 [51]	2050	10.41	-40.58%

2.2.3 Electrification

More-Electric Aircraft

More-Electric Aircraft (MEA) increase the degree of onboard electrification by replacing conventional pneumatic, hydraulic, and mechanical secondary power systems with electrically driven units [58]. This approach was recently implemented on the Boeing 787, reducing the number of engine off-takes, and thus improving thermodynamic efficiency, lowering fuel burn, and simplifying subsystem integration compared to traditional architectures [58]. MEA represent the first major step in aircraft electrification, providing incremental efficiency benefits while avoiding the mass and energy storage penalties associated with hybrid and all-electric propulsion.

Hybrid-Electric Aircraft

Hybrid-Electric Aircraft (HEA) use both fuel-based and battery-based energy sources, with degrees of hybridisation defined by the relative contributions of electrical power and energy [59]. This framework yields several architectures, including turbo-electric, series-hybrid, and parallel-hybrid configurations, which are illustrated in Figure 2.5. Turbo-electric and series-hybrid systems offer flexibility in the propulsion design, enabling Boundary Layer Ingestion (BLI), distributed propulsion, and other aero-propulsive efficiency gains, but incur significant drivetrain losses and mass penalties because all thrust is produced electrically [59]. Parallel-hybrid designs avoid these drawbacks by allowing mechanical thrust production to remain the primary source of thrust, with electrical power supplementing the turbine during selected mission phases. Consequently, parallel-hybrid architectures are identified as the most feasible near-term option, as they reduce battery and motor sizing requirements while limiting mass penalties [60].

Parallel-hybrid turbofan concepts have demonstrated meaningful fuel-burn reductions when battery energy is used strategically during take-off and climb, while the gas turbine is downsized or shifted towards a more efficient cruise operating point [60]. Studies such as Boeing/NASA's SUGAR Volt programme show fuel-burn reductions ranging from 11–22%, strongly dependent on battery specific energy (typically projected at 500–750 Wh/kg), aircraft configuration, and mission length [43]. Designs incorporating UHAR wings, such as the TTBW, further amplify benefits by reducing aerodynamic penalties associated with the additional electric drivetrain mass [43]. Recent parametric evaluations by Perullo et al. [61] confirm that parallel-hybrid benefits are most pronounced for short-to-medium ranges ($\approx$ 500–1300 NM) where complete utilisation of the onboard battery energy is achievable, and that increases in motor power shift the optimal range downward, while increases in battery specific energy shift it upward. The results of this parametric study are shown in Figure 2.6, where the optimal mission ranges can be observed in terms of fuel burn and energy reductions [61].

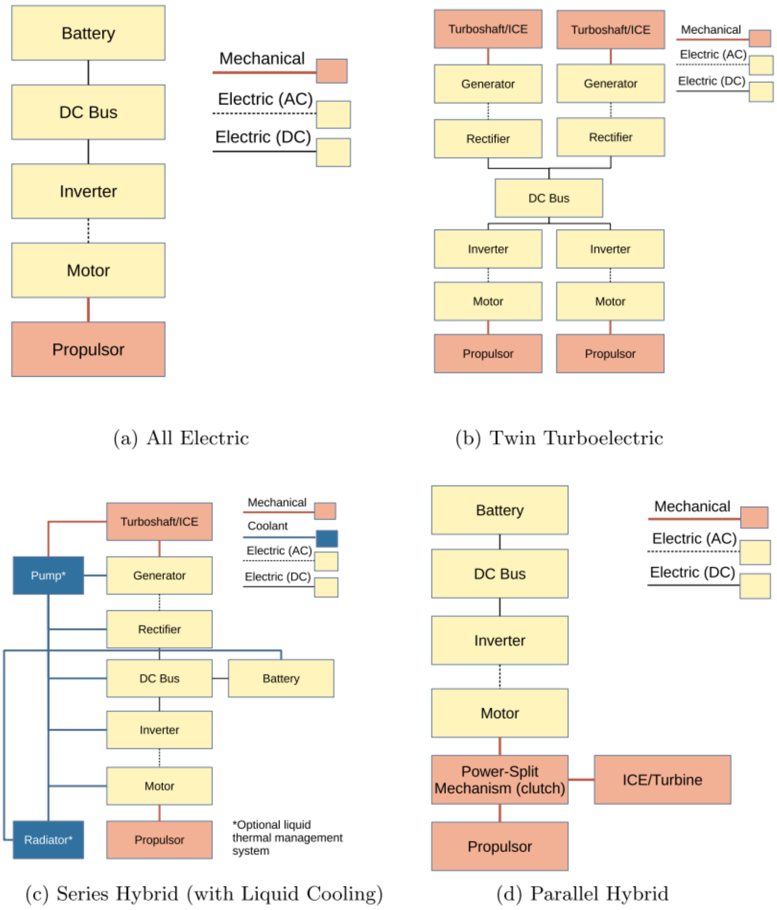

(a) All Electric (b) Twin Turboelectric

(c) Series Hybrid (with Liquid Cooling) (d) Parallel Hybrid

Figure 2.5: Hybrid-electric propulsion architectures [59]

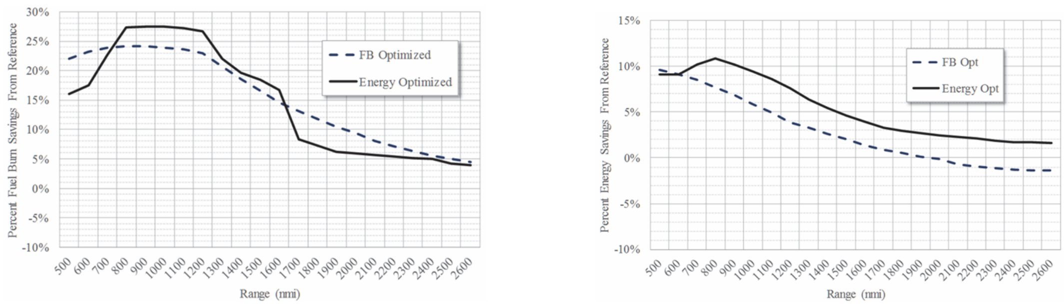

(a) (b)

Figure 2.6: Parametric analysis of mission range for parallel-hybrid aircraft, showing (a) Fuel burn savings (b) Energy savings [61]

All-Electric Aircraft

All-electric aircraft (AEA) rely exclusively on batteries to power electric motors, eliminating in-flight fuel consumption, but facing fundamental constraints due to the high energy and power density requirements of commercial transport missions. Current battery technologies may limit feasible applications to small commuter aircraft, such as NASA's X-57, which carries just two passengers over 100 NM [59]. Earlier feasibility studies for single-aisle aircraft, even under optimistic battery specific energy assumptions of up to 800 Wh/kg, suggested that only short-range missions of approximately 500 nm were achievable, often with reduced overall energy efficiency relative to conventional designs [62]. More recent studies, such as the Elysian E9X concept, challenged this view by demonstrating the potential for battery-electric aircraft that can carry 90 passengers over ranges of 800 km ($\approx$430 NM) using a battery specific energy of 360 Wh/kg [63]. These results highlight that the primary constraint is not solely battery specific energy but the overall system-level energy requirements, particularly the mass associated with reserve energy and certification constraints. Nevertheless, such concepts remain highly sensitive to battery performance assumptions and operational requirements, and are currently limited to short-haul applications.

2.3 Hydrogen Powered Propulsion

Although technology has a role to play in reducing the energy demand of future aircraft, it is clear that net-zero carbon emissions are not feasible without the introduction of alternative fuels. This section focuses on hydrogen as a fuel for future aircraft, which offers zero carbon emissions, but introduces new challenges related to its production, storage, and aircraft design.

2.3.1 Production

The global demand for hydrogen is approximately 100 million tonnes per year [33], serving primarily agriculture, steel production, and the transport sector. As aviation pursues net-zero CO_2 emissions by 2050, its future energy demand is expected to become a significant driver for hydrogen expansion, either through synthetic SAF production or direct use in hydrogen-powered aircraft. Meeting this demand requires rapid, sustainable scaling of the global hydrogen production capacity.

Current production is dominated by fossil-fuel reforming: around 62% of global hydrogen is produced from natural gas, 19% from coal gasification, 18% as a by-product of naphtha reforming, and less than 1% via water electrolysis [33]. Production pathways are commonly described by colour labels. Grey, black, and brown hydrogen refer to hydrogen from natural gas, coal, and lignite, respectively [64]. Blue hydrogen denotes fossil-derived hydrogen with carbon capture, although, as discussed in Section 1.2.4, it remains an unsustainable option due to upstream methane leakage and incomplete CO_2 capture [32]. Green hydrogen, produced exclusively through electrolysis using renewable electricity, represents the only pathway capable of supporting meaningful long-term decarbonisation of aviation. Consequently, all subsequent discussion focuses solely on green hydrogen.

Electrolysis requires both electricity and freshwater. Producing one kilogram of hydrogen consumes approximately nine litres of water, which implies that meeting the annual hydrogen demand by electrolysis would require approximately $6.2 \cdot 10^8$ of water, or 1.3% of the global demand for water in the energy sector [64]. Although freshwater is typically required to avoid corrosion of electrolyser components, seawater-based production is feasible if combined with renewable-powered desalination, increasing hydrogen cost by only \$0.01–0.02 per kg [64]. Table 2.3 summarises the key techno-economic characteristics of alkaline, Proton Exchange Membrane (PEM), and Solid Oxide Electrolyser Cell (SOEC) electrolyser systems.

Table 2.3: Techno-economic characteristics of electrolyser technologies [64].

	Alkaline		**PEM**		**SOEC**	
Parameter	**2020**	**2050+**	**2020**	**2050+**	**2020**	**2050+**
Electrical efficiency (%)	63–70	70–80	56–60	67–74	74–81	77–90
Operating temperature (°C)	60–80	–	50–80	–	650–1000	–
Stack lifetime (10^3 h)	60–90	100–150	30–90	100–150	10–30	75–100
Plant footprint (m^2/kW)	0.095	–	0.048	–	–	–
CAPEX (\$/kW)	500–1400	200–700	1100–1800	200–900	2800–5600	500–1000
Load range (%)	10–110	–	20–100	–	–	–

Electrolysers generate gaseous hydrogen, necessitating a downstream liquefaction stage for aviation applications. Hydrogen liquefies at $-253\,°C$, and associated cryogenic refrigeration makes this step energy-intensive. Liquefaction efficiencies are typically around 75% [31], resulting in current well-to-tank efficiencies for Liquid Hydrogen (LH_2) between 40% and 60% depending on the electrolyser technology used. These values are consistent with performance figures reported in the Clean Sky Hydrogen-Powered Aviation study [9] and the International Council of Clean Transportation (ICCT) study by Mukhopadhaya and Rutherford [65], which quote 58% and 56% production efficiencies, respectively. Future improvements in electrolyser efficiency (Table 2.3) could increase overall production efficiencies to approximately 70%.

2.3.2 Storage

Hydrogen storage presents a major challenge for its use as a transport fuel. Although hydrogen has an exceptionally high gravimetric energy density (almost three times that of conventional jet fuel), its volumetric energy density is at least four times lower [66]. Liquefaction is typically proposed to increase the volumetric density; however, the liquefaction process is highly energy intensive, and the resulting LH_2 must be maintained at cryogenic temperatures, adding significant complexity and operational risk to the storage system [66]. In addition, hydrogen is the lightest existing element and is therefore inherently susceptible to leakage, increasing safety concerns in both ground and onboard applications.

The storage tank design has significant implications on the performance of a hydrogen aircraft. Tank designs generally aim to minimise the weight and space of the overall fuel system while maintaining a stable pressure and temperature of the hydrogen. The weight of the tank is affected by the overall size, the materials used, and the design of the cooling or insulation system [67]. The gravimetric efficiency η_{grav}, equivalent to the Gravimetric Index (GI), is described in Equation 2.1 and is used as a metric to measure the weight of the tank relative to the stored fuel. Temperature control is affected by heat transfer, which is influenced by the surface-to-volume ratio of the tank design, along with the amount of insulation used or the power of the active cooling system, if used [67].

$$\eta_{grav} = GI = \frac{m_{fuel}}{m_{fuel} + m_{tank}} \tag{2.1}$$

There is an inevitable trade-off between weight/space and temperature control: if a design favours lower heat leakage, it requires more insulation, which increases the weight and size of the tank. Designs that favour weight and space will sacrifice heat leakage, causing boil-off of hydrogen throughout the flight. Boil-off requires venting measures to maintain appropriate pressures within the vessel throughout flight [67]. Venting is the process of safely releasing hydrogen vapour from the tank once the maximum allowable pressure is reached, leading to fuel losses. This process decreases the flight efficiency while also increasing the complexity of the tank design. By calculating the total rate of pressure variation in the tank through boil-off and fuel extraction, Huete and Pilidis [67] developed a method to determine venting requirements throughout a flight based on flight time and tank design. The duration before venting is required is referred to as 'dormancy time'.

There are a wide variety of estimations of LH_2 tank gravimetric efficiencies in the published literature, ranging from values as low as 0.2 [65] to values up to 0.76 [68], with many intermediate values [9]. Huete and Pilidis [67] conducted a parametric analysis on LH_2 tank designs for aircraft applications with the aim of understanding the influence of tank size, diameter, length, maximum operating pressure, dormancy time, wall material and tank architecture, on the performance of LH_2-powered aircraft, while providing realistic LH_2 tank gravimetric efficiency values for aircraft applications.

Three potential tank designs were specified through various insulation technologies: polyurethane foam insulation; Multi-Layer Insulation (MLI) vacuum insulation; and stiffened-panel MLI vacuum insulation. An additional "higher foam insulation" design was considered, in which the tank was designed with increased insulation to mitigate venting requirements, increasing dormancy time from 12 to 24 hours. Each tank contained a fuel volume of 100 m^3, which yields an energy content equivalent to 20 tonnes of kerosene, similar to a medium-range aircraft such as the Boeing 737-800. The typical fuselage dimensions for these aircraft are approximately 4 m in diameter and 40 m in length, and utilising the full fuselage diameter for the tank results in a tank length of 9.3 m [67]. Figure 2.7a shows the gravimetric efficiency of each tank design with respect to the tank radius, while Figure 2.7b shows the dependence of the design maximum operating pressure on the gravimetric efficiency. Both the tank radius and maximum operating pressure have a significant effect on the resulting gravimetric efficiency, while the length of the tank shows a weaker dependency [67].

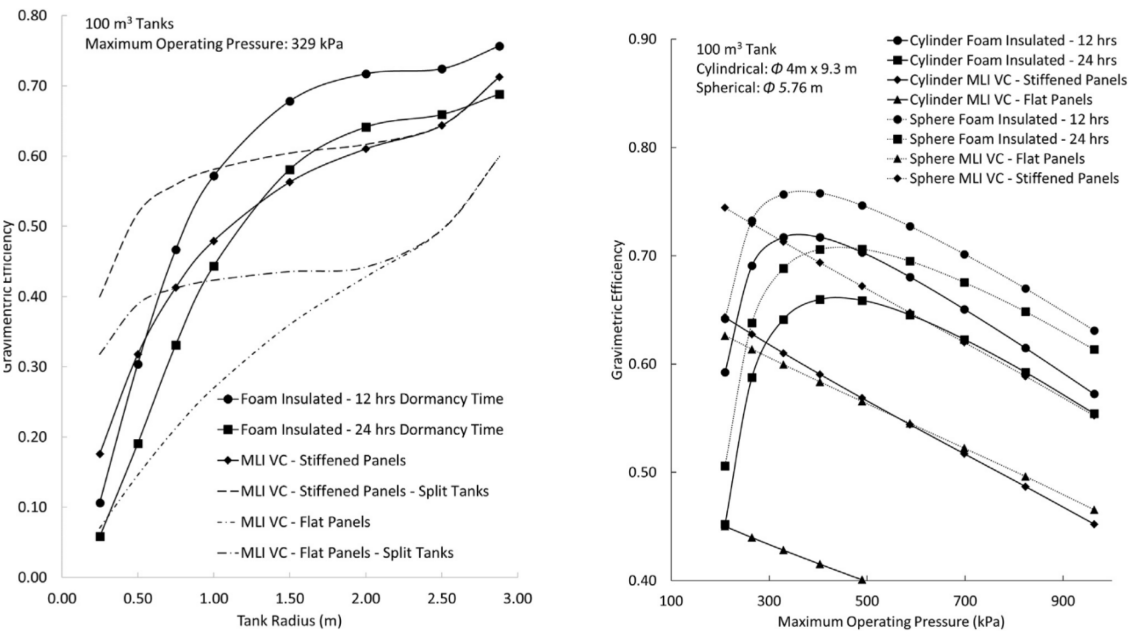

(a) (b)

Figure 2.7: Dependency of tank gravimetric efficiency on (a) Tank radius (b) Maximum operating pressure [67]

Huete and Pilidis [67] concluded that optimal tanks are those with a maximum diameter that can be inserted into the fuselage. For all ranges above regional aircraft, the gravimetric efficiencies of LH_2 tanks were calculated to be higher than 66%, suggesting that the main challenge in the design of an LH_2-powered aircraft is the volume of the tank, rather than the weight [67]. Further recommendations include the use of a foam insulated tank design for tanks with diameters larger than 2 to 3 metres [67]. Although foam insulation offers a lightweight solution for thermal protection, its application requires careful consideration of moisture and gas ingress, cryopumping, thermal cycle-induced cracking or debonding, environmental durability, and the need for protective barriers to maintain insulation performance and structural integrity over repeated service cycles [69].

2.3.3 Combustion

Similarly to combustion with traditional hydrocarbon fuels, hydrogen combustion uses a gas turbine to convert heat energy to usable thrust. The combustion of hydrogen completely eliminates CO_2 and CO emissions, which is an impossible feat with Jet A-1. However, other harmful greenhouse gas emissions such as NO_x remain a concern for hydrogen combustion. Other issues include stability, reliability, and safety. Hydrogen has properties that are vastly different from Jet A-1, where the combustion properties are summarised for each fuel in Table 2.4. The significantly higher flame speed of hydrogen can cause problems with traditional combustors, as the flame can propagate upstream of the combustor to pre-mixed zones which are not designed to withstand high heat [70]. Lower flammability limits can also create additional safety hazards that require changes in plant procedure [70];

however, the wider flammability range also allows stable combustion at leaner equivalence ratios (combustion below the stoichiometric ratio), achieving lower flame temperatures and thus reducing NO_x emissions [71, 72].

Table 2.4: Combustion properties of hydrogen and Jet A-1 [71]

Property	Hydrogen	Jet A-1
Flame speed (m/s)	2.65–3.25	0.18
Adiabatic flame temperature (K)	2318	2200
Autoignition temperature (K)	858	> 500
Flammability limits in air (vol%)	4–75	0.6–4.7

Despite the substantial differences between hydrogen and conventional hydrocarbon fuels, hydrogen combustion using existing gas turbine architectures has been shown to be technically feasible. General Electric (GE) has extensive experience with hydrogen combustion in stationary gas turbines, including operation with hydrogen fuel fractions exceeding 90% [70]. More recently, Rolls-Royce demonstrated 100% hydrogen combustion using a regional aircraft jet engine under ground-based, low-speed operating conditions [73]. However, such demonstrations have been largely confined to stationary power generation or controlled test environments. Challenges related to combustion instability, auto-ignition, and operability across the full flight envelope have so far prevented comprehensive in-flight demonstrations of hydrogen-fuelled propulsion.

Micro-mixing is a novel combustion technique proposed for hydrogen throughout the recent literature [74, 75]. Micro-mixing uses the stability of diffusion flames while maintaining low NO_x emissions through a low residence time (i.e., shorter flame time) of the high-temperature flames produced. The residence time of these flames is kept small due to the minute nature of the flames that rapidly dissipate heat, eliminating the requirements for water injection [76]. GE's recent tests demonstrated stable combustion capabilities with up to 50% hydrogen by volume [70], while other studies on hydrogen micro-mixing emissions demonstrated low NO_x exhaust emissions at a value of 2.5 ppm at the design point [75]. Khandelwal et al. [72] reported up to 80% reductions in NO_x for hydrogen combustion with lean-mixture technology without large reductions in combustion efficiency.

2.3.4 Aircraft Design

In order to analyse the performance of LH_2-powered aircraft, conceptual design techniques must be used to develop an appropriately sized aircraft for the Top-Level Aircraft Requirements (TLAR), which describe the requirements in terms of the desired passenger count and design mission range. Due to the change in aircraft design when transitioning to LH_2 propulsion, such as the change in the weight and volume of the aircraft due to the integration of the LH_2 tanks, it is necessary to re-design the fuselage, wings, empennage, and landing gear of the aircraft. Specifically, the fuselage must be extended to account for the LH_2 tank integration, the wings and engine must be re-sized to ensure sufficient lift and thrust is produced at take-off, and the empennage must be re-sized to ensure adequate control of the aircraft in terms of the pitch and yaw capabilities.

Mukhopadhaya and Rutherford [65] used a simplified design approach in their analysis of hydrogen powered aircraft using the Stanford University Aerospace Vehicle Environment (SUAVE), maintaining constant wing loading (W/S), Thrust-to-Weight (T/W) ratio, and tail volume coefficients (V_H, V_V). A constant wing loading ratio, which is described in Equation 2.2, ensures that the wing area increases or decreases in proportion to the change in the Maximum Take-Off Weight (MTOW) of the aircraft relative to the baseline design. Similarly, the T/W ratio, described in Equation 2.3, ensures that the thrust is scaled proportionally to the change in MTOW.

$$\left(\frac{W}{S}\right) = \frac{MTOW}{S} \tag{2.2}$$

$$\left(\frac{T}{W}\right) = \frac{T}{MTOW} \tag{2.3}$$

The tail volume coefficient is a measure of the stability and control authority of the horizontal and vertical stabiliser relative to the wing [77]. Using Equations 2.4 and 2.5, the required change in the horizontal and vertical stabiliser area can be calculated to maintain a constant tail volume coefficient relative to the baseline aircraft, where S_H and S_V represent the horizontal and vertical tail area, respectively, l_H and l_V is the distance from the Centre of Gravity (CG) to the aerodynamic centre of the horizontal and vertical tail, respectively, and $\bar{c}$ is the mean aerodynamic chord of the wing. In this design, an extended fuselage was not considered as the authors opted for a reduced passenger capacity to fit the LH_2 tank within the baseline fuselage design. The final LH_2 tank was sized using a fixed gravimetric efficiency of 0.35 within an iterative loop until convergence was achieved for the MTOW and fuselage length, where weight estimates were obtained using NASA's Flight Optimisation System (FLOPS) software [65].

$$V_H = \frac{S_H \cdot l_H}{S_W \cdot \bar{c}} \tag{2.4}$$

$$V_V = \frac{S_V \cdot l_V}{S_W \cdot b} \tag{2.5}$$

Karpuk and Elham [78] used a more complex design approach, coupling low-fidelity constraint-based pre-sizing with higher-fidelity aerodynamic and weight estimation tools, as illustrated in Figure 2.8. The sizing loop began with a constraint diagram to generate feasible combinations of W/S and T/W ratios, and the SUAVE tool was used for mission simulation and propulsion analysis for a selected design point to compute the hydrogen fuel requirement. This was followed by fuselage re-sizing to account for the LH_2 tank length, and the updated configuration was simulated again to determine the required wing area and thrust, which was iterated until the MTOW converged. NASA's FLOPS tool was used for weight estimations, in combination with the Elham Modified Weight Estimation Technique (EMWET) to refine the wing structural mass to account for the UHAR wing design [78]. The weight of the fuel system was calculated using a bottom-up approach following the method described by Brewer [79], rather than using a fixed gravimetric efficiency.

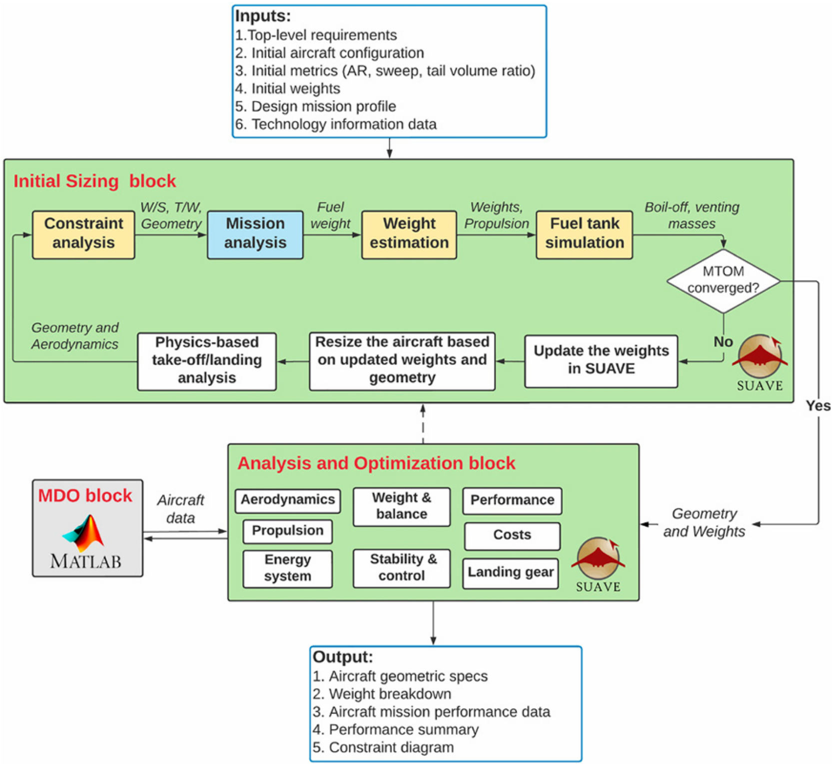

Figure 2.8: Hydrogen aircraft sizing procedure employed by Karpuk and Elham [78]

2.3.5 Aircraft Performance

Verstraete [68] analysed short-, medium-, and long-range hydrogen aircraft using FLOPS and GasTurb. The study incorporated fuselage-integrated cryogenic tanks with gravimetric efficiencies ranging from 57% to 76% for short- and long-range configurations, respectively. Hydrogen propulsion achieved a 3% thermal efficiency gain but incurred a 6% fuselage weight penalty [68]. Results showed that the long-range hydrogen aircraft consumed 12% less energy per seat-kilometre for its design mission than its kerosene counterpart due to the substantial reduction in fuel weight (44.5 t vs. 138 t). In contrast, short- and medium-range hydrogen aircraft exhibited energy penalties of 18% and 5% for their design missions, respectively, as structural weight dominated over fuel savings. Verstraete concluded that long-range hydrogen aircraft offer the greatest energy benefit, while smaller aircraft are less efficient [68]. The study also found that 'top tank' configurations could increase energy use by 6–19% compared to configurations with front/aft tanks inserted within the original fuselage diameter [68].

The Clean Sky report [9] presented evolutionary hydrogen concepts for a range of aircraft classes. It found reductions in the energy demand for commuter and regional aircraft, but increases of 22–42% for medium- and long-range designs relative to conventionally-powered aircraft for the design mission. Despite higher Cost per Available Seat Kilometre (CASK) values, hydrogen performed better economically than synthetic SAF in short-range applications [9]. The divergence from the trends observed in the work of Verstraete [68] was due to differences in the airframe geometry, range, and assumed tank gravimetric efficiency —particularly the single-deck, 10,000 km long-range design which used a 38%

tank gravimetric efficiency (compared to the 76% value used by Verstraete [68]), which increased the take-off weight by 23%.

Mukhopadhaya and Rutherford [65] recognised that the full design mission range is rarely used for conventional aircraft such as the A320neo, and instead focused on developing a shorter-range LH_2 aircraft capable of achieving >80% Revenue Passenger Kilometre (RPK) coverage relative to the baseline aircraft. It was argued that reducing the maximum range of LH_2 aircraft offers a better balance between market coverage and energy efficiency, as the weight penalties for the fuel system increase disproportionately with increasing maximum range [65]. With gravimetric efficiencies of 20–35%, hydrogen variants exhibited higher energy intensity (0.91–1.09 MJ/RPK) and lower range than conventional aircraft, but remained cost-competitive against synthetic SAF for missions up to 3,400 km [65]. Under projected 2050 conditions, green hydrogen could achieve a lower CASK than synthetic SAF or blue hydrogen given carbon pricing of \$100–\$275 per tonne of CO_2 [65]. Moreover, the authors showed that a family of 150-, 168-, and 192-seat aircraft, even under conservative gravimetric efficiency assumptions, could capture most of the RPK coverage of the conventional A320neo, as illustrated in Figure 2.9.

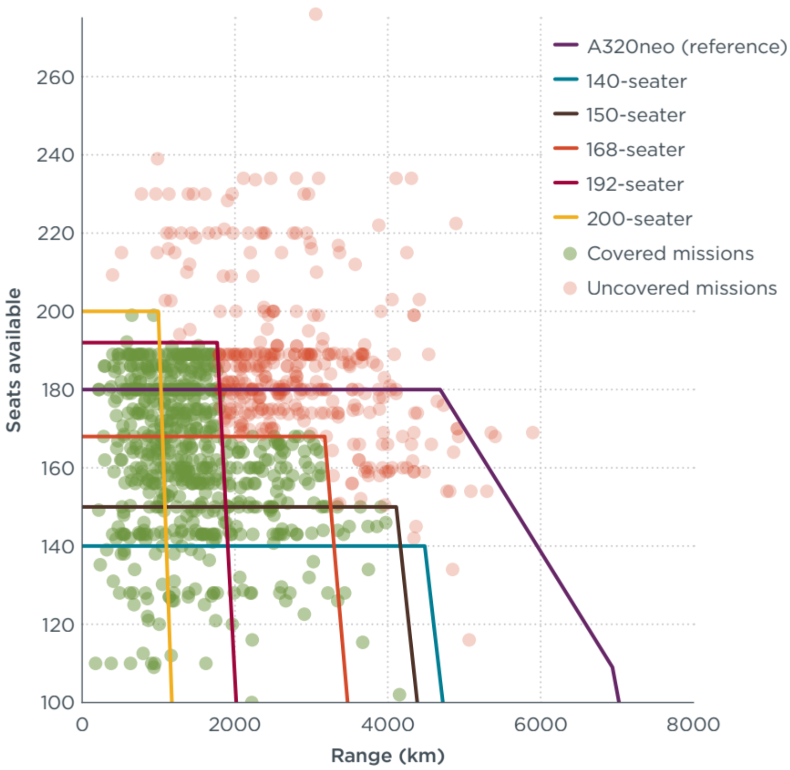

Figure 2.9: 2019 narrow-body missions compared to the payload-range capability of an LH_2-powered narrow-body (GI = 0.275) [65]

Karpuk and Elham [78] extended this analysis by incorporating advanced airframe and propulsion technologies (laminar flow, load alleviation, and UHBPR turbofans). It was found that hydrogen propulsion provided the greatest emission reduction potential with up to 63% lower lifecycle CO_2 equivalent emissions, but at a cost penalty relative to kerosene [78]. The results indicated that, although hydrogen delivers the greatest climate benefit, kerosene or sustainable aviation fuels may remain more economically favourable in early aircraft generations [78]. However, the study primarily evaluated performance at the design mission, supplemented by limited sensitivity analyses rather than comprehensive off-design mission sweeps. As a result, it is difficult to draw firm conclusions about optimal configurations when the performance of the missions most frequently operated was not explicitly assessed.

In summary, the performance of hydrogen aircraft is strongly dependent on mission range, tank efficiency, and technological maturity. Long-range configurations can exceed conventional aircraft in energy efficiency, while short-range aircraft remain penalised by tank weight and volume; however, this is strongly dependent on the fuel efficiency of the aircraft and the selected tank gravimetric efficiency. As airframe and propulsion advances continue, the environmental advantages of hydrogen could outweigh its structural and cost challenges, especially when compared with sustainable but energy-intensive synthetic SAF. In addition, excessive focus has been placed on design mission performance in the literature. As stated by Mukhopadhaya and Rutherford [65], a balance should be found between market coverage and energy efficiency of the aircraft design, where off-design mission analysis should be conducted to determine an optimal balance.

2.3.6 Engine Cycle Enhancements

Intercooling & Recuperation

Although the introduction of LH_2 is generally expected to reduce aircraft performance compared to conventionally-fuelled designs, LH_2-powered aircraft have the potential to increase thermodynamic performance within the engine through intercooling and recuperation systems. In contrast to traditional hydrocarbon fuels, LH_2 offers a significant temperature gradient between the fuel and the compressor air temperature and core exhaust flow temperature, allowing high rates of heat transfer. In addition, hydrocarbon fuels suffer from coking limits at approximately 400 K [80], limiting the available enthalpy transfer to the fuel within the system. These limitations of hydrocarbon fuels mean that the additional mass and pressure losses incurred by intercooling and recuperation systems cannot be justified for conventional engine designs [25].

Intercooling reduces the temperature of the working fluid between compressor stages, reducing the High-Pressure Compressor (HPC) work requirement, while also reducing NO_x formation through lower combustion temperatures [80]. Figure 2.10 illustrates a worked example that outlines how intercooling reduces the specific work of the HPC, where T_{t_i} represents the total air temperature at station i, the subscript IC denotes parameters related to the intercooled case, W_c is the specific work of the compressor, c_p represents the specific heat capacity of the working fluid at constant pressure, and γ is the ratio of specific heat values. Assumptions within the worked example include ideal compressors, perfect gas, no pressure loss, and a temperature reduction from T_{t_2} to $T_{t_{2-IC}} = 300$ K, resulting in a 12% reduction in the total compressor specific work.

Recuperation takes advantage of the higher temperatures available in the core exhaust

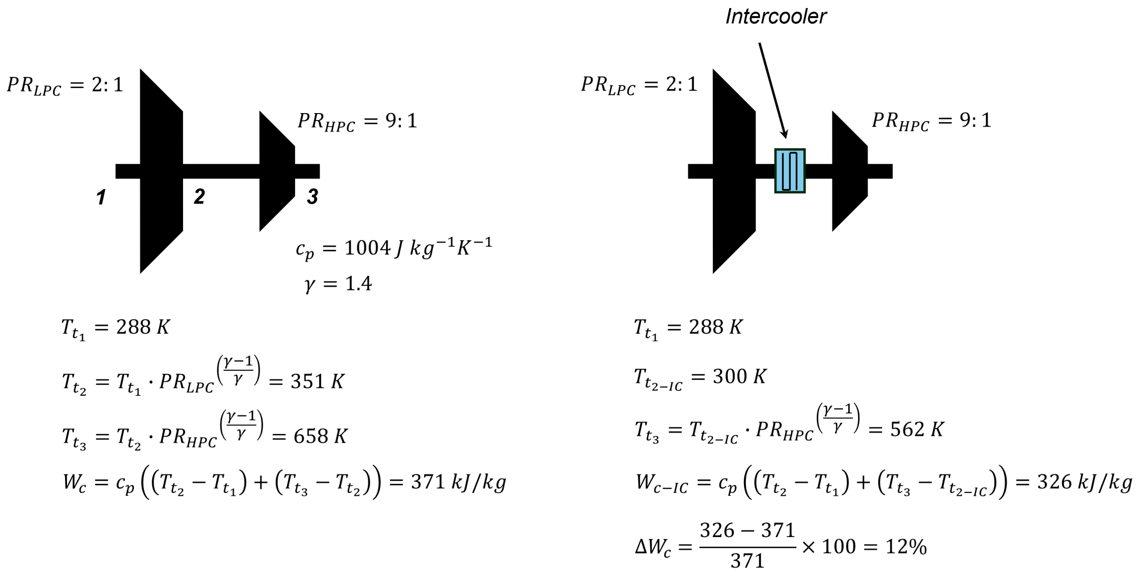

Figure 2.10: Worked example describing the reduction in compressor specific work as a result of intercooling

to further increase the enthalpy of the fuel, thus reducing the required fuel-flow to achieve the desired combustor inlet temperature [25]. This is described by the fuel-energy balance described in Equation 2.6, where T_{t_4} is the turbine inlet temperature (constrained by material limits), and $T_{t_{3-RC}}$ is the effective combustor inlet temperature, which is increased by the temperature rise due to recuperation ($\Delta T_{t_{RC}}$) as outlined in Equation 2.7.

$$\dot{m}_{fuel} \cdot \text{LHV} = \dot{m}_{air} \cdot c_p \left(T_{t_4} - T_{t_{3-RC}}\right) \tag{2.6}$$

$$T_{t_{3-RC}} = T_{t_3} + \Delta T_{t_{RC}} \tag{2.7}$$

Design & Performance

Figure 2.11 shows an example of an Intercooled-Recuperated Engine (IRE) design highlighting the increase in fuel temperature throughout the system, which provides thermodynamic benefits by reducing the required compressor work, reducing the temperature of the turbine cooling air, and increasing the enthalpy of the fuel through heat transfer from the core exhaust flow [81].

LH_2 IRE designs have been developed and analysed in recent literature [82, 81]. Görtz and Silberhorn [82] developed an LH_2 IRE engine for a short-range aircraft with an expected EIS of 2040, separately evaluating the achievable TSFC benefits of the intercooling and recuperation systems. This was performed using a 1D engine model combined with idealised ϵ-NTU Heat Exchanger (HEX) models and simplified pressure-loss assumptions, enabling an assessment of thermodynamic potential but without geometric or aerodynamic constraints. Their results showed that intercooling yielded the greatest performance improvement, enabling a higher OPR and reducing TSFC by 4.6% during cruise, followed by exhaust-based recuperation, which reduced TSFC by 2.9% relative to the conventional

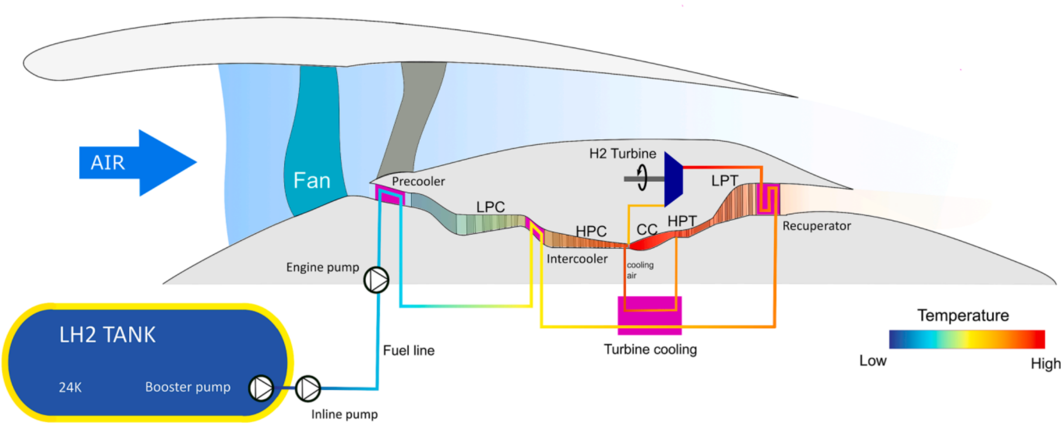

Figure 2.11: Example of a heat management system for a turbofan engine featuring intercooling, recuperation, and cooled turbine cooling air [81]

hydrocarbon-fuelled baseline [82].

Patrão et al. [81] presented a multi-fidelity analysis of compact heat exchangers for LH_2 turbofan engines, demonstrating that combined intercooling and recuperation provide substantial thermodynamic benefits enabled by the cryogenic temperature of LH_2. The higher-fidelity modelling approach combined ϵ-NTU HEX modelling, geometry-dependent correlations, a CFD-based duct optimisation, and full cycle re-evaluation including realistic pressure losses derived from Kays and London [83] and material constraints [81]. This study resulted in the optimised compact HEX duct design illustrated in Figure 2.12, which added 326 kg additional mass to the engine. The final IRE configurations achieved reductions of up to 7.7% TSFC at take-off, 5.3% at cruise, and a 5.5% reduction in mission fuel burn, primarily driven by reduced compressor work and fuel enthalpy gain [81]. In addition, NO_x reductions of up to 37% were achieved due to the reduced combustor inlet temperature and equivalence ratio [81].

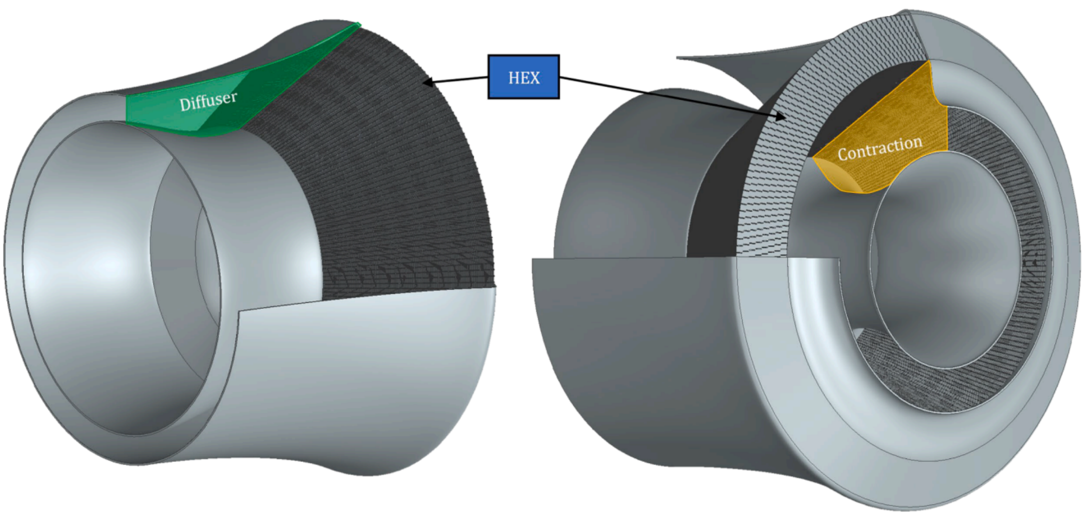

Figure 2.12: Concept illustration of compact HEX intercooler for LH_2 propulsion [81]

The results confirm that LH_2 enables compact, high-effectiveness intercoolers and recuperators that are infeasible with conventional kerosene systems, providing strong justification for integrating IRE concepts into future hydrogen aircraft. However, similar to previous analyses of LH_2-powered aircraft, the studies by Patrão et al. [81] and Görtz and Silberhorn [82] focus solely on design-mission performance and do not consider off-design missions, which represent the majority of real-world aircraft utilisation [84].

2.4 Sustainable Aviation Fuels

2.4.1 Fuel Types

SAF is essentially identical to traditional jet fuel; however, the key benefit of SAF is the reduction of lifecycle CO_2 emissions, which can range from 69–95% reductions for biofuels [85] and up to 96% for synthetic SAF produced using Direct Air Capture (DAC) [86, 87]. Biofuels can be further categorised by the various American Society for Testing and Materials (ASTM) pathways based on the feedstock used during production, as illustrated in Figure 2.13. The Hydrogenated Esters and Fatty Acids (HEFA) pathway converts oils and fats to SAF, where potential feedstocks include used cooking oil and animal/plant waste fats and oils. HEFA is the only SAF pathway in commercial use today, mainly due to the low initial investment capital required for production [30]. The cost and availability of feedstocks is critical for this pathway; growing limitations in available feedstocks mean that this pathway is likely to dominate the SAF market in the early years, but will subsequently contribute a much smaller portion of the overall production mix in the long term [30]. This has already been observed in recent years, as several HEFA-SAF plants have begun production [88].

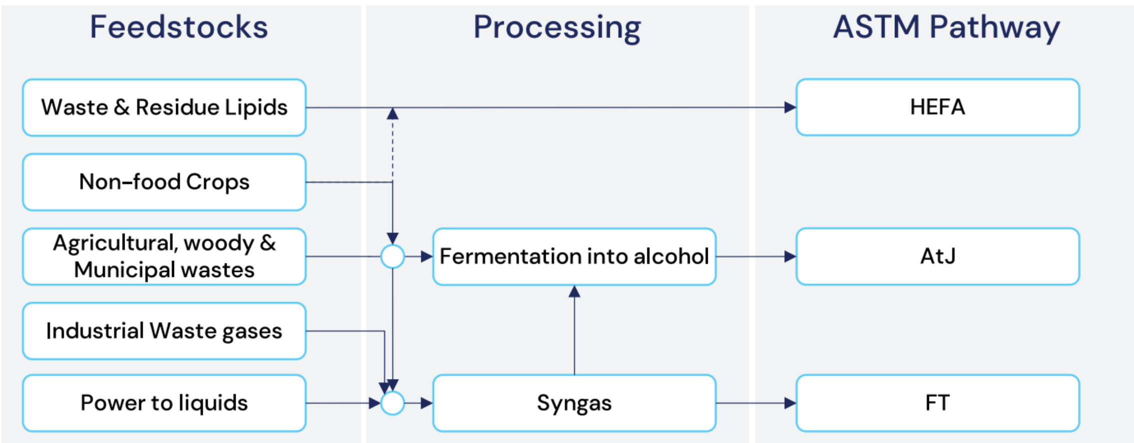

Figure 2.13: Summary of ASTM pathways for Sustainable Aviation Fuels [30]

Alcohol-to-Jet (AtJ) requires conversion of feedstocks to alcohol, followed by the AtJ process to produce SAF. Lower feedstock costs result in a more even split of production costs between feedstock and infrastructure, along with greater flexibility in feedstock, which mitigates the risk of feedstock shortages [30]. The Fischer-Tropsch (FT) pathway gasifies feedstocks to produce syngas, which can be converted to fuels via the FT reactions. Similarly to the AtJ pathway, a wide variety of low-cost feedstocks can be used for FT-produced

SAF. However, the FT pathway additionally allows carbon captured from the atmosphere to be synthesised with green hydrogen to produce synthetic SAF [30, 29]. Table 2.5 summarises the pathways in terms of stage of development, described by Fuel Readiness Level (FRL), along with the range of potential emission reductions and current certified blending ratios. The projected price of various SAF pathways relative to Jet A-1 is illustrated in Figure 2.14, highlighting the significant cost of PtL SAF compared to alternative biomass pathways.

Table 2.5: Summary of ASTM pathways for Sustainable Aviation Fuel production [87, 30, 88]

SAF Type	Blending Ratio	Emission Reduction	FRL
HEFA	50%	53–79%	9
AtJ	50%	30–67%	7
FT	50%	56–95%	7
PtL	50%	90–96%	7

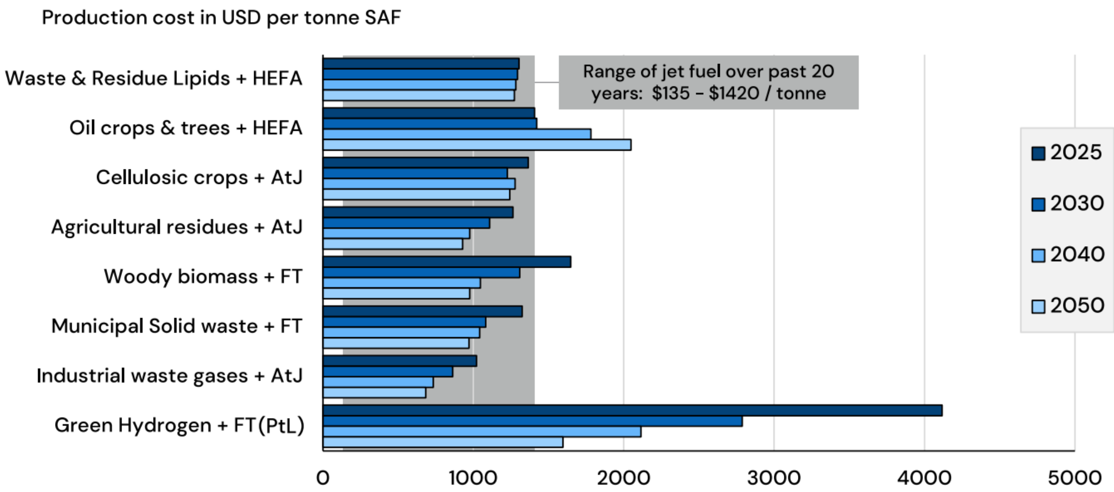

Figure 2.14: Projected price of selected SAF pathways from 2025 to 2050 [30]

2.4.2 Production and Availability

The current uptake of SAF represents an extremely small proportion of the total fuel consumption in aviation, on the order of 0.1% [89]. This is mainly due to the limited availability of SAF and lack of demand due to high costs. SAF producers have been reluctant to invest significant capital to produce the required volumes as the production technology is not mature, making operations prohibitively expensive [90]. The European Commission [91] recently proposed a mandate of 5% SAF (as a share of aviation fuels), with a sub-target of 0.7% synthetic SAF, for aviation fuel consumed in the EU by 2030 as part of the ReFuelEU directive. The proposed SAF target increases to 63%, with a minimum of 28% synthetic SAF by 2050 [91]. These policy directives are expected to provide the initial support required to develop SAF production technologies by mitigating the risk of investment and reducing the cost of production as the technology matures.

Ploetner et al. [87] conducted a study on the projected SAF uptake required to meet the ATAG goal of halving global emissions by 2050 relative to 2005 levels. Figure 2.15 shows projections of the SAF production capacity for the various ASTM pathways, where HEFA was projected to be the main source of SAF in the near term, while Thermochemical Conversion Technologies (TCT), equivalent to the FT pathway, were projected to supply the majority of SAF in the medium term, while the PtL pathway was expected to be the dominant source in the long-term [87]. These projections were based on the FRL of each technology and the feedstocks available for each pathway, which are significantly limited for HEFA and are expected to become limited for TCT/FT beyond 2035 [87].

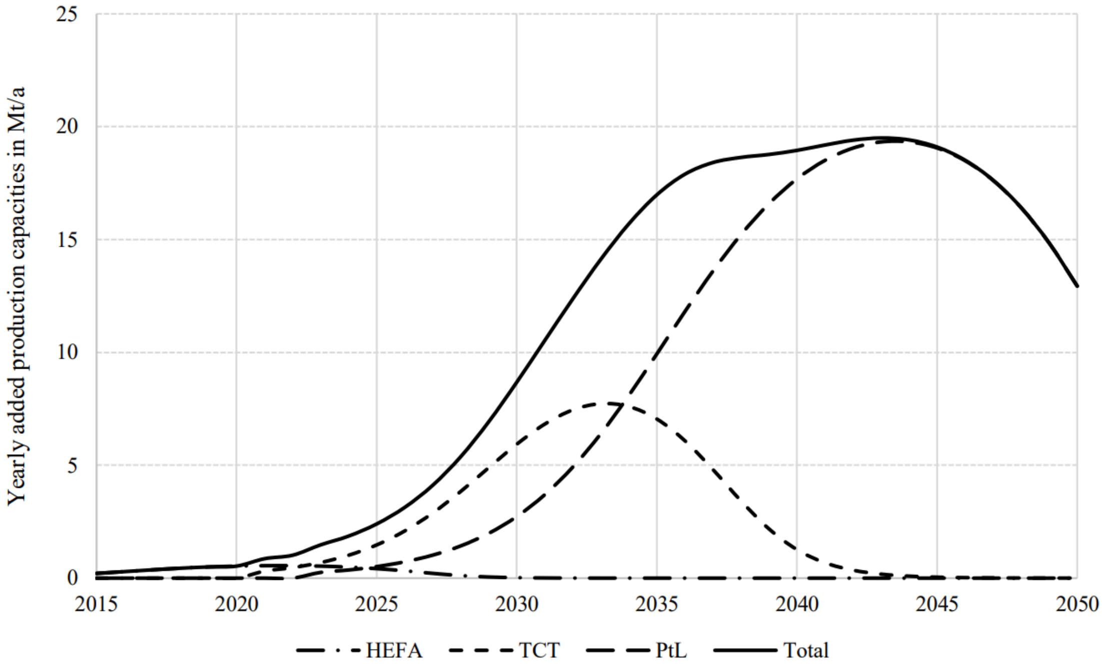

Figure 2.15: Projected production capacities for different Sustainable Aviation Fuel pathways [87]

Given the projected increase in SAF production capacity, estimates of the cumulative investment required to meet these targets were provided [87]. Up to 4 trillion euro could be required for the total production requirements of SAF towards 2050, the majority being spent on the PtL pathway from 2035 onward [87]. PtL requires a large investment due to the high capital costs associated with electrolysis and the FT process, together with the high operating costs resulting from the low efficiency of the fuel conversion process [92, 29]. Projections by Zhou et al. [92] estimate that synthetic SAF may not be cost competitive with jet fuel even in 2050, potentially further contributing to investment cost through government subsidies. Given the considerable cost burden of SAF, there is a growing incentive to develop more fuel-efficient aircraft. Reducing mission fuel burn directly reduces the dependence on costly low-carbon fuels, enabling investments in advanced aircraft technologies to be recouped through long-term SAF cost savings.

2.4.3 Power-to-Liquid

Bio-derived SAF feedstocks are expected to become limited in the coming decades, and are therefore not considered sustainable in the long term [93, 94, 95]. Hence, synthetic SAF, or PtL SAF, is expected to become the primary source of decarbonisation during the pathway to net-zero. Although PtL fuels offer a highly sustainable pathway for reducing aviation emissions when produced using DAC and renewable electricity, the scale of electricity required remains a major challenge due to low conversion efficiencies (typically 22—46% [9, 65, 29]). For example, approximately 10,734 TWh of renewable electricity was generated globally in 2025 [96], while commercial jet fuel demand was projected to be around 3,700–3,800 TWh [97]. Replacing this demand with PtL SAF would therefore require renewable electricity equivalent to approximately 70–140% of current global renewable generation, assuming production efficiencies in the range of 25–50%.

DAC is an extremely energy-intensive process in the production of PtL SAF. DAC involves the absorption of CO_2 from the air or from processes that emit CO_2 at high concentrations, such as industrial flue gases or biogenic processes such as fermentation [98]. The International Transport Forum [98] performed an analysis to represent the physical scale of atmospheric DAC required to extract the total of aviation emissions in 2019, which amounted to 1035 Mt of CO_2. Each aircraft in the global fleet was found to require 80 state-of-the-art DAC units operating 24/7, which would require between 6000 and 17,200 solar panels with an area of 36 m^2 each, to supply the renewable electricity demand, depending on the availability of waste heat [98]. The size comparison for these DAC infrastructure requirements in comparison to a Boeing 737-900 aircraft is presented in Figure 2.16. This analysis further highlights the monumental scale of renewable electricity required for the production of synthetic SAF, noting that this analysis considers only the DAC infrastructure, ignoring the energy and infrastructure required for the hydrogen production and the FT process.

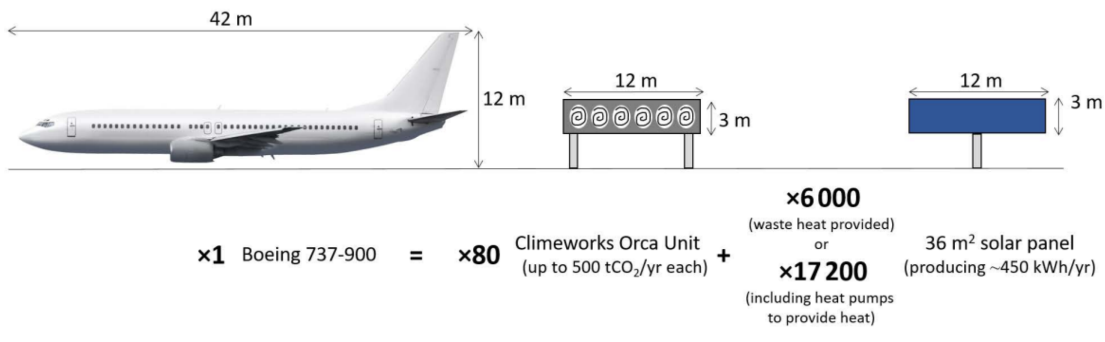

Figure 2.16: Size comparison between a Boeing 737-900 and the average DAC infrastructure required per aircraft [98]

Therefore, no single alternative fuel offers a universally optimal decarbonisation pathway. While hydrogen presents substantial infrastructural and design challenges, the high energy demand associated with SAF production may, in some scenarios, outweigh these drawbacks.

2.5 Non-Carbon Emissions

Previous sections have focused on technological developments in aircraft that reduce carbon emissions through improved fuel efficiency or the use of alternative low-carbon fuels. However, as discussed in Section 1.1.5, carbon emissions only represent a portion of anthropogenic emissions within aviation. Nitrogen oxides and contrail formation are a significant cause of global warming, while other emissions such as PM, SO_2 and H_2O also contribute to global warming to a lesser extent [12], as highlighted by the climate forcing metrics of various emissions presented in Figure 2.17. The following sections focus on the physical formation mechanisms and modelling approaches related to NO_x emissions and contrail formation, along with non-volatile Particulate Matter (nvPM) emissions which contribute to contrail formation [16].

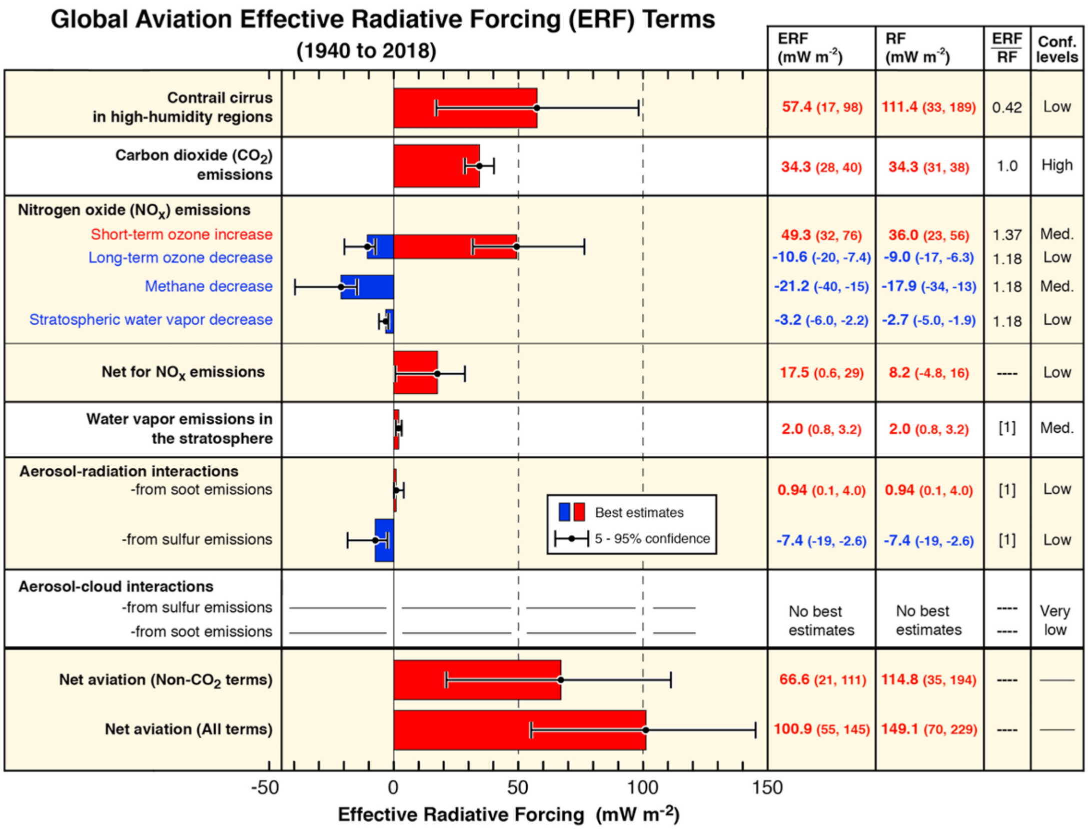

Figure 2.17: Best-estimates for climate forcing terms from global aviation from 1940 to 2018 [12]

2.5.1 Nitrogen Oxides

Nitrogen oxides are the most significant non-carbon emissions from aircraft, primarily formed through high-temperature reactions between atmospheric nitrogen and oxygen in the combustor. Their formation rate depends strongly on local flame temperature, residence time, and fuel–air stoichiometry, making accurate prediction sensitive to both engine design and operating conditions. Several formation pathways contribute to total NO_x production, of which the thermal (Zeldovich) mechanism dominates under typical gas turbine conditions in the post-flame region where the flame temperature is above 1800 K [99, 100]. In addition, prompt nitrogen oxide formation occurs in low-temperature hydrocarbon combustion due to the reaction of hydrocarbon radicals with molecular nitrogen [99, 100].

Combustor Design

Thermal Nitric Oxide (NO) formation is the dominant mechanism for gas turbines and is primarily influenced by the equivalence ratio within the combustion chamber. The equivalence ratio ϕ, defined in Equation 2.8, describes the ratio between the combustor Fuel-Air Ratio (FAR) and the stoichiometric FAR (FAR_{st}). Figure 2.18 illustrates the dependence of the equivalence ratio on the flame temperature and the thermal NO formation. It can be observed that the peak flame temperature occurs when the equivalence ratio is slightly above one, whereas maximum thermal NO formation rates occur when the equivalence ratio is below one. This is due to the increase in oxygen concentration under lean conditions, which enables higher reaction rates between nitrogen and oxygen.

$$\phi = \frac{FAR}{FAR_{st}} \tag{2.8}$$

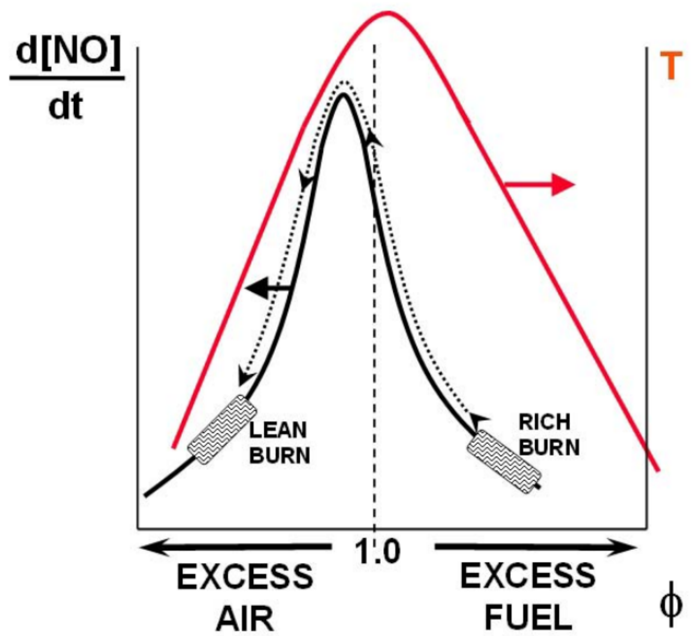

Figure 2.18: Relationship of equivalence ratio, nitric oxide formation and combustion temperature, where RQL combustion strategy is highlighted by the dotted line [101]

The Rich-Quench-Lean combustor, illustrated in Figure 2.19, was designed to reduce NO_x production by using a rapid 'quench' zone. Air is injected into the combustion chamber to rapidly transition from a rich to a lean mixture, minimising the time spent near stoichiometric conditions where both temperature and oxygen availability are highest, and thermal NO formation peaks [101]. This RQL combustion strategy to minimise NO formation is illustrated by the dotted line in Figure 2.18.

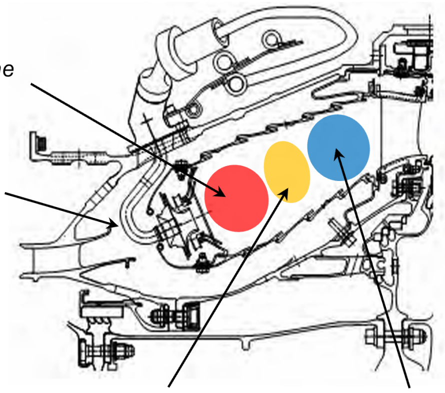

Figure 2.19: Diagram of RQL combustor with illustration of combustion process, adapted from [102]

The Twin Annular Premixing Swirler (TAPS) combustor, developed by GE as a successor to RQL designs, is illustrated in Figure 2.20. This combustor employs a fundamentally different approach to NO_x reduction by maintaining a lean-premixed flame throughout most of the operating range, rather than transitioning from rich to lean combustion. While RQL combustors minimise thermal NO_x by initially operating under fuel-rich conditions followed by a rapid transition to lean conditions, the TAPS concept prevents the formation of high-temperature stoichiometric zones throughout its operation [102]. Each TAPS injector consists of a central pilot fuel nozzle, with concentric main nozzles: the central pilot stage operates fuel-rich at low power to ensure stable combustion, while at higher thrust settings (above approximately 30% power), fuel is distributed to the lean-premixed main stage to enable lean combustion [99]. By premixing fuel and air prior to combustion, the TAPS design achieves more uniform flame temperature and oxygen distribution, reducing both peak flame temperatures and NO formation rates [102]. Full-annular and sector tests within the FAA CLEEN programme demonstrated that the TAPS-II design achieved up to 60% lower NO_x emissions relative to the CAEP/6 limit, with additional benefits of near-zero smoke and high combustion efficiency throughout the flight envelope [102].

Empirical Models

A wide range of modelling approaches have been developed to estimate NO_x formation, ranging from empirical correlations based on certification data to physics-based and chemistry-resolved methods capable of representing detailed kinetics. The most widely used methods are empirical or semi-empirical correlation methods, such as the P3-T3 method, Boeing Fuel-Flow Method 2 (BFFM), and the DLR method. The P3-T3 method described by Dubois and Paynter [103] uses the NO_x emission data within the ICAO Emissions Databank (EDB) to obtain reference NO_x values at Sea-Level Static (SLS)

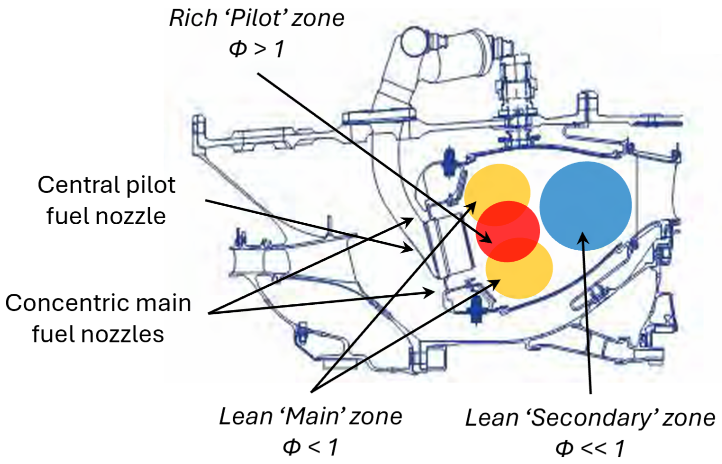

Figure 2.20: Diagram of TAPS-II combustor with illustration of combustion process, adapted from [102]

conditions, which are then corrected according to the engine performance parameters at altitude. Equation 2.9 describes the calculation used to obtain NO_x predictions using the P3-T3 method using the combustor inlet pressure (p_{t_3}), combustor inlet temperature (T_{t_3}), and FAR parameters, along with a humidity correction factor H which is described in the work of Aygun and Turan [104]. The reference values used in Equation 2.9 are obtained using a second-degree polynomial interpolation with respect to the T3 values, which is described in further detail by Awde and Stuart [34].

$$NO_{x,\,alt} = NO_{x,\,ref} \cdot \left(\frac{p_{t_{3,\,alt}}}{p_{t_{3,\,ref}}}\right)^{y} \cdot \left(\frac{FAR_{alt}}{FAR_{ref}}\right)^{z} \cdot e^{H} \tag{2.9}$$

BFFM is a simplified method that was developed to eliminate the need for the component-level thermodynamic properties required for the P3-T3 method [103]. A derivation was presented to develop the empirical equation described in Equation 2.10, which generates NO_x emission predictions by correcting the SLS EDB NO_x values using the engine fuel-flow values along with the ambient temperature and pressure values [103]. The $NO_{x,ref}$ values are obtained by interpolating a log-log fit of the EDB NO_x values against fuel-flow data, where fuel-flow factors are applied to the fuel-flow values of each SLS operating point to account for installation effects, and a reference fuel-flow value is used in the interpolated log-log plot to account for the change in ambient conditions and flight speed [103]. The DLR NO_x prediction method, described by Schaefer and Bartosch [105], follows a similar approach to the BFFM. The key differences are in the interpolation method, which uses a second-degree polynomial, and the pressure and temperature corrections are calculated using total rather than static conditions. Furthermore, no fuel-flow correction factors are applied to account for installation effects. The NO_x calculation for this method is presented in Equation 2.11, where a reference fuel-flow value is used for interpolation [105].

$$NO_{x,\,alt} = NO_{x,\,ref} \cdot \left(\frac{\delta_{amb}}{\theta_{amb}}\right)^{0.5} \cdot e^{H} \tag{2.10}$$

$$NO_{x,\,alt} = NO_{x,\,ref} \cdot \delta_{amb,\,t}^{0.4} \cdot \theta_{amb,\,t}^{3} \cdot e^{H} \tag{2.11}$$

Awde and Stuart [34] presented a comparative evaluation of each empirical method and found that the P3-T3 and BFFM methods showed the best agreement with the ICAO NO_x values, resulting in error bands of 10%, compared to 20% for the DLR method. This study combined real-world flight data with meteorological data obtained from the MERRA-2 datasets [106] to generate realistic in-flight NO_x emission predictions [34]. However, the ICAO have highlighted potential concerns related to methods utilising the ICAO EDB due to the large uncertainties present in mid-power cruise operations [107], as the EDB only measures emissions for ground operations at power levels of 7%, 30%, 85% and 100%. Proposals have been suggested for a mid-power testing point at 57.5% power [107], which would greatly reduce the uncertainty in this region and improve the accuracy of empirical-based methods. However, in the absence of this mid-power data point, higher-fidelity physics-based methods may offer greater accuracy for NO_x emission modelling.

Physics-Based Models

At higher fidelity, Computational Fluid Dynamics (CFD) coupled with finite-rate chemistry directly resolves turbulent flow, mixing, and reaction kinetics within the combustor [100]. Large Eddy Simulation (LES) and Reynolds-Averaged Navier–Stokes (RANS) approaches coupled with turbulence models, implemented with detailed or reduced NO_x sub-mechanisms, have been widely applied in research to capture local flame structure and predict spatial NO_x distributions [99]. However, the high computational cost of these 3D simulations limits their use in full-engine or mission-level studies.

Chemical Reactor Network (CRN) models have gained traction as a potential solution for bridging the gap between empirical models and detailed CFD simulations. CRN models provide 1D representations of engine combustors that use combustor inlet data, along with reaction mechanisms that detail all possible chemical reactions for the fuel-air mixture, to simulate combustor performance and predict emissions at the combustor outlet [108] [100]. CRN models have been developed to model NO_x, CO, and Unburned Hydrocarbons (UHC) for RQL combustors [100] and various turbofan engines in previous work [108].

A key benefit to using physics-based combustion models is that they can be used to predict emissions for novel engine concepts, which was seen in the work of Ziaja et al. [109] who developed CRN models for a SAF-powered hybrid-electric turbofan. The ability to model alternative fuels such as SAFs is particularly important, as it is suggested that these fuels have the potential to reduce contrail formation due to their lower concentrations of aromatics and sulphur [110]. However, CRN modelling remains underdeveloped for operational analysis, as existing studies apply CRN models only at discrete operating points rather than across full mission profiles, largely due to their higher computational cost relative to empirical methods.

Surrogate Models

Data-driven surrogate models such as Gaussian process regressors or neural networks are increasingly employed to emulate the results of CRN or CFD simulations to further reduce computational cost. Recent studies have demonstrated the feasibility of constructing fast-running surrogate models to emulate the outputs of high-fidelity physics-based models. For example, Lamioni et al. [111] built a surrogate response surface from a CRN to predict NO_x emissions as a function of key parameters of a gas turbine. Similarly, Korsunovs et al. [112] developed a 'global NO_x surrogate model' derived from a multi-physics engine platform using Kriging surrogate techniques. In addition, the use of Gaussian-process and neural-network surrogate models for CFD in combustion applications has been reviewed by Zhou et al. [113]. Such hybrid approaches represent a promising direction for future NO_x prediction frameworks in aviation, offering both physical interpretability and computational efficiency. However, they have yet to be combined with large-scale physics-based mission simulations to predict non-carbon emissions for aircraft operations.

2.5.2 Non-Volatile Particulate Matter

nvPM from aircraft engines consists primarily of black carbon soot, with contributions from metal ash and oxygenated functional groups [114]. nvPM forms in locally fuel-rich regions within the combustor primary zone, followed by surface growth and coagulation as particles are convected downstream, and the emitted nvPM is highly sensitive to the local mixture fraction, flame temperature and residence time in both rich and lean regions [115]. Engine tests show that nvPM emissions increase with total aromatics, naphthalenes and fuel hydrogen content, while reduced-aromatic synthetic or bio-derived SAF blends can lower nvPM by 50–97% under cruise conditions [37]. Although nvPM emissions alone do not contribute significantly to global warming, they are a key component involved in contrail formation when the soot number emissions index exceeds a threshold of approximately $10^{14} kg^{-1}$ [16], as water vapour emitted by the engine condenses and freezes onto nvPM particles in the exhaust plume [110].

2.5.3 Contrail Formation

Condensation trails, or contrails, are line-shaped ice clouds that form in the wake of an aircraft when the hot, moist exhaust gas mixes with the cold ambient air of the upper troposphere. They arise when the water vapour emitted from the engine exceeds the local saturation vapour pressure as the exhaust cools and expands, leading first to condensation and then rapid freezing of water droplets into ice crystals [116, 36]. These processes typically occur at cruise altitudes between 8 and 13 km where temperatures are below approximately $-40\,^{\circ}\mathrm{C}$ [36]. The initial contrail forms within seconds behind the engine and can either dissipate quickly or persist depending on the ambient humidity. Persistent contrails occur when the surrounding air is ice-supersaturated (i.e., relative humidity with respect to ice $> 100\%$), allowing ice crystals to grow by vapour deposition rather than sublimate [36]. Over time, persistent contrails can lose their linear structure through wind shear and turbulence, spreading to broader cirrus-like layers known as contrail cirrus [36, 117]. These contrail-induced cirrus clouds can persist for several hours, modifying the local radiation balance by reflecting incoming solar radiation and trapping outgoing long-wave radiation – effects that together lead to net warming under most conditions [12, 16].

The likelihood of contrail formation depends on both aircraft-specific and meteorological factors. Engine operating conditions and the fuel composition determine the exhaust water vapour and soot particles that act as condensation nuclei [116, 36]. In the "soot-rich" regime, characteristic of conventional kerosene combustion, the emitted soot particles dominate ice nucleation, while under "soot-poor" conditions, such as those expected with SAF or hydrogen combustion, other aerosol species and ambient particles become increasingly relevant [16]. Theoretical prediction of contrail formation is commonly based on the Schmidt–Appleman Criterion (SAC), which defines the critical temperature and humidity thresholds at which the water vapour in the exhaust plume becomes saturated and condensation can begin [116], which is visually represented in Figure 2.21. The SAC provides a thermodynamic foundation for identifying regions of the atmosphere where contrails are likely to form and has been widely used in both climatological studies and operational contrail mitigation research [117, 118].

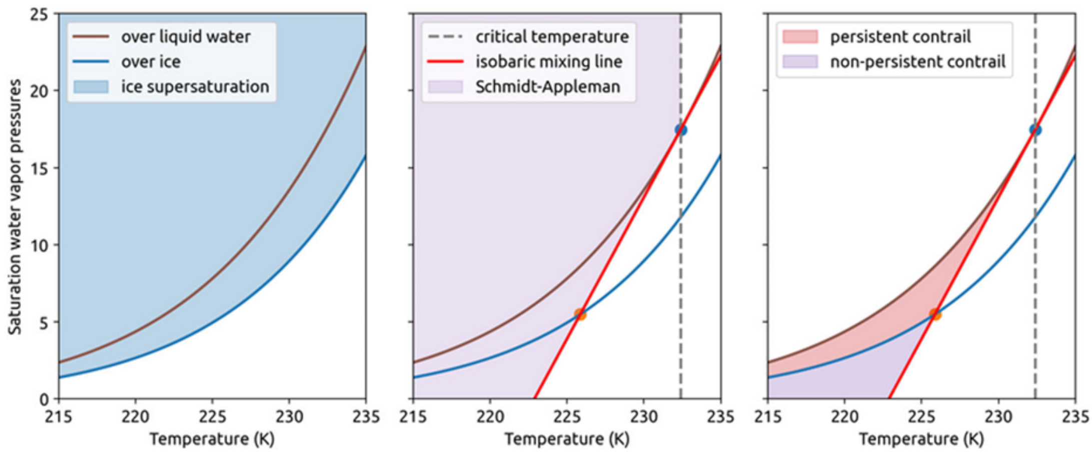

Figure 2.21: Saturation vapour pressure curves with respect to water and ice showing contrail formation areas according to the location of the exhaust plume mixing [119]

Combining the SAC with models of Ice Supersaturated Regions (ISSR) has been used to predict the formation of persistent contrails for real-world flights [34, 16]. Teoh et al. [16] used the Contrail Cirrus Prediction (CoCiP) [120] model to predict the formation and evolution of persistent contrails. CoCiP applies the SAC together with ambient ISSR to identify where persistent contrails may occur and adds further physical complexity through detailed modelling of plume thermodynamics, microphysical evolution, and the dynamic spread of contrail-induced cirrus, with nvPM emissions informing the initial ice crystal number and shaping the resulting microphysical and radiative characteristics of the contrail [16]. However, similar to NO_x modelling methods, current approaches to predicting nvPM emissions rely on empirical or semi-empirical correlations, such as the P3–T3

[34] and T4/T2 methods [34, 16], which strongly influence contrail formation predictions. Future contrail modelling techniques would benefit from physics-based nvPM prediction methods, which could be realised by coupling CRN combustion simulations with detailed soot formation models such as those implemented in SootLib, a C++ package designed for reacting-flow simulations [121]. This capability would be particularly valuable for evaluating emerging aircraft technologies and alternative fuels such as SAFs, for which existing empirical methods are not applicable or sufficiently accurate.

2.6 Climate Impact

The ultimate purpose of developing aircraft emission models is to support the reduction of adverse climatic impacts of aviation. Understanding this impact requires linking emission generation and prediction with their broader effects on the atmosphere. This section outlines the physical mechanisms through which aircraft emissions influence global warming and reviews the modelling approaches used to translate emissions into radiative forcing, effective radiative forcing, and temperature response metrics, which together quantify the total climate impact.

2.6.1 Radiative Forcing

Radiative forcing is a measure of how an emission or process alters the balance between incoming solar and outgoing infrared radiation, thus influencing the Earth's temperature [35]. Lee et al. [12] estimated that in 2005, aviation CO_2 RF accounted for 1.6% of the total anthropogenic CO_2 RF and that together the CO_2 and non-CO_2 effects arising from aviation contributed approximately 5% of the total net anthropogenic forcing globally. Carbon dioxide acts as a direct greenhouse gas with a long atmospheric lifetime and a well-mixed distribution, which means that its RF is independent of the emission location [122, 123]. In contrast, the effects of NO_x, H_2O and nvPM emissions are more complex, as they indirectly influence the climate through chemical or microphysical processes [12]. Their effects are highly dependent on the location of the emissions and the meteorological conditions, where NO_x emissions have a greater effect on the change in atmospheric concentrations of O_3 and CH_4 at higher altitudes [34], while contrail coverage increases at higher altitudes and RF effects depend on the time of day and location [124].

Carbon Dioxide

Sausen and Schumann [122] used a set of simplified linear response models to calculate the RF caused by CO_2 emissions. The evolution of CO_2 concentration over time due to aviation was calculated using a carbon cycle impulse response function $G_\chi(t)$, outlined in Equation 2.12, which assumes that CO_2 emissions are partially decayed or absorbed over time [122]. This was used as input to calculate the change in CO_2 concentration $\Delta\chi(t)$, as detailed in Equation 2.13. The decay/absorption of CO_2 was represented using five exponential decay terms, each describing a different carbon sink with various timescales, where the fraction of CO_2 following each decay path and timescales are represented by α_j and τ_j.

$$G_\chi(t) = \sum_{j=0}^{5} \alpha_j \cdot e^{-t/\tau_j} \tag{2.12}$$

$$\Delta\chi(t) = \int_{t_0}^{t} G_\chi(t - t') \cdot E(t') \cdot dt' \tag{2.13}$$

RF estimates caused by an increase in CO_2 concentration were obtained using the standard IPCC formula [35] detailed in Equation 2.14, where RF^* refers to the normalised RF, and χ_0 is the pre-industrial CO_2 concentration level. This simplified linear model was also used by Proesmans and Vos [123] to develop a climate-optimised aircraft design and again by Awde and Stuart [34] to quantify the climate response of real-world airline flights.

$$RF^*(t) = \frac{\ln(\Delta\chi(t)/\chi_0)}{\ln 2} \tag{2.14}$$

Lee et al. [12] used an Effective Radiative Forcing (ERF) metric to quantify the climate impact of aircraft emissions. ERF differs from conventional RF by including the rapid adjustments of atmospheric temperature, water vapour, and clouds that occur before the surface temperature responds. These adjustments are quantified in dedicated fixed-SST or radiative-transfer model experiments, from which the ERF/RF ratios are derived. The ERF metric for CO_2 emissions used by Lee et al. [12] was an aggregated value derived from three simple climate models: LinClim, i.e., the impulse response function based on the work of Sausen and Schumann [122], the Finite-amplitude Impulse Response (FaIR) model developed by Millar et al. [125], and the CICERO-SCM model [126, 127]. The final ERF value for CO_2 emissions was 34 mW/m^2, with an uncertainty range of 28–40 mW/m^2, which was quantified using a Monte-Carlo sampling approach [12]. The relatively narrow uncertainty range for CO_2 reflects the fact that its radiative forcing and climate response are well constrained, in contrast to short-lived non-CO_2 effects such as NO_x and contrails where the climate impact is much more uncertain [12].

Nitrogen Oxides

NO_x emissions indirectly contribute to global warming by altering atmospheric chemistry through three primary mechanisms: a short-lived increase in tropospheric O_3, producing a positive RF and atmospheric warming, followed by a reduction in the lifetime and abundance of CH_4, which subsequently induces a reduction in long-lived O_3 concentration, both of which produce a negative RF and cool the atmosphere [12]. To quantify the net impact of NO_x emissions, which is generally accepted to be a net warming effect (albeit with significant uncertainty values) [12], all three mechanisms must be considered in the RF analysis. Although chemistry-climate models have been employed to conduct comprehensive analyses of NO_x atmospheric interactions, such models are computationally intensive and cannot realistically be applied to large mission-scale studies [127]. Sausen and Schumann [122] used a highly simplified approach by scaling O_3 RF linearly with the aircraft NO_x emissions using Equation 2.15, using a scaling factor S which they described as "a very uncertain parameter". This approach contained significant limitations, as depletion in CH_4 and O_3 over time was not considered, nor the altitude dependence of NO_x emissions which disproportionately impacts O_3 and CH_4 concentrations at higher altitudes.

$$RF^{*}_{O_3} = \frac{S}{2.246} \cdot \frac{EI_{NO_x}(t)}{EI_{NO_x}(1992)} \cdot \frac{E_a(t)}{E_a(1992)} \tag{2.15}$$

Proesmans and Vos [123] used improved methods to quantify the net NO_x RF based on the methods developed by Dallara et al. [128]. The short-lived O_3 forcing was calculated as an instantaneous effect using Equation 2.16, where $s(h)$ is a forcing factor to account for the altitude dependence of the NO_x emissions, i.e., E_{NO_x}. The main improvements with the methods used for this study compared to Sausen and Schumann [122] was the implementation of simplified CH_4 and long-lived O_3 depletion models, which were calculated using a convolution integral with a fixed perturbation lifetime of 12 years, as described in Equation 2.17 where A_i represents the radiative efficiency per unit of NO_x emitted and G_i is the impulse response function [123]. These depletion models are simplified because they apply fixed perturbation lifetimes for CH_4 and O_3, thus neglecting the chemical feedbacks and variations in atmospheric composition that would alter these lifetimes over time [129]. Awde and Stuart [34] used the same RF modelling framework to predict the net NO_x RF of real-world flights, where the altitude-dependent forcing factors illustrated in Figure 2.22 were combined with actual mission profiles to generate realistic RF estimates for airline operations.

$$RF_{O3S}(t,h) = s_{O3S}(h) \cdot \left(\frac{RF_{ref}}{E_{ref}}\right)_{O3S} \cdot E_{NO_x}(t) \tag{2.16}$$

$$\begin{gathered} RF_i(t,h) = s_i(h) \int_{t_0}^{t} G_i(t-t') \cdot E_{NO_x}(t') \cdot dt' \\ \text{with} \quad G_i(t) = A_i \cdot e^{-t/\tau_i} \quad \text{for } i = CH_4,\, O_{3L} \end{gathered} \tag{2.17}$$

Similarly to their CO_2 analysis, Lee et al. [12] estimated NO_x ERF using a meta-analysis of 20 global chemistry–climate and chemical-transport models, rather than computing forcing directly. Short-term O_3 increases, CH_4 depletion, CH_4-induced long-term O_3 decreases, and CH_4-induced reductions in stratospheric water vapour were extracted from these studies and standardised into consistent RF units. The resulting component probability density functions were combined using Monte-Carlo sampling to derive a best-estimate net NO_x ERF of 17.5 mW/m^2 in 2018, with a wide uncertainty range reflecting the complex, non-linear atmospheric chemistry involved in quantifying the climate impact of NO_x emissions [12].

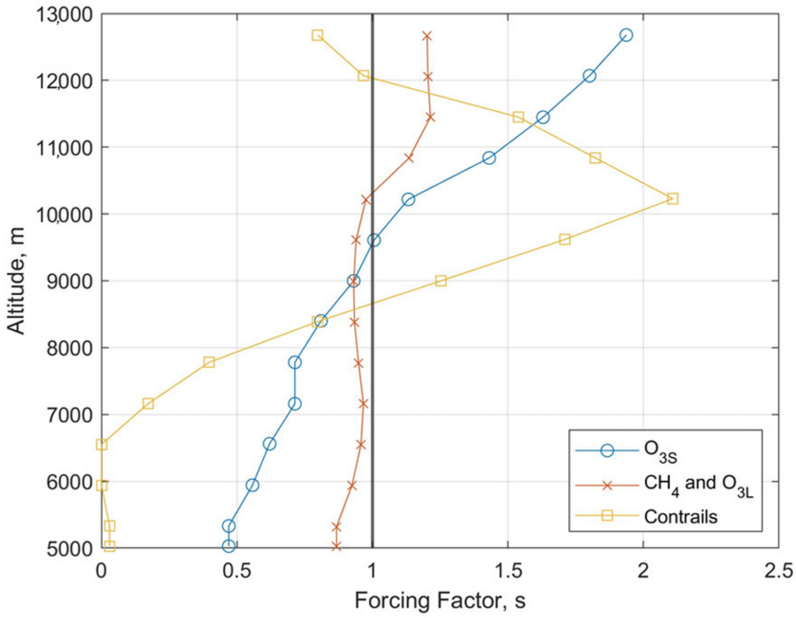

Figure 2.22: Altitude-dependent radiative forcing factors for NO_x-induced impacts and contrails, adapted from [130]

Contrails

Section 2.5.3 outlined the methods used to predict the formation of contrails and persistent contrails. When modelling the RF caused by contrails, only persistent contrails are considered, due to the short life-time and hence low impact of non-persistent contrails. Proesmans and Vos [123] and Awde and Stuart [34] used a simplified reduced-form method to calculate the RF of persistent contrails, using Equation 2.18. Within this equation, RF_{ref}/L_{ref} represents the RF per kilometre of contrail length which was obtained from the work of Dallara et al. [128], and $L(t)$ is the distance flown in ISSR conditions. Altitude dependent forcing factors were applied to the RF value as illustrated in Figure 2.22.

$$RF_{contrails}(t,h) = s_{contrails}(h) \cdot \left(\frac{RF_{ref}}{L_{ref}}\right)_{contrails} \cdot L(t) \tag{2.18}$$

Lee et al. [12] did not simulate contrails directly but instead harmonised published contrail-cirrus forcing from multiple global climate models, applying inventory-based scaling factors and an ERF/RF ratio of 0.42 to account for rapid cloud adjustments. Teoh et al. [16] used the CoCiP model to calculate the RF induced by persistent contrail formation, which does so by simulating the time-dependent microphysical evolution of each contrail segment, including ice crystal number, optical depth, and plume spreading. These properties were then used in a simplified radiative-transfer model to estimate the longwave warming and shortwave cooling produced by the contrail under different atmospheric and lighting conditions [16]. The resulting forcing was integrated over the lifetime and area of each contrail, and aggregated globally to obtain an annual mean RF value [16].

A major challenge in contrail modelling is the substantial uncertainty associated with estimated RF and ERF values. Lee et al. [12] report a central contrail-cirrus ERF of 57.4

mW/m^2, with a wide uncertainty range of 17–98 mW/m^2. Teoh et al. [16] estimated a global net contrail ERF of 32.1 mW/m^2, which is 44% lower than the central value reported by Lee et al. [12], yet still well within its uncertainty bounds. Such large uncertainty intervals limit the confidence with which contrail modelling results can be interpreted, particularly when assessing their contribution to aviation climate impacts.

2.6.2 Temperature Response

RF and ERF metrics allow us to quantify the changes in radiation caused by aircraft emissions; however, these figures are somewhat ambiguous in terms of the resulting climate impact. Therefore, it is necessary to translate the RF changes into a more meaningful and measurable metric that align with environmental objectives. Grewe and Dahlmann [131] compared the features of various climate metrics such as RF, GWP, Global Temperature change Potential (GTP), and Average Temperature Response (ATR). RF and GWP allow for comparative analyses on the same scale but ignore the resulting effect on the climate, whereas GTP enables measurement of the temperature change caused by the change in RF over a period of time but depends critically on the selected time horizon [131]. Therefore, Grewe and Dahlmann [131] argue that the ATR, which is the mean future temperature development over a specific time period, is the most appropriate metric to compare the climate impact of aircraft technologies while minimising the dependence on ambiguous variables such as the selected time horizon. In addition, using the ATR creates a clear link between aircraft emissions and climate targets, such as the Paris Agreement [15], which aims to limit global warming caused by anthropogenic emissions between 1.5 °C and 2 °C.

Surface temperature response and ATR metrics have been used in several studies to quantify the climate impact of new technologies [123] and the climate impact of real-world flights [34]. Proesmans and Vos [123] used the ATR to design a climate-optimised aircraft using a time horizon of 100 years, where they argue that 100 years provides a balanced assessment between long-lived emissions such as CO_2 and short-lived emissions such as NO_x emissions and contrail formation. To calculate the ATR, the surface temperature response ΔT was first computed for each year using the total normalised RF caused by all aircraft emissions for each respective year, as described in Equation 2.19 [123], where $G_T(t)$ is a linear temperature impulse response function that accounts for the delayed response of the climate system. The ATR for the time horizon H was simply calculated as the mean of the surface temperature response results, as presented in Equation 2.20.

$$\Delta T(t) = \int_{t_0}^{t} G_T(t-t') \cdot RF^*(t') \cdot dt' \quad \text{with} \quad G_T(t) = \frac{2.246}{36.8} \cdot e^{-t/36.8} \tag{2.19}$$

$$ATR_H = \frac{1}{H} \int_{0}^{H} \Delta T(t) \cdot dt \tag{2.20}$$

This method was also used by Awde and Stuart [34], who quantified the surface temperature response of real-world flights for CO_2, NO_x, contrails and other emissions from the year of emission to the year 2100. An example of the surface temperature response results for a single flight is presented in Figure 2.23. These results highlight the value of the surface temperature response metric, as it shows a tangible and measurable climate impact caused by individual aircraft emissions over time. For example, the short-term effects of NO_x emissions and contrails can be observed, as well as the long-term impact of CO_2 emissions, and the negligible impact of secondary emissions such as soot, H_2O and SO_4 emissions. Such models can be used to simulate the projected climate impact of future aircraft operations and to compare the climate impact of prospective aircraft designs to help aircraft manufacturers, airlines, and policy-makers make informed, data-driven decisions.

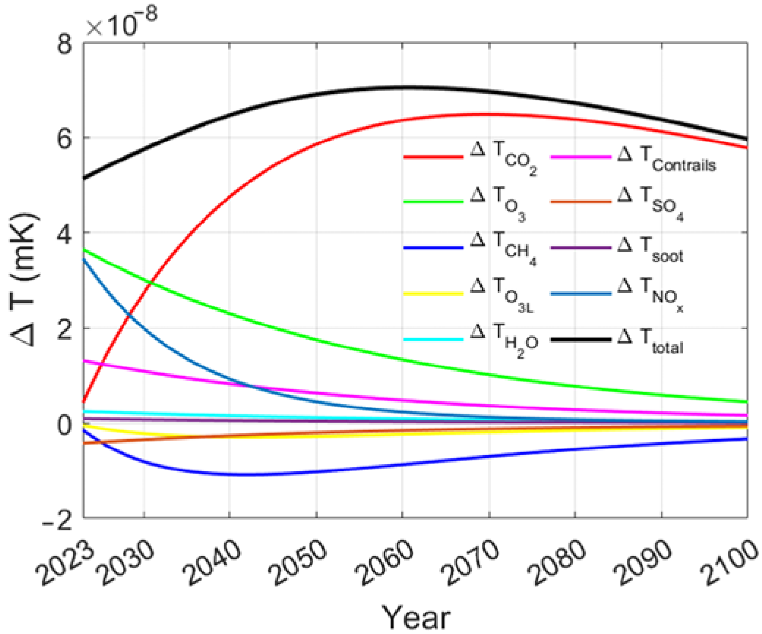

Figure 2.23: Species-specific surface temperature response for a single flight [34]

2.7 Conceptual Design

Addressing the climate impact of aviation requires progress on two coupled challenges: the decarbonisation of future aircraft and the mitigation of non-CO_2 effects. While the literature on CO_2 emissions and long-term decarbonisation options is mature, there is still limited scientific consensus on the optimum technological and operational pathways that can achieve net-zero aviation while preserving economic viability. Much existing modelling work still concentrates on performance at design range or nominal operating conditions, despite growing recognition that off-design mission behaviour strongly influences real-world performance. Therefore, there is a need for physics-based conceptual design frameworks that can be applied across diverse operational missions, enabling systematic evaluation of future aircraft technology and fuel pathways.

In contrast, understanding of non-CO_2 climate effects remains constrained by substantial scientific uncertainty. Current research is dominated by efforts to improve the accuracy and representativeness of non-CO_2 climate modelling, yet many emission predictions still rely heavily on empirical correlations based on sparse measurement datasets. These limitations prevent reliable assessment of NO_x, nvPM, and H_2O emissions, particularly for emerging combustion technologies or alternative fuels such as SAF and hydrogen, which may alter emission profiles. Advancing this field requires physics-based emission models capable of integration into large-scale mission simulations to quantify the true climate impact of present and future aircraft operations. This section therefore reviews the state of the art in conceptual aircraft design tools with mission-level simulation environments, along with propulsion and combustion modelling tools, and surrogate modelling approaches that enable high-fidelity yet computationally efficient analysis.

2.7.1 Aircraft Design Tools

Many aircraft design tools have been developed in recent years, such as the Flight Optimisation System (FLOPS) [132], Transport Aircraft System Optimisation (TASOPT) [133], Environmental Design Space (EDS) [134], and the Stanford University Aerospace Vehicle Environment (SUAVE) [135]. Table 2.6 provides details of popular conceptual design tools used throughout recent published literature.

Table 2.6: Comparison of conceptual aircraft design tools

Tool	Modelling Approach	Unconventional Systems	Flexibility & Integration	Availability
FLOPS	Empirical correlations with physics-based mission analysis for conventional aircraft.	Limited support; unconventional concepts require workarounds or external modules.	Constrained by built-in assumptions; partial external coupling possible.	Widely used but not open-source.
TASOPT	Low-order physics-based models with some empirical inputs.	Strong for BLI concepts; limited capability for electric or hydrogen aircraft.	Optimises for a specific mission; less suited to fixed geometry; requires detailed inputs.	Freely available, not open-source.
EDS	Physics-based and surrogate models; empirical methods for conventional aircraft.	Can model unconventional designs but depends on NASA toolchain; limitations unclear.	Requires multiple external NASA tools; complex for stand-alone use.	Proprietary FAA/NASA tool; not publicly accessible.
SUAVE	Multi-fidelity physics-based and semi-empirical modelling framework.	Strong support for unconventional aircraft (e.g., hybrid-electric, hydrogen, BWB).	Highly modular; interfaces with SU2, OpenVSP, OpenMDAO, surrogate models.	Open-source and actively developed.

SUAVE was selected as the aircraft design tool for this project due to its accessibility, open-source framework to allow for customised models, and its multi-fidelity approach, which contains a suite of ready-made physics-based models that have been used in the design and evaluation of prospective aircraft designs in several studies [65, 78, 54]. SUAVE is capable of complete aircraft design and optimisation, and contains methods for aerodynamics, propulsion, and mission-level simulations. Examples of physics-based models within SUAVE include the 'fidelity-zero' Vortex Lattice Method (VLM) and Blade Element Momentum Theory (BEMT) aerodynamic models, which were validated against experimental wind tunnel and CFD data [136]. VLM is a low-fidelity aerodynamic calculation method, which discretises the wing into panels and uses the Biot-Savart law to calculate the inviscid lift and induced drag of the aircraft [137], where the 'fidelity-zero' VLM model within SUAVE is based on a modified version of the NASA VORLAX code [138]. Aircraft drag calculations are performed using semi-empirical methods, such as that used for the fuselage parasite drag as shown in Equation 2.21, where k_{fuse} is the form factor, C_f is the friction coefficient derived from a compressible turbulent flat plate computation, and S_{ref} is the fuselage reference area. The form factor is computed using Equation 2.22, where C is the correction factor to be calibrated, and δu_{max} represents the maximum velocity increase on an ellipsoid of revolution [135]. While it is generally desirable to use physics-based models, such semi-empirical methods provide an opportunity for model calibration if sufficient real-world data is available.

$$C_{D_{fuselage}} = k_{fuselage} \cdot C_f \cdot S_{ref} \tag{2.21}$$

$$k_{fuselage} = (1 + C \cdot \delta u_{max}) \tag{2.22}$$

The propulsion model within SUAVE is a simplified 1D analysis based on the Cantwell method [139], which approximates performance using a single operating point efficiency based on the design point. Hence, the native SUAVE propulsion model does not account for off-design efficiency, and thus the TSFC is a function of only the altitude and Mach number, which is the main limitation of the SUAVE tool. However, a key advantage of the SUAVE tool is its multi-fidelity approach and ability to connect external models through propulsor surrogates. It is therefore possible to generate propulsion data from external, higher-fidelity models which can be used to develop surrogate models within SUAVE. SUAVE models aircraft missions using a segment-based framework in which each segment applies dedicated aerodynamic, propulsion, and atmospheric analyses. The equations of motion are solved using a pseudospectral collocation method, which discretises each segment into a small number of optimally spaced control points and uses pre-computed matrices to calculate derivatives efficiently [135]. A nonlinear root-finding algorithm adjusts unknowns such as pitch angle and throttle to drive the force and kinematic residuals to zero within each segment. This approach supports multi-fidelity models and arbitrary mission profiles, suitable for analysing both conventional and advanced aircraft concepts for a variety of aircraft missions.

2.7.2 Propulsion System Modelling

Table 2.7 outlines the popular propulsion system design tools widely used throughout the published literature. These software include NASA's Numerical Propulsion System Simulation (NPSS) [140], Gas Turbine Simulation Programme (GSP) [141], PyCycle [142], GT-SUITE [143], and Propulsion Object Oriented Simulation Software (PROOSIS) [144].

Table 2.7: Comparison of aircraft propulsion system modelling software

Tool	Modelling Approach	Unconventional Systems	Flexibility & Integration	Availability
NPSS	Component-based 0D/1D thermodynamic simulation for steady and transient analysis.	Strong support for hybrid-electric, bleed-less, recuperated, and novel cycles.	Highly modular; integrates with CRN, surrogate models, and NASA toolchain.	Licensed; widely used in industry and research.
GSP	0-D thermodynamic modelling with map-based components.	Moderate capability; supports custom components but limited for radical architectures.	GUI + scripting; less modular than NPSS but easy for preliminary design.	Commercial licence; broadly accessible.
PyCycle	Open-source thermodynamic cycle solver built on OpenMDAO.	Strong support for new cycles, hybrid-electric systems, and custom physics.	Deep integration with MDAO workflows and surrogate modelling.	Open-source; actively developed.
GT-SUITE	High-fidelity 1-D engine/system simulation for steady and transient analysis.	Good for hybridisation and detailed component studies; limited full-architecture flexibility.	Integrates with CFD/FEM; extensive libraries but heavier setup.	Commercial; widely used in industry.
PROOSIS	Modelica-based multi-domain propulsion and system simulation.	Strong support for hybrid-electric and distributed propulsion.	Highly modular; integrates with system engineering and multi-domain analysis.	Commercial; used in industry and academia.

NPSS was chosen for the current project due to its accessibility, high computational efficiency, and wide use throughout the published literature [50, 145]. NPSS is an object-oriented modelling environment developed by NASA and industry partners [140]. It was originally designed for gas turbine analysis, and contains a suite of gas turbine assembly component models, such as compressors, combustors, turbines, and nozzles installed within the software package, where each component satisfies the conservation equations for mass and energy [145]. The NPSS software contains internal non-linear solver routines that aim to locate operating points that satisfy the coupled differential equations that represent the system within the defined model, through iteratively adjusting independent variables until convergence is achieved for the target dependent variables [50]. For example, turbine pressure ratios are adjusted such that the work produced by the turbines is equal to the work demanded by the compressors. Furthermore, NPSS was developed using C++ [140], ensuring that simulations are completed with high computational efficiency.

Inclusion of component performance maps within NPSS enables off-design performance analysis of aircraft propulsion systems [146], which improves the fidelity of propulsion analysis relative to lower-fidelity methods such as those used within SUAVE. NPSS has been used to simulate conventional [50, 145, 147] and advanced gas turbine propulsion systems, such as open-rotor engines and UHBPR turbofans [50, 148]. In addition, electronic components have been added to the NPSS software, enabling the development of electric and hybrid-electric propulsion system models [149]. The potential for off-design analysis and the development of next-generation propulsion models make NPSS a preferable alternative to SUAVE for modelling both conventional and novel propulsion systems.

2.7.3 Combustion Modelling

Table 2.8 summarises the combustion and chemical-kinetics modelling tools commonly employed in gas-turbine and emissions research. These include Cantera [150], CHEMKIN-Pro [151], OpenSMOKE++ [152], COSILAB [153], and the combustion modelling capabilities available within ANSYS Fluent [154].

Cantera was selected as the chemistry solver for this work due to its strong suitability for modelling non-CO_2 emissions, including NO_x formation and nvPM precursors (i.e., UHC emissions) [108, 109]. Its open-source, multi-physics framework provides detailed chemical kinetics, thermodynamic property evaluation, and transport modelling within a single, fully scriptable environment. This is essential for CRN models, which require efficient evaluation of large reaction mechanisms between interconnected reactor elements. In contrast to commercial tools such as CHEMKIN or COSILAB, Cantera offers unrestricted access of the solver and mechanism files, allowing transparent modification of reaction pathways for future fuels such as SAF [109], as well as modification of the fuel sulphur content, which could have an impact on predictions of contrail formation [155, 36]. Its strong community support, established validation across combustion research [108, 109], and compatibility with advanced kinetic mechanisms (e.g., the compact kerosene mechanism developed by Luche [156]) make it a robust and extensible platform for high-fidelity, physics-based emission predictions in mission-scale studies, particularly when combined with surrogate modelling techniques to improve computational efficiency.

2.7.4 Surrogate Modelling

Surrogate modelling is an essential component of modern aerospace design, enabling physics-based models to be deployed at scales that would otherwise be computationally prohibitive. Several regression approaches are widely used in the literature, including polynomial response surfaces, radial basis functions, support vector machines, Kriging or Gaussian process regression, and machine learning methods such as Artificial Neural Networks (ANN) [157]. Among these, Gaussian regression models offer strong predictive performance and built-in uncertainty quantification, making them particularly attractive for early-stage design studies [158]. However, a key limitation is that their computational cost scales cubically with the number of training samples [159], making them impractical for large datasets

Table 2.8: Comparison of combustion modelling tools for gas turbine emissions

Tool	Modelling Approach	Unconventional Systems	Flexibility & Integration	Availability
Cantera	Open-source library for kinetics, thermodynamics, transport, and reactor networks (0D, 1D).	Strong support for alternative fuels, NO_x pathways, and custom mechanisms.	Python, C++, MATLAB integration; highly modular for CRN and emissions modelling.	Open-source; widely used in research.
CHEMKIN	Industry-standard solver for detailed kinetics, flames, ignition, and emissions.	Excellent for NO_x, soot, and fuel chemistry with extensive validation.	GUI workflows; integrates with CFD (e.g., ANSYS Fluent).	Commercial; widely used.
OpenSMOKE++	Open-source kinetic solver for detailed mechanisms, laminar flames, and reactors.	Strong support for alternative fuels and pollutant formation modelling.	C++ core with Python interface; suited for batch and UQ studies.	Open-source; active academic development.
COSILAB	High-fidelity solver for flames, ignition, extinction, and detailed chemistry.	Excellent pollutant and soot modelling capabilities.	GUI-based; integrates with external CFD but less flexible than Cantera.	Commercial; used in combustion R&D.
ANSYS Fluent	CFD platform with reduced/global kinetics and advanced turbulence–chemistry models.	Good for 3D combustor modelling; limited detailed kinetics unless externally coupled.	Strong 3D integration; not suited for stand-alone kinetics or CRN.	Commercial; widely adopted.

typically required for high-fidelity engine and emissions modelling. In contrast, ANNs scale efficiently with the volume of data and are well suited to capture the nonlinear relationships inherent in combustion chemistry and engine performance [160]. Their rapid evaluation speed and ability to generalise across wide operating envelopes make them a strong candidate for surrogate development in this thesis. For example, ANN evaluation times are on the order of milliseconds per prediction [161], compared to approximately 10 seconds per physics-based CRN combustion simulation, highlighting the substantial computational gains achievable. This increase in efficiency is necessary to enable rapid evaluations of full flight schedules and to support large-scale mission studies.

The performance of ANN models are highly dependent on the hyperparameters which define the model architecture and training methods used, which are generally unintuitive. These parameters include the number of hidden layers, neurons per layer, learning rate, activation functions, training epochs, and data normalisation strategies. Bayesian optimisation has become a widely adopted approach for tuning ANN hyperparameters in engineering surrogate applications, owing to its ability to efficiently explore high-dimensional and non-convex search spaces [162]. Bayesian optimisation provides a probabilistic framework for sequentially selecting hyperparameter configurations, balancing exploration of the search space with exploitation of promising regions.

This approach has been successfully applied in several studies, including the work of Ren et al. [162], who demonstrated its effectiveness in improving surrogate model accuracy while reducing the number of required model evaluations, during the development of an ANN regression surrogate for a high-dimensional physics-based model. A key consideration in ANN development is the choice of training-validation strategy. While k-fold cross-validation can improve robustness, it also increases computational cost of training, particularly when the Bayesian optimisation method requires evaluating several architectures. Austern and Zhou [163] highlight that, in cases where abundant data is available, hold-out validation can provide performance estimates comparable to cross-validation at significantly lower computational expense. In most applications, the optimisation objective is defined using metrics such as Mean Absolute Error (MAE) or Root-Mean-Squared Error (RMSE) on a validation set, with the final selected model assessed on an independent test dataset to ensure generalisation across different datasets [162].

2.8 Research Questions

A critical examination of the literature has identified several unresolved limitations in current research regarding aircraft decarbonisation and non-CO_2 effects. Within non-CO_2 research, a strong reliance on empirical and semi-empirical emission models remains prevalent. Such models are typically derived from limited experimental datasets and calibrated to conventional engines and fuels. As a result, their applicability is limited to legacy aircraft configurations and makes them unsuitable for future climate impact assessments, where physically representative predictions of non-CO_2 emissions are required. Moreover, even when applied to historical aircraft, significant uncertainty exists due to the limited interpolation data available to calibrate the empirical models.

Evaluations of decarbonisation pathways, particularly those comparing alternative fuels and propulsion concepts, are typically centred on the performance of design range missions or a limited number of idealised flight profiles. These assumptions can misrepresent the true performance of prospective aircraft technologies, as commercial aircraft are rarely operated under design-point conditions. Comprehensive comparative analyses therefore require consideration of the variability inherent in real-world operations, including differences in mission length, flight profiles, payload, and atmospheric conditions. In contrast, mission-level non-CO_2 emissions studies employing advanced physics-based models remain absent from the literature. This is primarily due to the lack of modelling frameworks capable of resolving non-CO_2 emissions with sufficient fidelity while remaining computationally efficient enough for large-scale operational analyses.

On the basis of these findings, four research questions are formulated to guide the remainder of this thesis. These questions are designed to address the identified methodological gaps and to advance modelling capabilities for the evaluation of aircraft decarbonisation strategies and associated climate impacts under real-world operational conditions.

1. *How can physics-based aircraft, propulsion, and combustion models be integrated with real-world flight data to accurately predict aircraft performance and emissions across complete flight schedules?*

2. *To what extent do aircraft technology level, hydrogen tank gravimetric index, and engine cycle enhancements influence the performance of hydrogen-powered aircraft relative to SAF-powered counterparts?*

3. *How does the use of physics-based non-CO_2 emissions models at the mission level affect the estimated climate impact of aircraft operations when compared with empirical approaches?*

4. *To what extent can fleet renewal strategies reduce the overall climate impact of commercial aircraft operations, when accounting for both CO_2 and non-CO_2 effects under realistic operational conditions?*

Chapter 3

Methodology

The literature review in Chapter 2 identified the need for a flight simulation framework that offers both sufficient accuracy and computational efficiency to assess real-world aircraft operations, evaluate decarbonisation pathways, and quantify non-CO_2 emission impacts. This chapter outlines the methodology used to develop and validate the baseline modelling framework using design tools selected through the comparative assessment presented in Section 2.7, along with the development of a real-world operations model. The resulting baseline modelling framework forms the foundation for the operational case studies presented in Chapters 4 and 5.

3.1 Baseline Flight Simulation Framework

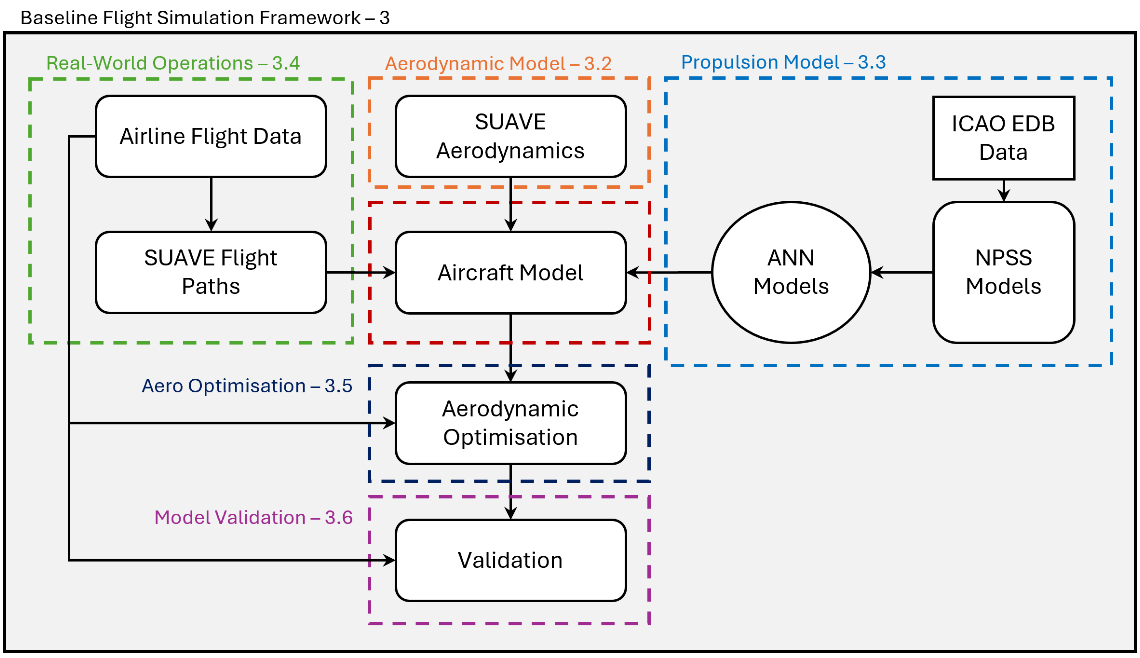

Figure 3.1: Schematic diagram of baseline flight simulation framework

Figure 3.1 outlines the model connections that form the baseline flight simulation framework. The SUAVE aircraft simulation environment was used to define the airframe models of Boeing 737-800NG (B737-NG) and Boeing 737-8200 (B737-MAX) aircraft and perform aerodynamic analysis, which is detailed in Section 3.2. Turbofan models of the CFM56-7B26 and LEAP-1B27 engines were developed within NPSS, and connected to the SUAVE aircraft model via ANN propulsor surrogates, as described in Section 3.3. Section 3.4 outlines the airline flight database provided for this project and the incorporation of realistic operational profiles into the SUAVE simulation environment, providing the basis for representative mission simulations and model validation. Sections 3.5 and 3.6 outline the optimisation and validation of the aircraft model across a diverse set of flights to demonstrate its accuracy over a broad range of operating conditions.

3.2 Aerodynamics

3.2.1 Airframe Model

Representative airframe models of the B737-NG and B737-MAX aircraft were required to perform the aerodynamic analysis. Due to the relatively low fidelity of the aerodynamic models used, exact representations were not required, but key parameters such as wingspan, chord geometry, fuselage length and diameter, and surface areas were used. Details of these key airframe parameters were obtained from Boeing 3-view CAD drawings developed for airport planning purposes [164] and the Brady Boeing 737 Technical Guide [165]. It is important to note that, while the B737-NG and B737-MAX share an almost identical airframe, the B737-MAX was designed with a number of minor aerodynamic improvements, such as the addition of the improved split-scimitar winglet design and the removal of the aft body vortex generators [165] — features that the low-fidelity aerodynamic model cannot capture. The B737-NG airframe model generated within SUAVE is presented in Figure 3.2.

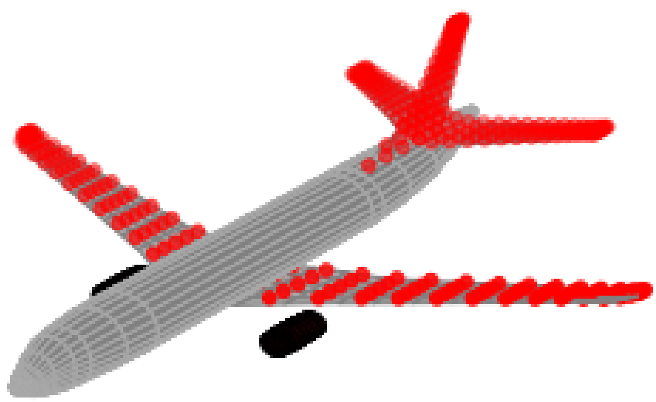

Figure 3.2: SUAVE airframe model of B737-NG, with discretised panels and red control points used for VLM calculations

3.2.2 Vortex-Lattice Method

The SUAVE Fidelity-Zero aerodynamics model computes subsonic lift using VLM, which calculates the inviscid lift (i.e., not accounting for viscous effects) of the wing based on a discretised lifting-surface representation. When a configuration is assigned this model, SUAVE samples a small set of angles of attack, solving the VLM for each condition, and fits a surrogate polynomial representation of C_L with respect to the angle of attack. This surrogate is then evaluated throughout the mission analysis, enabling rapid evaluation of aerodynamic forces without repeatedly solving the full VLM. The inviscid lift computation is supplemented with empirical correction factors to account for the contributions of the fuselage, compressibility, and viscous effects [135]. The fuselage lift contribution is described in Equation 3.1, where $C_{\text{fuselage, L}}$ is the fuselage lift correction factor, and L_{VLM} is the inviscid lift calculated using the Fidelity-Zero VLM. Induced drag is computed using the VLM model combined with viscous corrections derived from historical aircraft data. This integrated approach allows the Fidelity-Zero model to remain computationally inexpensive while still capturing the dominant aerodynamic trends needed for conceptual design studies. Although this model is simplified relative to higher-fidelity CFD-based methods, the Fidelity-Zero VLM has been verified within validation studies [136].

$$L = C_{\text{fuselage, L}} \cdot L_{VLM} \tag{3.1}$$

3.2.3 Drag Prediction

The drag prediction framework within the Fidelity-Zero aerodynamics model relies primarily on semi-empirical correlations based on the work of Shevell [166], allowing rapid estimates of drag suitable for conceptual-level analysis. Rather than resolving viscous or compressibility effects through high-fidelity CFD, SUAVE constructs a total drag build-up from a series of component-wise correlations. Parasite drag for both the wing and fuselage is evaluated using flat-plate skin-friction estimates informed by form-factor relations that account for thickness, sweep, curvature, and compressibility effects. The fuselage parasite drag calculation was previously described in Equations 2.21 and 2.22, highlighting use of the empirical correction factor $C_{\text{fuselage, D}}$. Similarly, the parasite wing drag calculation is presented in Equation 3.2, where k_{wing} is the wing form factor. The form factor is calculated using Equation 3.3, where t/c is the wing thickness-to-chord ratio, Λ is the wing sweep, M is the Mach number, and C_{wing} is an empirical correction factor.

$$C_{D_{p,\text{wing}}} = k_{\text{wing}} \cdot C_f \cdot S_{\text{ref}} \tag{3.2}$$

$$k_{\text{wing}} = 1 + \frac{2C_{\text{wing}}\left(\frac{t}{c}\cos^2\Lambda\right)}{\sqrt{1 - M^2\cos^2\Lambda}} + \frac{C_{\text{wing}}}{2\cos^2\Lambda}\left(\frac{t}{c}\right)^2 \frac{1 + 5\cos^2\Lambda}{2\left(1 - M^2\cos^2\Lambda\right)} \tag{3.3}$$

Beyond parasite drag, SUAVE includes a viscous lift-dependent drag term that supplements the inviscid induced drag predicted by the VLM, incorporating the impact of boundary-layer growth and span-efficiency degradation [166]. The induced drag calculation is presented in Equation 3.4, where $C_{D_{i,\text{ inviscid}}}$ and $C_{D_{i,\text{ viscous}}}$ represent the inviscid and viscous elements of the induced drag, respectively, and C_{viscous} is the lift-dependent viscous drag correction factor applied in the Fidelity-Zero model. Finally, the trim drag is applied as a multiplier of the total aircraft drag coefficient, as described in Equation 3.5, where C_{trim} is the trim drag correction factor.

$$C_{D_i} = C_{D_{i,\text{ inviscid}}} + C_{D_{i,\text{ viscous}}} = C_{D_{i,\text{ inviscid}}} + \left(C_{\text{viscous}} \cdot C_{D_{p,\text{wing}}} \cdot C_L^2 \cdot S_{\text{ref}}\right) \tag{3.4}$$

$$C_{D_{\text{total}}} = C_{\text{trim}} \cdot C_D \tag{3.5}$$

3.3 Propulsion

3.3.1 Turbofan Model

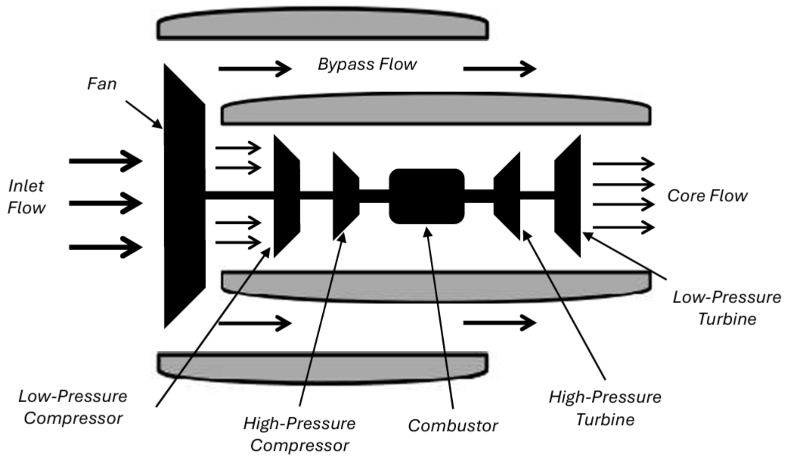

Figure 3.3: Generalised NPSS propulsion system model for CFM56-7B26 and LEAP-1B27 turbofan engines

A one-dimensional numerical propulsion system model for the CFM56-7B26 and LEAP-1B27 turbofan engines was developed in NPSS. A generic dual-spool turbofan architecture was constructed using the components shown in Figure 3.3. Off-design performance was predicted using compressor and turbine maps representative of direct-drive turbofans, obtained from the work of Hendricks and Gray [142], while inlet and nozzle performance at off-design conditions followed the scheduling approaches of Schutte [147].

Bleed flows were incorporated to account for turbine cooling, with air extracted from the mid- and final-stage compressor bleeds and routed to the HPT and LPT, where both chargeable and non-chargeable bleed flows were included. Turbine cooling requirements were estimated using NASA's CoolIt subroutine [167], with the cooling fraction computed at the Rolling Take-Off (RTO) condition and applied across all operating points, consistent with practices adopted in similar NPSS-based studies [50, 142]. Additional bleed schedules – accounting for customer bleed (used for pneumatics, air conditioning, anti-icing, etc.), surge control, and turbine active clearance control systems – were implemented based on information in the CFM training manual [168]. These schedules were necessary to achieve realistic FAR values and ensure stable engine behaviour at low-power settings.

3.3.2 Calibration & Validation

A calibration procedure was required to generate configuration-specific NPSS models of the CFM56-7B26 and LEAP-1B27 turbofan engines using the generic component architecture shown in Figure 3.3. The objective of the calibration was to produce numerical engine models that accurately reproduce performance at key operating conditions, including SLS, RTO, and Top-of-Climb (TOC).

Two calibration strategies are commonly used in NPSS-based studies. The Multi-Design Point (MDP) method developed by Schutte [147] treats each operating condition as an independent design point and solves for all simultaneously, enabling close matching throughout the operating envelope. However, the MDP approach is considerably more complex, requires accurate initial estimates for multiple design-point variables, and is often prone to convergence difficulties [147]. In contrast, the Single-Design Point (SDP) approach selects one operating point as the primary design condition (typically TOC [50]) and calibrates the model at this point while monitoring performance at other off-design conditions. For the present work, the SDP approach was adopted because the additional complexity and tuning effort associated with an MDP formulation was not justified for two well-characterised engine configurations, for which reasonable design-variable estimates were available.

The SDP method was implemented using TOC as the primary design condition. Key design variables – including FPR, OPR, BPR, and T4 – were systematically varied to achieve an appropriate balance between thrust, TSFC, and secondary performance indicators such as compressor and turbine map operating points and combustor FAR, ensuring physically realistic thermodynamic behaviour. SLS thrust and TSFC targets were taken from the ICAO EDB, which provides experimental measurements for four SLS power settings ranging from 100% to 7% rated thrust. The TOC thrust target for the CFM56-7B26 was obtained from the turbofan model of Jones et al. [50], and the same TOC thrust value was adopted for the LEAP-1B27 model, consistent with its use in their UHBPR engine design within the same study. The target thrust for the RTO condition was calculated using the "Boeing Equivalent Thrust" formulation presented in Equation 3.6 [169].

$$T_{\mathrm{RTO}} = \frac{T_{\mathrm{SLS}}}{1.2553} \tag{3.6}$$

Model accuracy was assessed by comparing the NPSS-predicted TSFC values against experimental measurements for the four SLS operating points reported in the ICAO EDB. The predicted and measured TSFC values for the CFM56-7B26 and LEAP-1B27 engines are summarised in Table 3.1. Excellent agreement was achieved at the 100% and 85% power settings, with relative errors between 0.1–0.7%. At lower power settings, TSFC errors increased to 3.0–9.6%; however, these operating points correspond to substantially lower thrust levels and therefore contribute minimally to the total mission fuel burn. In addition, the aircraft operates at these conditions for only a small fraction of the mission profile, further reducing the impact of low-power TSFC discrepancies on overall performance prediction. The TSFC accuracy was therefore considered acceptable, with the model demonstrating realistic thermodynamic behaviour across all operating conditions, which was essential for the combustion modelling work presented in Chapter 5.

Table 3.1: Comparison of predicted and ICAO TSFC values for the CFM56-7B26 and LEAP-1B27 engines at SLS operating points.

	CFM56-7B26			**LEAP-1B27**		
Op. Point	**Thrust** (lbf)	**Pred. TSFC** (lbf/hr·lbm)	**ICAO TSFC** (lbf/hr·lbm)	**Thrust** (lbf)	**Pred. TSFC** (lbf/hr·lbm)	**ICAO TSFC** (lbf/hr·lbm)
SLS – 100%	26300	0.364	0.366	28000	0.286	0.287
SLS – 85%	22355	0.350	0.350	23800	0.276	0.275
SLS – 30%	7890	0.323	0.333	8400	0.250	0.258
SLS – 7%	1841	0.510	0.466	1960	0.406	0.385

3.3.3 Surrogate Models

The complexity of physics-based models often results in greater computational expense compared to empirical-based models. One goal of this project is to develop physics-based models capable of accurately and rapidly simulating real-world aircraft operations. Therefore, reduced-order methods are required to reduce simulation times while maintaining sufficient accuracy. Section 2.7.4 identified ANNs as an excellent candidate for the development of such surrogate models due to the accuracy and speed of the evaluations, particularly when used with large datasets compared to alternative surrogate modelling methods [157].

The calibrated NPSS model described in Section 3.3.2 was used to produce an engine deck of approximately 100,000 operating points, covering all combinations of altitude, Mach number, throttle and ambient temperatures contained within the flight database described in Section 3.4.1. The thrust and TSFC predictions within this dataset were used to develop the ANN surrogates for the CFM56-7B26 and LEAP-1B27 propulsion systems.

Bayesian optimisation was used to determine the optimal hyperparameters for each surrogate model following an approach similar to that of Ren et al. [162]. The optimisation space included the number of hidden layers, the number of neurons per layer, the learning rate, the activation function, the data-scaling method, and the number of training epochs. The dataset was divided into training, validation, and testing subsets using a 60/20/20 split. Cross-validation was not applied in order to reduce computational cost, which was substantial given the number of optimisation runs required. Its omission was justified by the size of the available dataset, which allowed sufficiently large training, validation, and test partitions to achieve performance estimates comparable to those obtained by cross-validation [163].

The optimisation objective was to minimise the MAE of the validation set, and the resulting optimal models were further validated by evaluation of the MAE and RMSE of

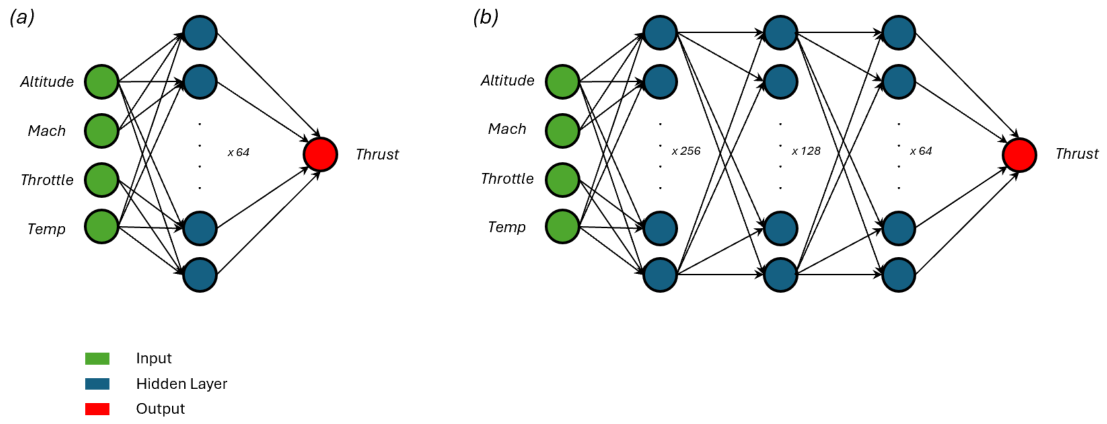

Figure 3.4: Illustration of change in ANN architecture for CFM56-7B26 thrust surrogate optimisation (a) Baseline ANN architecture (b) Optimised ANN architecture

the unseen test dataset. Figure 3.4 presents an example of an optimised ANN architecture for the CFM56-7B26 thrust model, demonstrating that the Bayesian optimiser tended to select deeper networks with a larger number of hidden-layer neurons. The final test-set MAE, RMSE, and MAPE values for the thrust and TSFC ANN surrogates are summarised in Table 3.2.

Table 3.2: Surrogate model error metrics for thrust and TSFC predictions of the CFM56-7B26 and LEAP-1B27 propulsion systems.

Prop. System	**CFM56-7B26**			**LEAP-1B27**		
	MAE	**RMSE**	**MAPE**	**MAE**	**RMSE**	**MAPE**
Thrust	1.22×10^2	2.59×10^2	1.204%	1.00×10^2	2.40×10^2	0.958%
TSFC	1.07×10^{-7}	2.10×10^{-7}	0.426%	1.01×10^{-7}	1.97×10^{-7}	0.439%

3.4 Real-World Operations

3.4.1 Flight Database

An extensive flight database was provided by Ryanair to conduct the studies within this project, consisting of Quick Access Recorder (QAR) data for a full day of B737-NG operations (2408 flights), alongside a further 24 B737-MAX flights, where data was sampled at a rate of 1 Hz and between 0.08–0.33 Hz, respectively. Ryanair are Europe's leading airline in terms of flights and passengers carried, operating almost 3000 flights daily with a fleet of 600 B737 aircraft at the time of writing [170]. The flight database provided a valuable opportunity to conduct a rigorous validation and calibration study to evaluate and maximise the accuracy of the aircraft model, alongside detailed operational case-studies. The distribution of mission range and Take-Off Weights (TOW) within the flight database is illustrated in Figure 3.5, where the TOW axis-values were redacted due to the sensitive nature of the data, but the variation of TOW values is indicated on the graph. There was significant variation in the mission range, ranging from 88 NM to 2320 NM, with an average mission range of 693 NM. This was closely aligned with the airline's annual average mission range of 766 NM in 2023 [171].

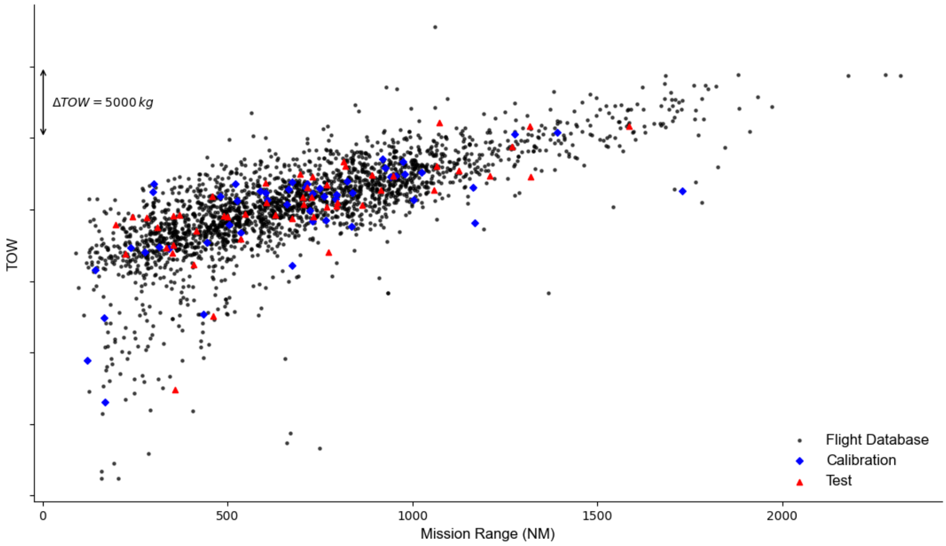

Figure 3.5: Distribution of mission range and TOW for the total B737-NG flight database and calibration/test datasets

To perform the validation and calibration of the B737-NG aircraft model, a subset of 50 flights were selected from the flight database and placed into the calibration dataset using a random sampling method. In order to maintain sufficient representation of the wider database, the calibration dataset was generated such that the mean of the mission range and TOW were kept within 1% of the complete flight database, while the sample standard deviations were maintained within 10% of the complete flight database, which was achieved through generation of thousands of random samples. The 50 selected flights are illustrated in Figure 3.5, superimposed on the total flight database. Using the same approach, a further 50 flights were placed in the B737-NG test dataset. Due to the limited available B737-MAX data, 20 flights were generated for the calibration dataset using the same random sampling method, leaving four remaining flights that were used for the test dataset.

3.4.2 Flight Paths

The SUAVE mission analysis module works with discretised linear flight segments to reduce the computational expense of simulations. Therefore, it was necessary to process the QAR data for each flight to produce segmented trajectories compatible with the SUAVE aircraft model.

A Python-based workflow was developed to automate this process. The algorithm identified climb, cruise, step-climb/step-descent, and descent segments, as well as portions of the flight where high-lift devices or landing gear were deployed. The climb, cruise, and descent phases were detected using a rolling-mean estimate of the flight-path angle, supplemented with additional logic to correct misidentified segments caused by noise in the QAR data, and to identify any step-climb/descent segments within the cruise phase. Flap, slat, and landing-gear deployments were identified directly from the relevant QAR parameters.

After segment classification, each phase was further discretised into sub-segments to ensure accurate representation of aircraft velocity, acceleration, vertical rate, and ambient temperature throughout the mission. Figure 3.6 illustrates a representative discretised SUAVE mission profile for a B737-NG flight from the database in Figure 3.5, showing how altitude and Mach number profiles are approximated relative to the raw QAR data.

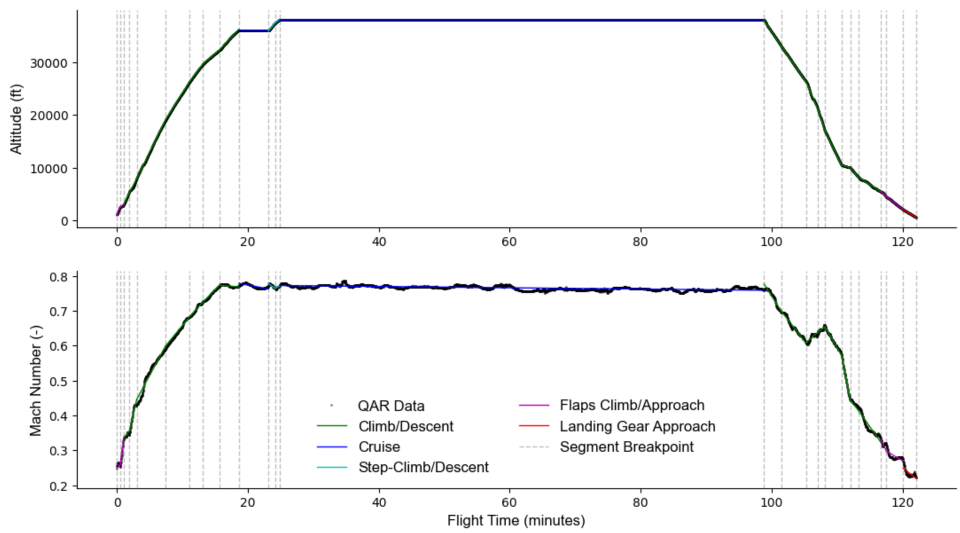

Figure 3.6: Optimised representation of a B737-NG flight path in terms of altitude and Mach number compared to QAR data

Excellent representation of the flight path variables was achieved using an algorithm to select optimal sub-segment breakpoint locations throughout the mission profile. For the climb and descent segments, eight sub-segment breakpoints were used, where the locations were determined using a multi-start gradient-based optimisation to maximise the R^2 correlation coefficient for the altitude approximation. Cruise, step-climb/step-descent, and segments involving high-lift or landing gear configurations were treated similarly, with the number of sub-segments scaled according to segment duration. The optimised altitude breakpoints were subsequently used as the basis for approximating the Mach number, ground speed, and ambient temperature throughout the mission. The initial and terminal values for each sub-segment were used within the linear segment definitions within SUAVE, which were solved using the methods described in Section 2.7.1.

3.5 Aerodynamic Optimisation

3.5.1 Optimisation Strategy

Section 3.2.3 introduced the semi-empirical correction factors used within the SUAVE drag build-up method. The availability of an extensive QAR flight dataset enabled these aerodynamic coefficients to be optimised to maximise fuel-flow accuracy relative to measured airline operations. The optimisation variables comprised the empirical coefficients $C_{\text{fuselage, L}}$, $C_{\text{fuselage, D}}$, C_{wing}, C_{viscous}, and C_{trim}, which are used in Equations 3.1, 2.22, 3.3, 3.4, and 3.5, respectively. The B737-NG calibration dataset, described in Section 3.4.1, was used for this purpose due to its significantly larger number of flights compared to the B737-MAX dataset. The optimisation objective was defined as the average fuel-flow error across all climb and cruise segments, since these phases are modelled with higher precision than descent, where low-power engine inaccuracies outlined in Table 3.1 introduced higher relative errors. The average fuel-flow error metric was favoured instead of the cumulative fuel burn error to encourage generalisation of the model across all mission ranges.

A sensitivity analysis was performed to quantify the influence of each coefficient on the average fuel-flow error by perturbing each parameter by 1%. Figure 3.7 illustrates the resulting change in climb, cruise, and combined fuel-flow error magnitudes across the 50 calibration flights. The analysis showed that the fuselage lift ($C_{\text{fuselage, L}}$) and trim-drag (C_{trim}) correction factors exerted the strongest influence on fuel-flow predictions, followed by the wing drag coefficient, where the impact was greatest on the cruise fuel-flow error magnitude. In contrast, the fuselage and viscous lift-dependent drag coefficients had minimal impact, though their influence was slightly greater in cruise than in climb.

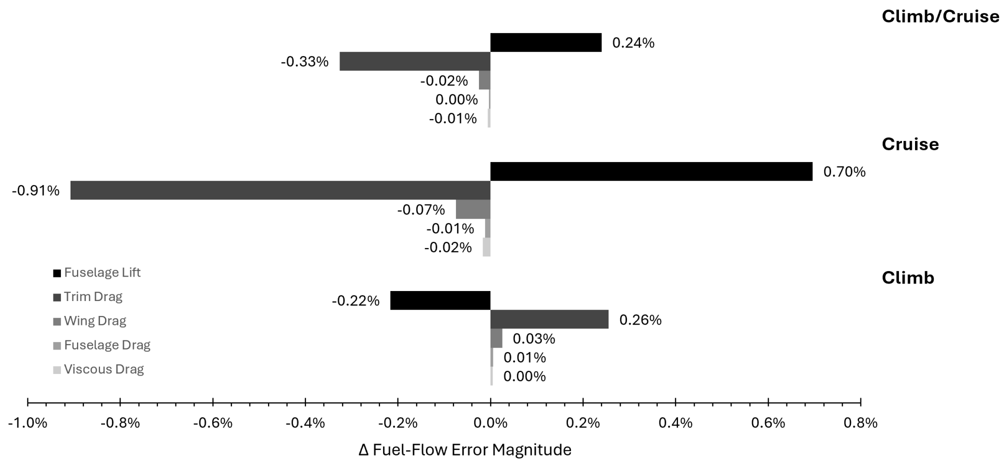

Figure 3.7: Sensitivity analysis of aerodynamic coefficients on the average fuel-flow prediction errors within the calibration dataset

Following optimisation of the baseline SUAVE drag model, additional configuration-specific adjustments were applied to modify the drag polars for the 'Flaps Climb', 'Flaps Approach', and 'Landing Gear Approach' segments. These corrections were implemented by optimising drag-coefficient increments ($C_{D,\text{ Flaps-Climb}}$, $C_{D,\text{ Flaps-App}}$, $C_{D,\text{ Landing-Gear}}$) to represent the additional drag associated with flap and gear deployment, which was not captured in the default SUAVE drag build-up. In addition, the descent segment was calibrated by imposing a minimum idle throttle condition, in which a drag coefficient increment was calculated using Equation 3.7 and added to the aircraft model such that the lowest thrust value was equal to the minimum idle thrust for the given altitude and Mach number. The requirement for this additional drag during the descent operations may be explained by the inability to account for spillage drag in the current aerodynamic model, which resulted in insufficient drag for some descent operations when using the baseline drag prediction model.

$$C_{D_{\text{descent}}} = \frac{T_{\text{deficit}}}{p_{dynamic} \cdot S_{\text{ref}}} \tag{3.7}$$

For the B737-MAX model, the optimised aerodynamic coefficients for the B737-NG model were retained, and an additional L/D increment was introduced and calibrated to minimise the average climb and cruise fuel-flow errors across the 20 MAX calibration flights. This additional optimisation parameter was justified by the presence of aerodynamic upgrades on the B737-MAX airframe, which were not represented by the VLM and semi-empirical drag prediction methods used in this study, as discussed in Section 3.2.1.

3.5.2 Optimisation Results

An appropriate optimisation method was required to determine the optimal aerodynamic coefficients described in Section 3.5.1. Several approaches were evaluated, including gradient-based methods such as Sequential Least Squares Quadratic Programming (SLSQP) and L-BFGS, as well as Bayesian optimisation. Bayesian optimisation was ultimately the most effective to determine the optimal combination of the correction factors $C_{\text{fuselage, L}}$, $C_{\text{fuselage, D}}$, C_{wing}, C_{viscous}, and C_{trim} within the baseline SUAVE drag model. This was due to the highly non-linear response of the objective function, which prevented gradient-based algorithms from reliably converging to a global minimum. The balance between exploration and exploitation of the Bayesian optimisation algorithm enabled it to navigate the parameter space more efficiently and avoid local minima. In contrast, the configuration-specific optimisations for $C_{D,\text{ Flaps-Climb}}$, $C_{D,\text{ Flaps-App}}$, $C_{D,\text{ Landing-Gear}}$ and $L/D_{\text{increment}}$ exhibited more linear behaviour with respect to their objective functions, making SLSQP an appropriate and more computationally efficient choice for these cases. The optimisation results for each variable discussed in Section 3.5.1 are presented in Table 3.3.

3.6 Aircraft Model Validation

The complete aircraft model combined the optimised SUAVE aerodynamic framework with NPSS-based turbofan performance supplied through ANN surrogate models, together with a mission analysis module driven by representative flight paths derived from QAR data. Fuel burn measurements from the QAR database were used to validate the accuracy of the fuel-flow predictions generated by the B737-NG and B737-MAX aircraft models,

Table 3.3: Optimised calibration variables for the B737-NG and B737-MAX aircraft models

Aircraft Model	Opt. Variable	Initial Value	Opt. Range	Opt. Value
B737-NG	$C_{\text{fuselage, L}}$	1.14	1.10 – 1.20	1.1678
	C_{trim}	1.02	1.01 – 1.03	1.0154
	C_{wing}	1.10	1.05 – 1.20	1.0937
	$C_{\text{fuselage, D}}$	2.30	2.00 – 3.00	2.4676
	C_{viscous}	0.38	0.30 – 0.45	0.3548
	$C_{D,\text{ Flaps-Climb}}$	0.00	0.00 – 0.03	0.0137
	$C_{D,\text{ Flaps-App}}$	0.00	0.00 – 0.03	0.0133
	$C_{D,\text{ Landing-Gear}}$	0.00	0.00 – 0.06	0.0464
	Min. Idle Thrust (%)	0.00	3.00 – 7.00	3.0000
B737-MAX	$L/D_{\text{increment}}$ (%)	0.00	0.00 – 15.00	9.1595

where validation was conducted across a diverse set of missions to ensure that the model performed consistently over varying mission ranges, flight profiles, and take-off weights.

3.6.1 Boeing 737-800NG

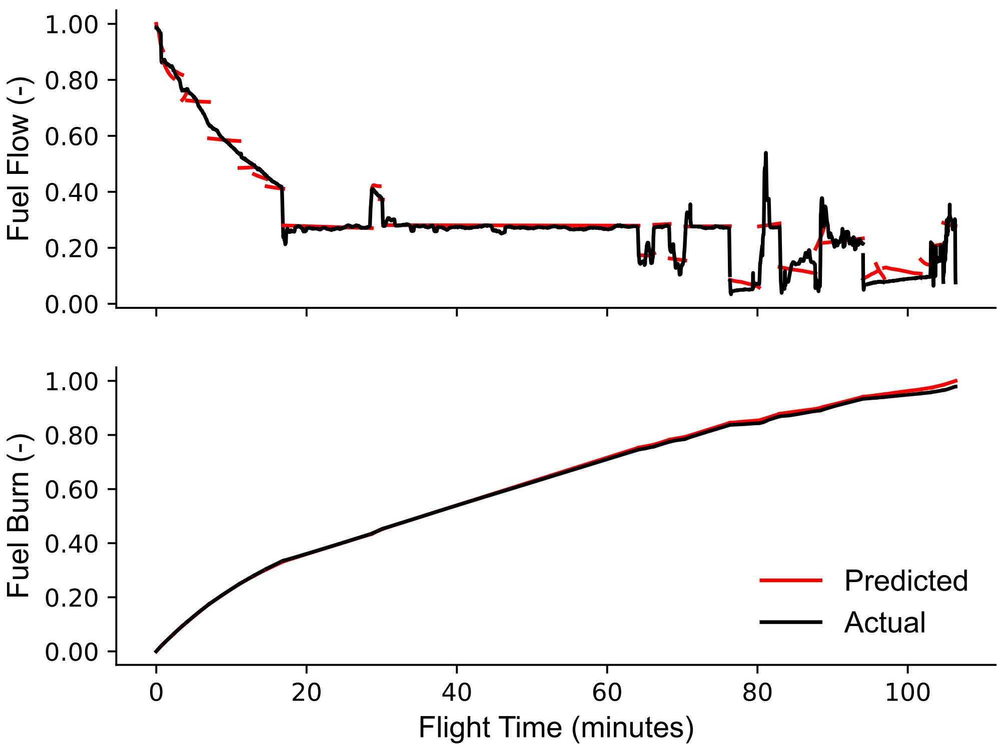

Figure 3.8: Normalised mission fuel-flow and cumulative fuel burn validation for the B737-NG aircraft model

Figure 3.8 presents an example of the fuel-flow and cumulative fuel-burn validation for a ∼600 NM B737-NG mission from the test dataset. The y-axis has been normalised to protect the sensitivity of the underlying QAR data. The model reproduces the measured fuel flow with high precision, particularly during the climb and cruise segments, which constitute the first ∼80 minutes of the mission and dominate overall fuel consumption. The initial and terminal segments, which represent phases of flight where high-lift and landing gear devices have been deployed, were also captured with high accuracy, demonstrating the effectiveness of the configuration-specific optimisations described in Section 3.5.

The performance of the model was strongest in flight segments with greater fuel consumption, reflecting the calibration strategy that prioritised accuracy during high-power operations such as climb and cruise. Consequently, accuracy deteriorated during low-thrust descent conditions, where the minimum-idle throttle setting was active for most sub-segments, amplifying the impact of the relatively large TSFC errors characteristic of idle operation, which was observed in Table 3.1. This behaviour is visible in the divergence between the predicted and measured fuel flow in the latter stage of the mission in Figure 3.8. However, the cumulative fuel burn shows that these discrepancies have limited overall impact: fuel-burn errors remain small towards the end of the mission, with total mission fuel burn over-predicted by only 2.2% relative to the QAR data.

While mission-specific validation helps assess the physical realism of each phase of flight, it is equally important to demonstrate accuracy under a wide range of operating conditions. The test dataset shown in Figure 3.5 was used to evaluate the mean fuel-burn error across 50 real-world B737-NG missions. The resulting average absolute error magnitudes of 2% closely matches the 1.9% obtained for the calibration dataset, indicating that the optimisation procedure in Section 3.5 generalised effectively across each set of flights. Overall, the model delivers strong predictive capability for a low-fidelity, physics-based framework applied to real-world operations.

3.6.2 Boeing 737-8200

Figure 3.9 shows an example of the fuel-flow and cumulative fuel-burn validation for a ∼1500 nm B737-MAX mission from the test dataset. The model exhibits the same general behaviour observed for the B737-NG (Section 3.6.1), with high accuracy during the climb and cruise segments and good agreement in the initial and terminal phases where flaps and landing gear are deployed. The model accuracy decreased during the descent phase due to prolonged idle-thrust operation, where engine performance predictions are less reliable. However, the impact of these discrepancies on cumulative fuel burn remains limited, as the total mission fuel consumption was over-predicted by just 0.9%.

The fuel-burn accuracy was also evaluated using the four flights in the B737-MAX test dataset, which produced a mean absolute error of 2.5%. For comparison, the calibration dataset achieved an average absolute error of 1.9% across 20 flights. Although the test-set error is slightly higher compared to the calibration dataset, the small sample size limits the extent to which the model's generalisation performance can be inferred. Overall, the B737-MAX model demonstrates fuel-burn accuracy comparable to that of the B737-NG model, which provides confidence in the robustness of the modelling framework.

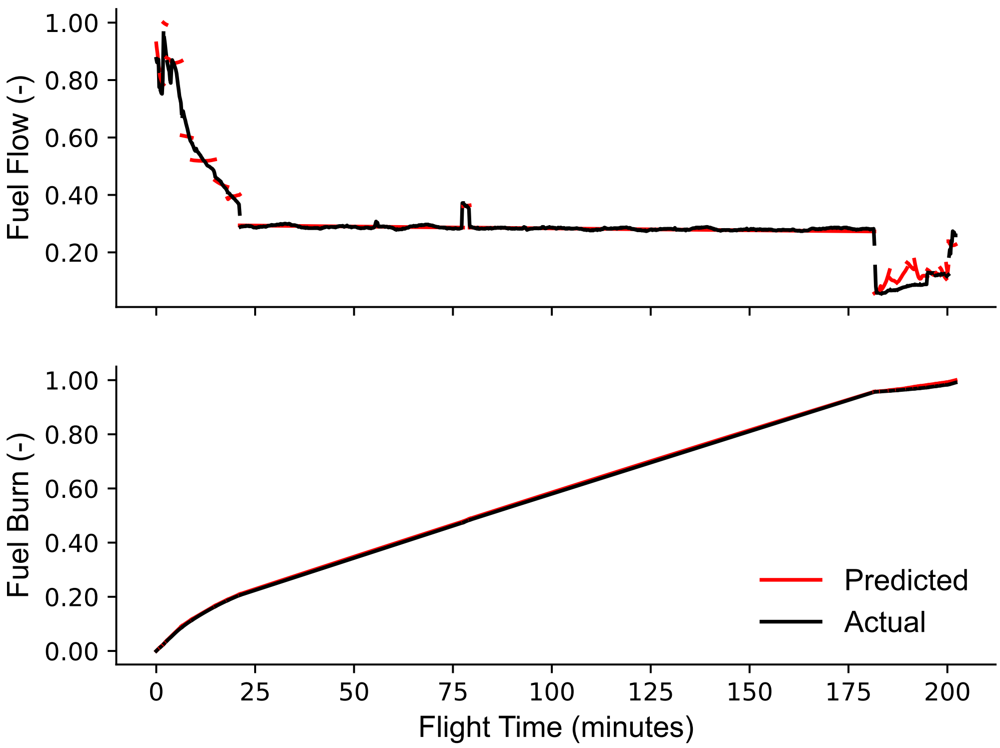

Figure 3.9: Normalised mission fuel-flow and cumulative fuel burn validation for the B737-MAX aircraft model

Chapter 4

Evaluating Decarbonisation Pathways

4.1 Introduction

SAF is widely regarded as a central pillar of aviation decarbonisation towards 2050 and is projected to offset 53–71% of aviation's carbon emissions [3]. SAF can be categorised according to its production pathway, including bio-SAF produced through hydrogenation of bio-derived feedstocks, and P2L SAF synthesised from green hydrogen and carbon, ideally captured from the atmosphere via DAC processes and powered entirely by renewable electricity. Green LH_2 represents an alternative P2L pathway for aviation and is considered alongside SAF within the ReFuelEU mandates for 2030 and 2050 [91]. These mandates specify a minimum sustainable fuel uptake of 6% at EU airports by 2030, increasing to 70% by 2050, with sub-targets for P2L fuels rising from 1.2% in 2030 to 35% by 2050 [91].

While bio-SAF pathways are expected to dominate near-term deployment – reflected in the structure of the ReFuelEU mandates – the present study focuses on P2L fuels. This emphasis is motivated by their low carbon intensity when produced using renewable electricity and by ongoing uncertainty surrounding the long-term scalability and sustainability of bio-derived carbon feedstocks [93, 95]. In addition, Ireland's substantial offshore wind resource, with a theoretical annual generation potential of 2852 TWh, presents a strategic opportunity for large-scale P2L fuel production [172].

Both P2L SAF and LH_2 offer credible pathways for decarbonisation; however, significant uncertainty remains regarding their economic viability. P2L SAF production is characterised by high energy requirements, which may limit its competitiveness [29]. Conversely, LH_2-powered aircraft face challenges associated with infrastructure provision and aircraft design, as LH_2 is not a drop-in replacement for Jet A-1 and requires cryogenic storage within the fuselage, resulting in in-flight performance penalties due to reduced volumetric energy density, as discussed in Section 2.3.5. However, engine cycle enhancements such as intercooling and recuperation have demonstrated potential to improve the thermal efficiency of LH_2-powered propulsion systems [81, 82]. Although several studies have compared the design-mission performance and market coverage of LH_2 aircraft against Jet A-1 and SAF [65, 78, 68, 9, 81], the existing literature lacks a comprehensive assessment of their real-world operational performance.

Therefore, this study aims to quantify and compare the real-world performance of LH_2 and SAF technologies through an operational case study of a European short-haul airline. The analysis comprises a fleet-wide simulation of a full day of airline operations, considering all flights to and from the island of Ireland under LH_2 and SAF scenarios. Fleet-level performance is evaluated in terms of in-flight fuel energy consumption and total energy consumption, quantified using Tank-to-Wake (TtW) and Well-to-Wake (WtW) energy metrics, respectively. An overview of the modelling framework is illustrated in Figure 4.1, highlighting the extended modelling elements to the validated flight simulation framework developed in Chapter 3. Specific objectives of this study include the following:

- Develop LH_2 propulsion system models for the CFM56-7B26 and LEAP-1B27 turbofan engines
- Implement and assess engine cycle enhancements for the baseline LH_2 propulsion configurations
- Design equivalent LH_2-powered B737-NG and B737-MAX aircraft across a range of GI values
- Perform a fleet-wide energy analysis over a complete operational schedule for SAF and LH_2 aircraft configurations
- Quantify the influence of fuel choice, aircraft technology level, GI, and IRE-based propulsion on fleet-level energy consumption and associated electricity costs

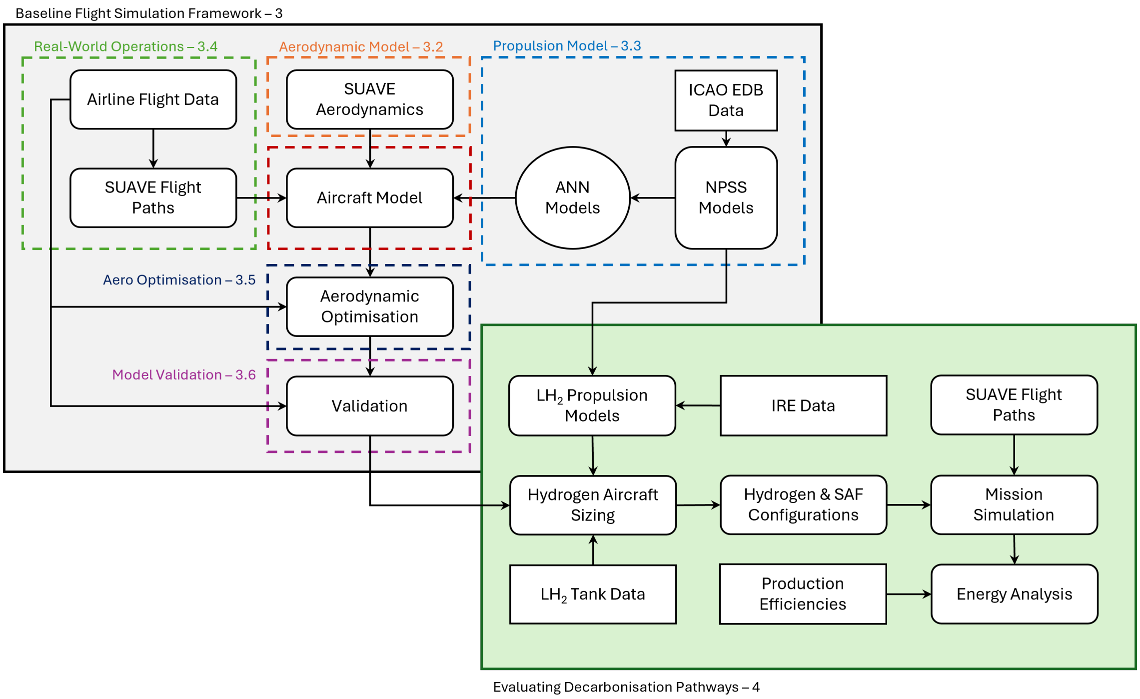

Figure 4.1: Modelling framework for evaluating LH_2 and SAF performance for real-world operations

4.1.1 Propulsion System

The propulsion system models for the hydrogen-powered aircraft were derived from the baseline CFM56-7B26 and LEAP-1B27 turbofan models developed in Section 3.3 and shown in Figure 3.3. The LH_2 engine configurations were implemented by modifying the fuel properties, increasing the LHV from 42.8 MJ/kg for Jet A-1 to 119.96 MJ/kg for hydrogen [71]. Consequently, the LH_2 propulsion models account only for differences in fuel specific energy, with no further changes made to the engine cycle or component characteristics. Treating hydrogen solely as an energy carrier was a simplification within this study, as it neglects the minor thermal efficiency improvements that may arise from hydrogen combustion due to its higher specific heat capacity [68].

Intercooling & Recuperation

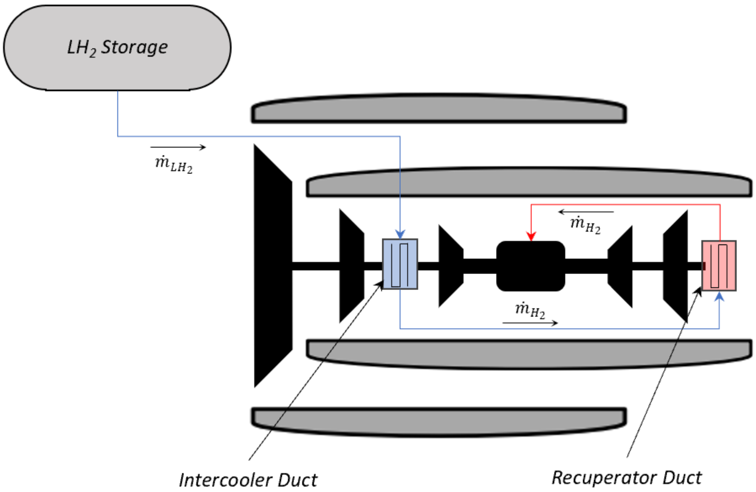

Figure 4.2: NPSS propulsion system model for intercooled and recuperated hydrogen-powered turbofan

A preliminary IRE model was developed to assess the potential performance benefits of LH_2-powered aircraft. The IRE system was implemented in NPSS using data obtained from a recent compact heat exchanger design for LH_2 propulsion systems [81]. While the original study focused on design-point performance, the present work extends this analysis to evaluate the impact of IRE technology across a representative range of airline operations. The NPSS IRE architecture, illustrated in Figure 4.2, uses the low-temperature LH_2 fuel to reduce the core air temperature upstream of the HPC, as described by Equation 4.1. This reduces the required HPC work while increasing the fuel temperature to approximately 350 K. The hydrogen fuel subsequently recovers heat from the core exhaust flow, raising its temperature to approximately 750 K before entering the combustor with increased enthalpy [81].

$$T_{\text{air}_2} = T_{\text{air}_1} - \frac{\dot{Q}_{\text{IC}}}{\dot{m}_{\text{air}} \cdot c_{p_{\text{air}}}} \tag{4.1}$$

As the present study constitutes a scoping exercise, heat transfer within the HEX ducts was not modelled explicitly. Instead, heat transfer rates were correlated using data published by Patrão et al. [81]. The reference IRE configuration considered in that study corresponds to a higher engine technology level and operates with reduced fuel-flow and core mass-flow rates relative to the CFM56-7B26 and LEAP-1B27 LH_2 configurations examined here. To approximate equivalent IRE performance for the current models, the heat transfer values reported by Patrão et al. [81] were scaled with fuel flow at TOC, cruise, and RTO. The resulting heat transfer parameters are summarised in Table 4.1. Core mass-flow values from the CFM56-7B26 and LEAP-1B27 NPSS models at TOC, RTO, and cruise were then used to extrapolate heat transfer rates across the full range of operating conditions. Within NPSS, $-\dot{Q}_{\mathrm{IC}}$ was applied to the intercooler duct, $-\dot{Q}_{\mathrm{RC}}$ to the core exhaust duct, and $\dot{Q}_{\mathrm{IC}} + \dot{Q}_{\mathrm{RC}}$ was added to the combustor inlet.

Table 4.1: Intercooling and recuperation heat transfer, core mass flow, and ΔTSFC data for LH_2 IRE configurations.

Configuration		**CFM56-7B26**			**LEAP-1B27**		
Op. Point		Cruise	TOC	RTO	Cruise	TOC	RTO
Intercooler	Q_{IC} (kW)	612	831	2307	537	730	2090
	$\dot{m}_{\mathrm{air}}$ (kg/s)	22.2	24.8	56.3	19.2	21.6	50.2
Recuperator	Q_{RC} (kW)	683	876	2544	599	794	2304
	$\dot{m}_{\mathrm{air}}$ (kg/s)	17.3	19.6	45.8	15.3	17.6	40.6
NPSS ΔTSFC		−5.0%	−6.4%	−8.2%	−5.2%	−6.1%	−7.7%
Patrão ΔTSFC [81]		−5.3%	−5.6%	−7.7%	−5.3%	−5.6%	−7.7%

The air-side pressure drop across the HEX ducts was calculated within NPSS using Equation 4.2 [83], where G represents the mass flux, ρ the density, σ the ratio of free-flow to frontal area, f the friction factor, L_x the HEX length in the air-flow direction, and $\bar{\rho}$ the average air density between the inlet and outlet stations. Furthermore, a constraint of $\Delta p < 9\%$ was implemented to aid convergence across the full range of operating points. Integration of the IRE system resulted in an additional 326 kg per engine and a propulsion system length increase of 1.04 metres [81], which were applied consistently across all LH_2-IRE aircraft configurations described in Section 4.1.4.

$$\Delta p_{\mathrm{air}} = \frac{G_{\mathrm{air}}^2}{2 \cdot \rho_{\mathrm{air}_1}} \left(\left(1 - \sigma_{\mathrm{air}}^2\right) \left(\frac{\rho_{\mathrm{air}_1}}{\rho_{\mathrm{air}_2}} - 1 \right) + f \cdot \frac{4 \cdot L_x}{D_{h_{\mathrm{air}}}} \frac{\rho_{\mathrm{air}_1}}{\bar{\rho}_{\mathrm{air}}} \right) \tag{4.2}$$

Despite the simplified modelling approach, the TSFC reductions reported in Table 4.1 show good agreement with those obtained by Patrão et al. [81]. A maximum discrepancy of 0.8 percentage points was observed for the ΔTSFC values at the TOC operating point for the CFM56-7B26 engine. At lower power settings, increased TSFC values were predicted due to reduced heat transfer combined with the additional pressure loss across the HEX ducts. A higher-fidelity treatment would be required to assess the validity of these predictions outside the cruise, TOC, and RTO operating regimes, which was beyond the scope of the present study.

4.1.2 Tank Sizing

The first step in developing the airframe design for equivalent LH_2-powered B737 aircraft configurations was the integration of an appropriately sized LH_2 storage tank within the fuselage. A clean-sheet tank structural design was beyond the scope of this evaluation study; therefore, a simplified sizing approach was adopted by selecting target GI values informed by relevant literature, as discussed in Section 2.3.2. Although the analysis by Huete and Pilidis [67] demonstrated that spherical tanks offer superior performance due to their mechanical advantages, a single spherical tank would not provide sufficient fuel capacity for LH_2-powered aircraft designs with equivalent range and payload capabilities compared to the baseline configurations. Consequently, a cylindrical tank configuration was selected. Furthermore, while some studies have proposed the distribution of tanks between the forward and aft fuselage sections to address stability considerations [68, 78], in the present work only an aft fuselage tank was implemented, as detailed stability analysis was outside the scope of this study. This simplified configuration is consistent with the approach adopted by Mukhopadhaya and Rutherford [65] for a similarly sized aircraft.

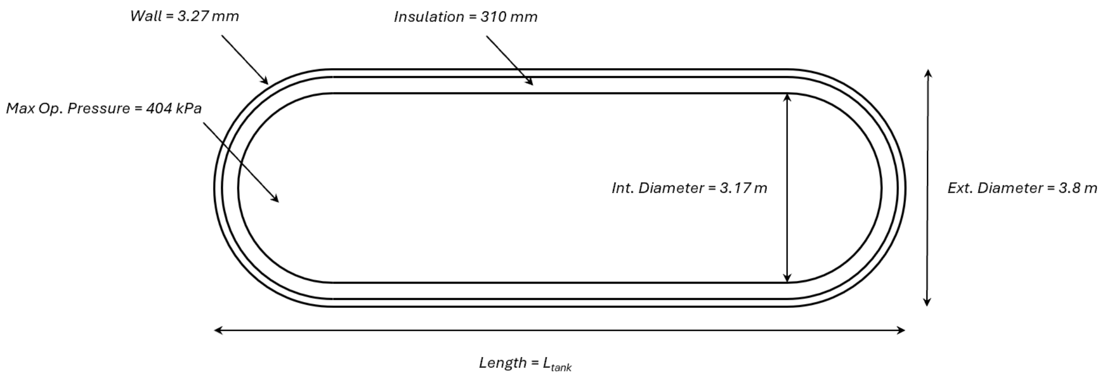

Figure 4.3: Diagram of the generic LH_2 tank design used for hydrogen aircraft configurations

The cylindrical LH_2 tank configuration is shown in Figure 4.3. For each hydrogen-powered aircraft variant, the tank was sized using the required fuel mass in combination with a prescribed GI value to determine the tank length, L_{tank}. The tank diameter and wall and insulation thicknesses were informed by the detailed parametric study of Huete and Pilidis [67], who designed a 100 m^3 cylindrical tank for a short- to medium-haul aircraft with a maximum operating pressure of 404 kPa and a 24-hour dormancy time, yielding a GI value of 0.66. While this value exceeds those commonly reported in the literature, it may be considered an optimistic estimate for an EIS timeframe of 2035–2050, where more conservative studies report GI values in the range of 0.2–0.38 [9, 65]. To account for this uncertainty and to assess the sensitivity of the study outcomes to tank performance assumptions, three GI values (0.33, 0.50, 0.66) were considered. An external tank diameter of 3.8 metres, which was slightly smaller than the 4 metre diameter adopted by Huete and Pilidis [67], was selected to ensure compatibility with the B737 fuselage, which has an effective diameter of 3.88 metres [164].

4.1.3 Aircraft Sizing

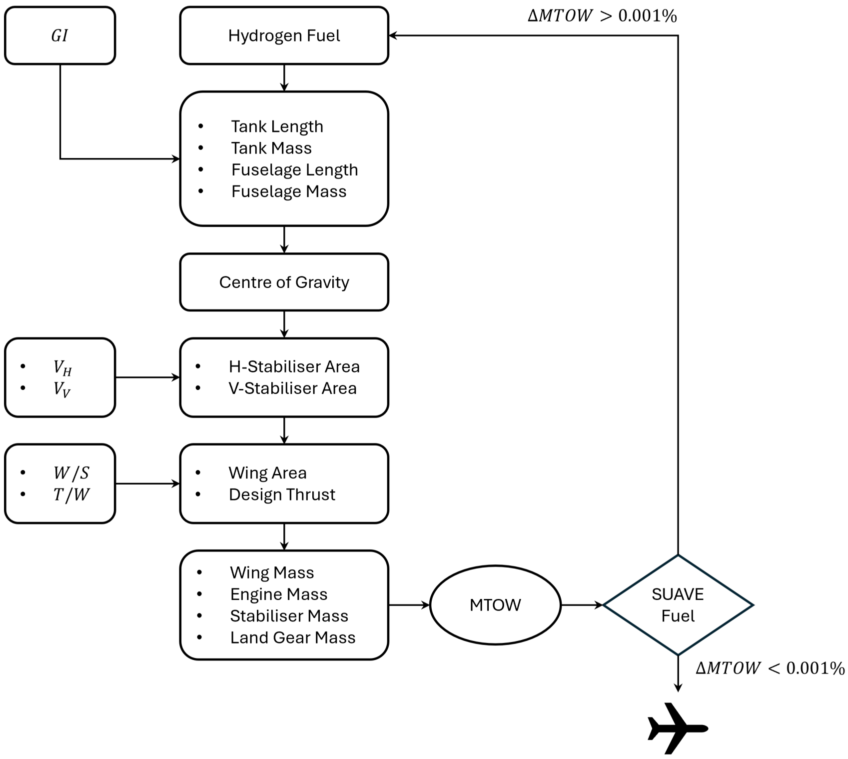

Figure 4.4: Iterative sizing process used to design LH_2 aircraft configurations

Aircraft sizing was performed using the iterative procedure shown in Figure 4.4. The loop was initialised with an estimate of the LH_2 fuel mass, derived from the equivalent energy content of the jet fuel required for the baseline aircraft design mission. This initial fuel mass was converted into fuel volume using the volumetric density of LH_2, enabling calculation of the tank length parameter shown in Figure 4.3, while the fuel mass and target GI value were used to determine the corresponding LH_2 tank mass. The resulting tank geometry and mass were then incorporated into the airframe model, allowing the updated aircraft geometry and total mass properties to be defined, including the MTOW. The validated flight simulation framework described in Chapter 3 was subsequently used to simulate the performance of the modified aircraft over a 2950 nm design mission followed by a 250 nm reserve segment, yielding an updated estimate of mission fuel burn. This sizing loop was repeated until convergence was achieved, where convergence was defined by a change in MTOW of less than 0.001% between successive iterations.

Geometry

The methods proposed by Mukhopadhaya and Rutherford [65] were used to generate the updated airframe geometry for each LH_2 aircraft configuration. The external tank length was calculated using Equation 4.3, where V denotes the volume, D the diameter, and the subscripts 'int' and 'ext' refer to internal and external geometric parameters, respectively.

This external tank length was added to the baseline fuselage length to determine the total fuselage length of each LH_2 configuration. The additional fuselage wetted area introduced by the extension was estimated by approximating the added section as a cylindrical segment.

$$L_{\text{tank}} = \left(\frac{V_{\text{fuel}-\frac{1}{6}\cdot\pi\cdot D_{\text{int}}^3}}{\frac{1}{4}\cdot\pi\cdot D_{\text{int}}^2} \right) + D_{\text{ext}} \tag{4.3}$$

Changes in wing area were calculated using Equation 2.2, with the wing loading W/S held constant to ensure sufficient lift was produced as the mass was varied for the LH_2 configurations. Similarly, the horizontal and vertical stabiliser areas were updated by maintaining constant tail volume coefficients relative to the baseline aircraft, as defined in Equations 2.4 and 2.5. Because the distance between the aerodynamic centres of the wing and stabilisers directly affects the required stabiliser area, the wing was re-positioned along the fuselage following the extension to maintain alignment with the updated centre of gravity. The centre of gravity of the LH_2 aircraft was computed by accounting for the LH_2 tank and fuel as a point mass located at the midpoint of the fuselage extension.

Mass

Although LH_2 aircraft benefit from reduced fuel mass due to the higher specific energy of hydrogen, additional mass penalties arise from the LH_2 storage tank and fuselage extension, while the mass of the wing, stabilisers, propulsion system, and landing gear may increase or decrease depending on the resulting airframe modifications. The tank mass was calculated using the fuel mass and the GI, as described in Equation 2.1. The masses of the fuselage, wing, stabilisers, and landing gear were estimated using the SUAVE weight estimation framework [135], which is based on correlations derived from Shevell [166]. The mass of the propulsion system was scaled in proportion to thrust to maintain a constant thrust-to-weight T/W ratio, as defined in Equation 2.3. The final MTOW of each LH_2 configuration was then calculated using Equation 4.4, where Δm_{fuel} represents the difference in design-mission fuel mass between the conventional and LH_2 aircraft, and ΔOEW denotes the total change in operating empty weight, as defined in Equation 4.5.

$$MTOW = MTOW_{\text{baseline}} + \Delta m_{\text{fuel}} + \Delta OEW \tag{4.4}$$

$$\Delta OEW = \Delta m_{\text{fuselage}} + \Delta m_{\text{wing}} + \Delta m_{\text{stabilisers}} + \Delta m_{\text{landing gear}} + \Delta m_{\text{engine}} + \Delta m_{\text{tank}} \tag{4.5}$$

4.1.4 Aircraft Configurations

Figure 4.5 presents representative SUAVE-generated geometries for the conventional and LH_2-powered aircraft, shown in Figures 4.5(a) and 4.5(b), respectively. The red markers show the control point locations used in the VLM aerodynamic calculations, while the darker fuselage section in Figure 4.5(b) highlights the location and size of the LH_2 fuel tank.

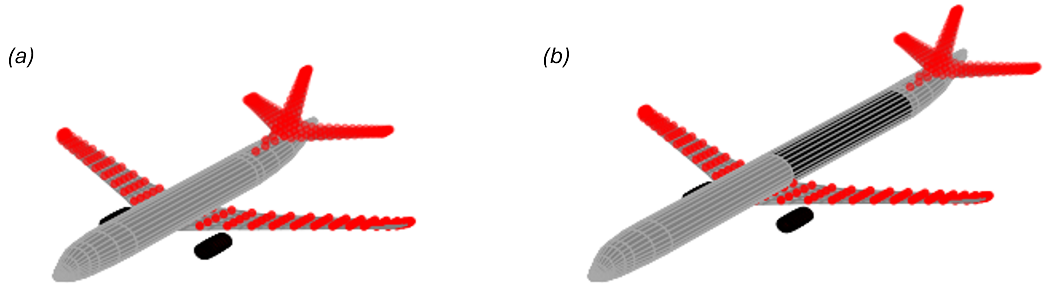

Figure 4.5: SUAVE model representations for the (a) B737-NG aircraft (b) B737-NG-LH_2-0.33 aircraft

Key design parameters for all aircraft configurations are summarised in Table 4.2, where $m_{\text{des-fuel}}$ denotes the design-mission fuel burn. Within Table 4.2, a B737-NG-LH_2-0.33 configuration corresponds to a B737-800NG aircraft powered by a baseline LH_2 engine and sized using a GI of 0.33, whereas B737-MAX-LH_2-IRE-0.50 refers to an LH_2-powered B737-8200 aircraft sized with a GI of 0.50 and equipped with an intercooled and recuperated LH_2 engine. The SAF-labelled aircraft represent the conventional configurations, assuming identical fuel properties to Jet A-1, and are included in Table 4.2 for comparison purposes.

Table 4.2: Final sizing parameters for B737-NG and B737-MAX aircraft models

Aircraft	**B737-NG**			**B737-MAX**		
	MTOW (kg)	L_{fuselage} (m)	$m_{\text{des-fuel}}$ (kg)	MTOW (kg)	L_{fuselage} (m)	$m_{\text{des-fuel}}$ (kg)
SAF	79 016	38.0	18 992	82 644	39.1	16 741
LH_2-0.33	105 809	57.2	9 784	103 044	55.1	7 994
LH_2-0.50	84 191	54.0	8 006	86 941	53.1	6 896
LH_2-0.66	77 276	53.2	7 532	81 173	52.5	6 554
LH_2-IRE-0.50	83 706	53.3	7 636	86 635	52.5	6 573

The influence of the GI on LH_2 aircraft sizing trends is evident in Table 4.2. As GI decreases, the MTOW, fuselage length, and design-mission fuel burn increase rapidly due to a compounding effect: a higher tank mass leads to increased fuel consumption, which requires a longer tank and larger airframe, which in turn results in greater fuel burn and a further extension to the LH_2 tank length. This feedback loop was less pronounced for the B737-MAX compared to the B737-NG aircraft, as observed by the less-exaggerated response in the aircraft size, weight, and fuel burn as the GI was varied. This was due to the increased fuel efficiency of the B737-MAX aircraft, which consumed 12% less fuel than the B737-NG aircraft for its design mission for the conventional (SAF) configuration. With increasing fuel efficiency, the relative impact of the in-flight performance penalties associated with LH_2-powered aircraft are reduced, and therefore the influence of the GI on the aircraft performance is less significant. This highlights the importance of accurate fuel-burn modelling for future aircraft when assessing LH_2 operations and quantifying the influence of GI. The impact of the IRE model is also apparent in Table 4.2: despite yielding MTOW values comparable to the corresponding LH_2-0.50 configurations, LH_2-IRE configurations achieved reductions in design-mission fuel burn of 4.6% for the B737-NG and 4.7% for the B737-MAX.

4.2 Case-Study Setup

4.2.1 Aircraft Operations

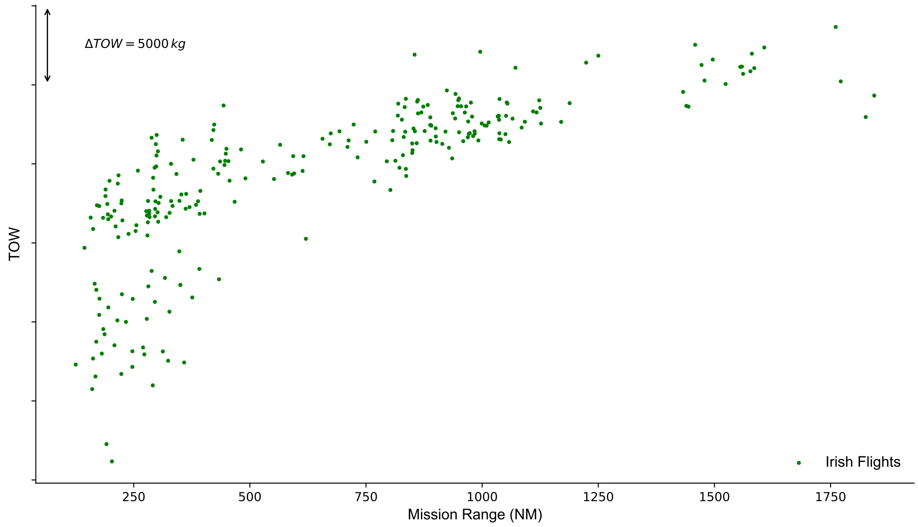

Figure 4.6: Irish flight operations within wider flight database used for the LH_2-SAF case-study

To evaluate the performance of the various aircraft configurations, each design listed in Table 4.2 was simulated over an operational flight schedule using the validated modelling framework described in Chapter 3. The operational schedule selected for the LH_2–SAF case study comprised all flights within the full database operating to and from Irish airports – specifically Dublin, Belfast, Cork, Shannon, and Knock – and are illustrated in Figure 4.6 highlighting the wide range of mission range and TOW values within the data. The resulting schedule contained 257 B737-NG flights, with an average mission range of 659 NM. Due to the limited availability of operational data for the B737-MAX, 25% of the 257 B737-NG flights were simulated using the B737-MAX aircraft model. This proportion was chosen to reflect the composition of the airline fleet at the time of the study, which consisted of 411 B737-NG and 137 B737-MAX aircraft [173].

4.2.2 Take-Off Weights

The QAR data for each flight shown in Figure 4.6 included a recorded TOW and onboard fuel mass corresponding to conventional B737-NG operations. To approximate equivalent real-world operations for the LH_2 configurations, and for B737-MAX flights derived from B737-NG trajectories, equivalent TOW values were estimated. For the B737-NG LH_2 configurations, TOW was calculated by augmenting the conventional TOW with the corresponding ΔOEW and adjusting the onboard fuel mass to maintain the same relative tank fill fraction used in the conventional B737-NG flight.

The TOW calculation is described in Equation 4.6, where TOW_{LH_2} denotes the estimated TOW of the LH_2-powered aircraft, TOW_{SAF} and $m_{\text{fuel-SAF}}$ correspond to the recorded TOW and fuel mass from the QAR data, and $m_{\text{fuel-LH}_2}$ is the equivalent LH_2 fuel mass carried on the flight. $m_{\text{fuel-LH}_2}$ was computed using Equation 4.7, in which $m_{\text{des-fuel-LH}_2}$ and $m_{\text{des-fuel-SAF}}$ represent the design-mission fuel burn of the LH_2 and conventional aircraft, respectively, as reported in Table 4.2. For flights simulated with the B737-MAX model, an additional 3000 kg was added to the estimated TOW to account for the higher MTOW of the conventional B737-MAX relative to the B737-NG.

$$TOW_{\text{LH}_2} = TOW_{\text{SAF}} + (m_{\text{fuel-LH}_2} - m_{\text{fuel-SAF}}) + \Delta OEW \tag{4.6}$$

$$m_{\text{fuel-LH}_2} = m_{\text{des-fuel-LH}_2} \cdot \left(\frac{m_{\text{fuel-SAF}}}{m_{\text{des-fuel-SAF}}} \right) \tag{4.7}$$

4.2.3 Well-to-Tank Efficiency

The P2L fuels considered in this study include SAF-DAC, produced via the synthesis of green hydrogen with carbon captured through a DAC process, and green LH_2, generated by electrolysis of water followed by liquefaction to $-253\,°\text{C}$. For both fuels, the electricity supply was assumed to be fully renewable. In addition, SAF produced via FT and AtJ pathways – both ASTM-approved routes utilising biogenic feedstocks – were included for comparison as near-term low-carbon SAF options [29]. All SAF and LH_2 production pathways were assumed to be zero-carbon or net-zero on the basis of their reported low carbon intensity values [29]. Therefore, no direct emissions analysis was undertaken in the present study. A complete life-cycle assessment of the fuels was also beyond the scope of this work; however, comprehensive life-cycle impact studies are available in the literature and are referenced here for completeness [174, 86, 175].

Table 4.3: Well-to-tank production efficiencies used for SAF and green LH_2 pathways

Fuel Type	**Well-to-Tank Efficiency**
SAF-DAC	30.3% [29]
SAF-ATJ	39.3% [29]
SAF-FT	43.6% [29]
Green LH_2	55.7% [31]

The Well-to-Tank (WtT) efficiency quantifies the energy efficiency of each fuel production pathway, defined as the ratio of useful fuel energy produced to the total energy input required. The WtT efficiencies for the SAF pathways listed in Table 4.3 were selected based on a detailed assessment of SAF production processes, with the SAF-DAC value representing an average across three DAC-based synthesis routes with differing efficiencies [29]. The LH_2 WtT efficiency was estimated assuming an electrolysis efficiency of 75%, a liquefaction efficiency of 75%, and a distribution efficiency of 99% [31], resulting in an overall WtT efficiency of 55.7%. This value is consistent with those reported in comparable studies, where LH_2 WtT efficiencies typically range between 56—58% [65, 9]. The final WtT efficiencies used for each fuel pathway are summarised in Table 4.3.

4.3 Results & Discussion

4.3.1 In-Flight Energy Consumption

The operational schedule described in Section 4.2.1 was simulated to obtain the fuel burn for each flight and aircraft configuration. Each configuration was then assessed in terms of its Tank-to-Wake (TtW) energy consumption, defined here as the in-flight energy content of the fuel consumed during the mission. TtW energy was calculated by multiplying the fuel burn by the corresponding LHV, as given in Equation 4.8.

$$E_{TtW} = m_{\text{fuel}} \cdot LHV \tag{4.8}$$

B737-NG

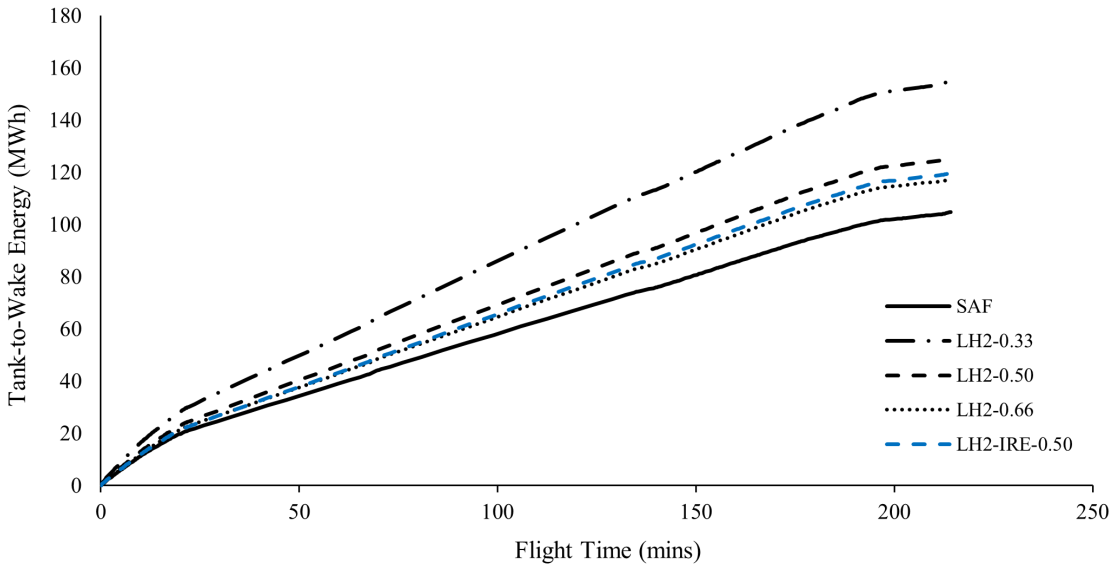

Figure 4.7: Tank-to-Wake energy performance of B737-NG LH_2 and SAF configurations for a 1500 NM mission

To illustrate the relative TtW performance of the different aircraft designs, a representative flight with a mission range of approximately 1500 NM was selected from the operational schedule, as shown in Figure 4.7. The results demonstrate the detrimental impact of low GI values on in-flight energy performance. In particular, the LH_2-0.33 configuration exhibited a 48.4% increase in TtW energy consumption relative to the SAF aircraft, primarily due to its substantially higher TOW, which was 43% greater than that of the SAF configuration. This increased weight led to higher energy consumption across all flight phases, with the most pronounced effect occurring during the climb phase as a result of increased induced drag. In contrast, the LH_2-0.50 and LH_2-0.66 configurations exhibited more moderate penalties of 19.8% and 12.1%, respectively, reinforcing the compounding impact of GI on in-flight energy performance which was discussed in Section 4.1.4. The LH_2-IRE configuration with a GI of 0.50 further reduced the performance penalty to 14.4%, indicating the potential of IRE technology to partially mitigate the in-flight performance gap between LH_2 and SAF.

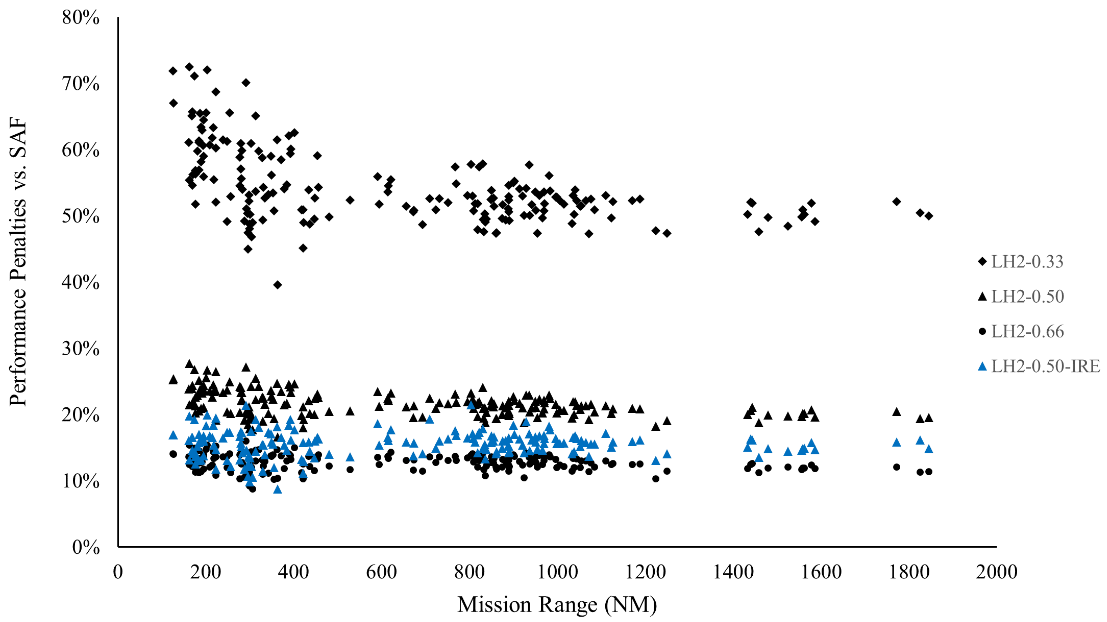

Figure 4.8: In-flight energy performance penalties for LH_2 aircraft vs. SAF for all B737-NG operations

Figure 4.8 presents the TtW energy performance penalties – defined as the relative increase in in-flight energy consumption – for each LH_2 configuration compared to the SAF baseline across the B737-NG operations shown in Figure 4.6. A notable trend was observed for the LH_2-0.33 configuration, which yielded substantially higher performance penalties for short-range missions below 500 NM, exceeding 70% in some cases. The relatively higher energy penalties for these flights were caused by the increased OEW combined with reduced fuel-mass savings in comparison to longer range missions, which carry more fuel. Similar, though less severe, trends were observed for the remaining LH_2 configurations, with modest increases in relative energy penalties at shorter ranges, reaching maximum values of 27.7% and 16.0% for the LH_2-0.50 and LH_2-0.66 aircraft, respectively.

B737-MAX

Consistent with the previous analysis, a representative flight with a mission range of approximately 1500 NM was selected to evaluate the TtW energy performance of the B737-MAX aircraft configurations, as shown in Figure 4.9. The LH_2-0.33 configuration produced a 35.5% increase in TtW energy consumption relative to the SAF baseline, which decreased to 15.3% and 9.1% for the LH_2-0.50 and LH_2-0.66 configurations, respectively. The LH_2-IRE configuration demonstrated a similar relative improvement to that observed for the B737-NG aircraft, reducing the energy performance penalty to 10.8% compared to the SAF B737-MAX aircraft.

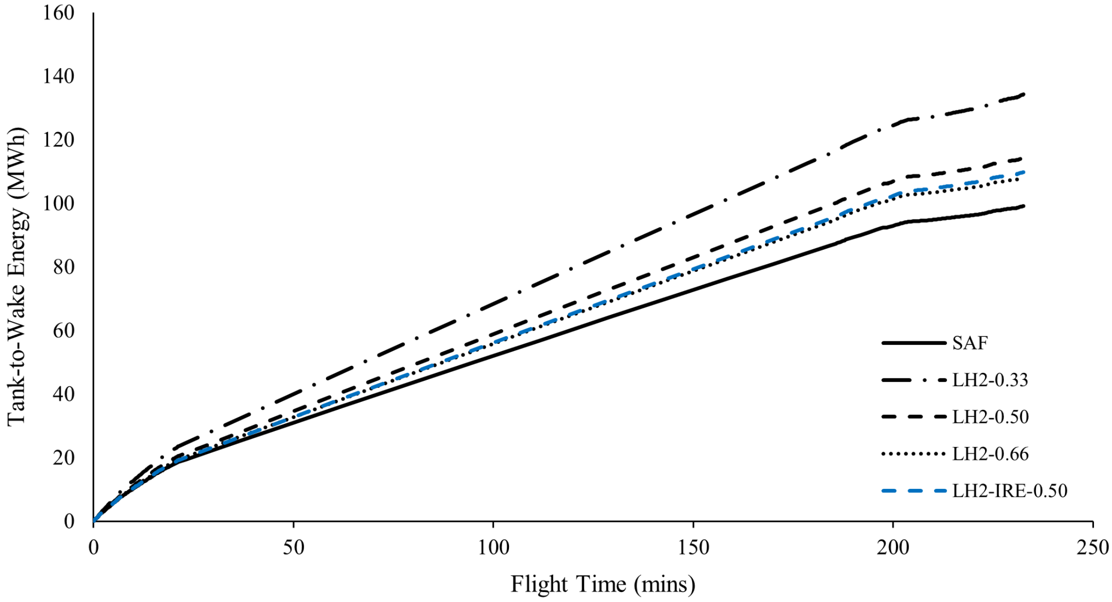

Figure 4.9: Tank-to-Wake energy performance of B737-MAX LH_2 and SAF configurations for a 1500 NM mission

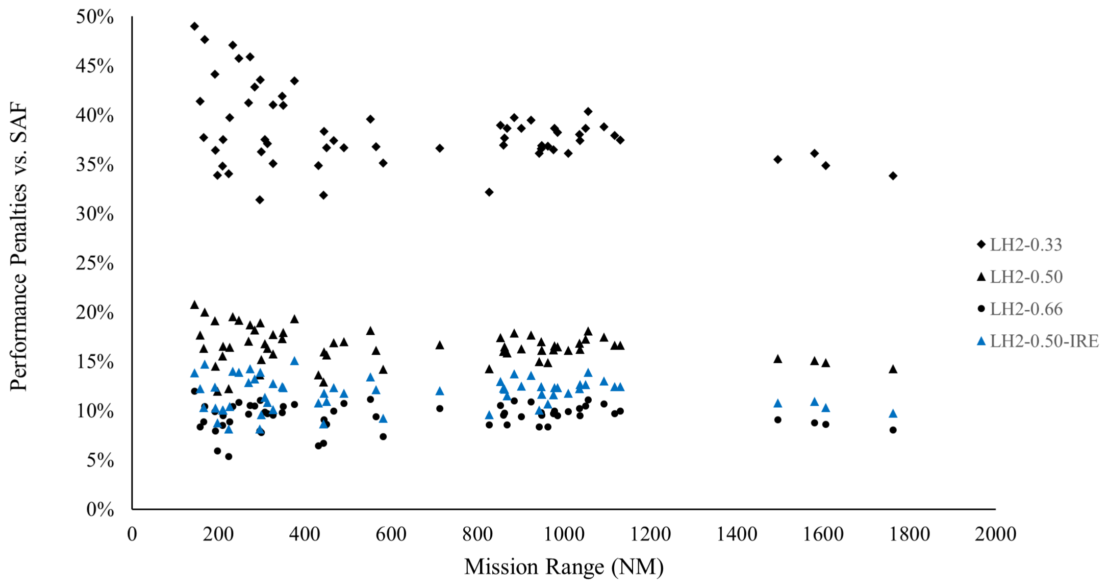

Figure 4.10: In-flight energy performance penalties for LH_2 aircraft vs. SAF for all B737-MAX operations

Figure 4.10 presents the TtW energy performance penalties across the full range of B737-MAX operations. Overall reductions in performance penalties are observed relative to the B737-NG case, while similar trends persist for short-range missions. In particular, the largest penalties occur at shorter mission ranges, reaching maximum values of 49.0%, 20.8%, and 12.0% for the LH_2-0.33, LH_2-0.50, and LH_2-0.66 configurations, respectively. The relationship between aircraft fuel efficiency and the sensitivity to the GI parameter is evident from a comparison of Figures 4.8 and 4.10. As fuel efficiency improves, the influence of GI on in-flight energy penalties decreases, highlighting the importance of accurately projecting fuel-burn performance for future aircraft when comparing LH_2 and SAF operations.

4.3.2 Total Energy Consumption

The Well-to-Wake (WtW) energy consumption was calculated by dividing the TtW energy by the WtT efficiency of each fuel listed in Table 4.3, as defined in Equation 4.9. Fleet-wide WtW energy results for the three SAF candidates and three LH_2 configurations are reported in Table 4.4 for both individual aircraft operations and the total fleet. SAF-DAC was found to be substantially more energy intensive than all LH_2 configurations, requiring 43.8% more energy than the LH_2-0.33 case across the total fleet. SAF-ATJ achieved a 4.9% reduction in total fleet energy consumption relative to LH_2-0.33; however, it was 3.1% more energy intensive than the corresponding B737-MAX LH_2-0.33 operations, suggesting that ATJ may be less competitive than LH_2 for more fuel-efficient aircraft. SAF-FT yielded a 14.3% reduction in WtW energy compared to the LH_2-0.33 fleet, but was outperformed by the LH_2-0.50 and LH_2-0.66 configurations, where SAF-FT exhibited 6.5% and 14.2% higher energy consumption relative to these aircraft, respectively.

$$E_{WtW} = \frac{E_{TtW}}{\eta_{WtT}} \tag{4.9}$$

The minimum cost of renewable electricity required to support these operations was estimated using the Levelised Cost Of Electricity (LCOE) associated with Europe's North Sea offshore wind power hub, which is projected to deliver renewable electricity at a break-even cost of €40/MWh beyond 2030 [176]. The use of LCOE was preferred given the assumption that future fuel production would be entirely based on renewable electricity, and because projected fuel costs for LH_2 and SAF remain highly uncertain. Nevertheless, it is well established that P2L SAF pathways are likely to incur higher costs than green LH_2 due to additional production processes and capital requirements. Although the LH_2-0.50 and LH_2-0.66 fleets outperform all SAF candidates in terms of both WtW energy consumption and estimated electricity cost, these results must be interpreted alongside the substantial infrastructure requirements, aircraft development costs, and operational complexity associated with LH_2 aircraft – factors that are beyond the scope of this study. As a result, near-term SAF pathways such as ATJ and FT may represent more practical options in the event that sufficient feedstock is available. In contrast, SAF-DAC incurs significantly higher energy and electricity costs – up to €617,840 more than the LH_2-0.66 configuration for the 257-flight schedule – which may outweigh the advantages of retaining a drop-in fuel solution for long-term decarbonisation strategies.

Table 4.4: Fleet-wide energy and LCOE results for LH_2 versus SAF operations, for a total of 257 flights (193 B737-NG, 64 B737-MAX)

Configuration	B737-NG		B737-MAX		Total Fleet		
	E_{TtW} (MWh)	E_{WtW} (MWh)	E_{TtW} (MWh)	E_{WtW} (MWh)	E_{TtW} (MWh)	E_{WtW} (MWh)	E_{WtW} (€)
SAF-DAC	9 273	30 572	2 712	8 942	12 435	39 514	1 580 560
SAF-ATJ	9 273	23 594	2 712	6 901	12 435	30 495	1 219 800
SAF-FT	9 273	21 267	2 712	6 220	12 435	27 487	1 099 480
LH_2-0.33	14 139	25 384	3 728	6 694	17 867	32 078	1 283 120
LH_2-0.50	11 229	20 161	3 152	5 658	14 381	25 819	1 032 760
LH_2-0.66	10 439	18 741	2 967	5 327	13 406	24 068	962 720

4.3.3 Intercooling & Recuperation Benefits

Fleet-wide energy results for the LH_2 and LH_2-IRE configurations are presented in Table 4.5, where a single GI value of 0.50 was considered to reduce the number of flight simulations required. The LH_2-IRE configurations for the B737-NG and B737-MAX aircraft achieved energy reductions of 4.6% and 3.9%, respectively, relative to their baseline LH_2 counterparts, corresponding to an overall fleet-wide reduction of 4.4%. While these percentage reductions may appear modest at the individual-flight level, their cumulative impact across the full operational schedule is substantial. For the 257-flight case study, this equates to energy savings exceeding 1 GWh and a reduction in electricity costs of approximately €46,000 for a small portion of the airline's daily flights, alleviating the demand on renewable electricity resources and improving the economic viability of LH_2-powered operations. Overall, the IRE results further strengthen the case for LH_2-powered aircraft and indicate that such technologies may play an enabling role in the transition towards zero-carbon aviation.

Table 4.5: Fleet-wide energy and LCOE results for LH_2 and LH_2-IRE aircraft configurations, for a total of 257 flights (193 B737-NG, 64 B737-MAX)

Configuration	B737-NG		B737-MAX		Total Fleet		
	E_{TtW} (MWh)	E_{WtW} (MWh)	E_{TtW} (MWh)	E_{WtW} (MWh)	E_{TtW} (MWh)	E_{WtW} (MWh)	E_{WtW} (€)
LH_2-0.50	11 229	20 161	3 152	5 658	14 381	25 819	1 032 760
LH_2-0.50-IRE	10 713	19 233	3 029	5 439	13 742	24 672	986 880

4.4 Key Findings & Interpretation

An operational case study was conducted to evaluate the fleet-wide energy performance of LH_2-powered and SAF-powered B737-NG and B737-MAX aircraft for a large short-haul European airline. Conventional SAF aircraft, together with the developed LH_2 and LH_2-IRE configurations, were simulated over a full day of airline operations to and from the island of Ireland, comprising 257 flights. These simulations were performed using the validated low-fidelity aircraft modelling framework described in Chapter 3, enabling accurate estimation of real-world operational performance. The configurations were compared in terms of TtW and WtW energy consumption, as well as the renewable electricity cost required to support the corresponding fuel pathways.

Despite higher in-flight energy penalties for the LH_2 configurations, the LH_2-0.50 and LH_2-0.66 fleets outperformed all SAF pathways considered when evaluated on a WtW basis. SAF-DAC was found to be particularly energy intensive, requiring approximately 44% more energy than the lowest-performing LH_2-0.33 configuration. Near-term SAF pathways, including ATJ and FT, exhibited competitive performance relative to the best-performing LH_2 aircraft, with maximum fleet-wide WtW energy penalties of 27% and 14%, respectively; however, these fuels lack the long-term scalability and sustainability associated with P2L pathways such as SAF-DAC or green LH_2. The inclusion of IRE provided a measurable benefit to LH_2-powered aircraft, reducing total fleet-wide energy consumption by 4.4%.

This study was part of a broader effort to assess the feasibility of hydrogen-powered aircraft relative to SAF-powered alternatives across successive generations of commercial aircraft. The results indicate that improvements in fuel efficiency and LH_2 tank GI significantly reduce the relative in-flight performance penalties associated with large hydrogen fuel tanks, as demonstrated by the transition from the B737-NG to the B737-MAX operations. Future work will extend this analysis to an advanced B737-class aircraft representative of an EIS timeframe of 2035—2050. By evaluating performance over representative operating schedules, such studies aim to quantify the real-world trade-offs between aircraft design, fuel choice, infrastructure requirements, operating cost, and total energy demand. Ultimately, these analyses are intended to support data-driven policy and technology decisions that enable economically viable decarbonisation pathways while minimising pressure on renewable electricity resources.

Chapter 5

Evaluating Non-Carbon Emissions

5.1 Introduction

Given the increasing focus and regulations in relation to non-CO_2 aviation emissions, there is a growing need for modelling frameworks capable of simulating these emissions for aircraft operations at both individual-flight and fleet levels. Recent high-impact publications [12, 177] have focused on non-CO_2 climate impact models on a global scale using a top-down approach. Brazzola et al. [177] developed three definitions of climate neutrality, in which non-CO_2 emissions were either stabilised, reduced, or eliminated from 2050 onwards, and analysed the global surface temperature response due to the non-CO_2 aviation emissions resulting from each climate-neutrality scenario. Lee et al. [12] modelled the climate impact of aviation using average EI values for CO_2, NO_x, H_2O, nvPM, and SO_2 to estimate the global RF, and hence the global surface temperature response attributed to CO_2 and non-CO_2 aviation emissions.

While such approaches are well suited to global assessments, they lack the resolution required to accurately model individual flights and operational schedules. To address this limitation, Teoh et al. [16] developed a framework for simulating non-CO_2 emissions and climate impacts at the flight level, using empirical fuel-flow models driven by ADS-B trajectories, BFFM for NO_x emissions, and the T4/T2 method for nvPM prediction. These nvPM estimates were subsequently coupled with CoCiP [120] to evaluate contrail formation and associated climate impacts. More recently, Awde et al. [34] applied a similar operational framework to real-world airline flights, employing physics-based aerodynamics and propulsion models for thrust and fuel flow, while relying on empirical methods and fixed emission indices to predict non-CO_2 emissions and contrail formation. This was followed by quantification of RF and surface temperature response to determine the climate impact of specific flights, using the methods described by Proesmans and Vos [123].

The methods developed by Teoh et al. [16] and Awde et al. [34] introduced improved capabilities in modelling the climate impact of individual flights, however, these methods still rely on empirical or semi-empirical models to quantify non-CO_2 emissions. Such methods are calibrated based on experimental data for in-service engine technologies, allowing only for the simulation of pre-existing aircraft designs. The current study proposes an alternative approach, in which reduced-order physics-based models are used to simulate individual flights to predict their CO_2, NO_x, and H_2O emissions, to facilitate rapid evaluations of non-CO_2 emissions for specific flight schedules — a key enabler for proposed EU legislation. Although the increased modelling fidelity introduces additional complexity, the removal of empirical dependencies improves predictive capability and broadens applicability across both existing and future aircraft fleets. This dual capability addresses the needs of airline operators, enabling emissions estimation for compliance with MRV requirements while supporting data-driven fleet planning for future environmental objectives.

Therefore, there is a clear demand for a comprehensive physics-based methodology capable of predicting CO_2 and non-CO_2 emissions at the flight level without resorting to computationally intensive 3D simulations such as CFD. CRN models have emerged as a promising solution for bridging the gap between empirical correlations and high-fidelity CFD approaches. These models represent combustors using networks of idealised reactors, driven by combustor inlet conditions and detailed chemical reaction mechanisms, enabling prediction of combustor performance and outlet emissions [108, 109]. CRN-based models have previously been developed for NO_x, CO, and UHC prediction for CFM56-7B27 and LEAP-1A26 engines [108]; however, they have not yet been integrated within complete mission analyses or climate impact assessments. Furthermore, prior implementations did not explicitly account for the substantial combustor architecture differences between the CFM56 and LEAP engine families, which is addressed in the present study.

The overarching aim of this work is to advance operational climate impact assessment frameworks by integrating physics-based CRN combustor models for non-CO_2 emission prediction. A full day of airline operations for Europe's largest airline is simulated using a validated flight simulation framework for both B737-NG and B737-MAX aircraft. CO_2, NO_x, and H_2O emissions are predicted using CRN combustor models. Furthermore, UHC emission prediction capabilities are demonstrated as precursors to future nvPM prediction capability, and can be considered a stepping-stone towards fully physics-based contrail formation simulations. The resulting emissions are used to quantify RF and surface temperature response attributable to airline operations. CRN-based NO_x predictions are compared against conventional empirical methods to assess performance over real-world flight profiles. Finally, the climate benefits of fleet renewal are evaluated through a comparative analysis of the surface temperature response associated with B737-NG and B737-MAX operations. An overview of the modelling framework is presented in Figure 5.1, illustrating how the validated flight simulation framework discussed in Chapter 3 was connected to the non-CO_2 emission models to facilitate the climate impact analyses. Specific objectives of this study include the following:

- Develop physics-based CRN combustion models for the CFM56-7B26 and LEAP-1B27 turbofan engines, including a novel CRN architecture to represent the LEAP combustor

- Implement P3–T3, BFFM, and DLR empirical NO_x prediction models within the simulation framework

- Simulate a full day of real-world airline operations to predict CO_2, H_2O, and NO_x

emissions and quantify the associated climate impact

- Compare CRN-based and empirical NO_x emission predictions and assess their influence on climate impact estimates
- Evaluate the potential climate benefits of fleet renewal through replacement of B737-NG aircraft with B737-MAX aircraft

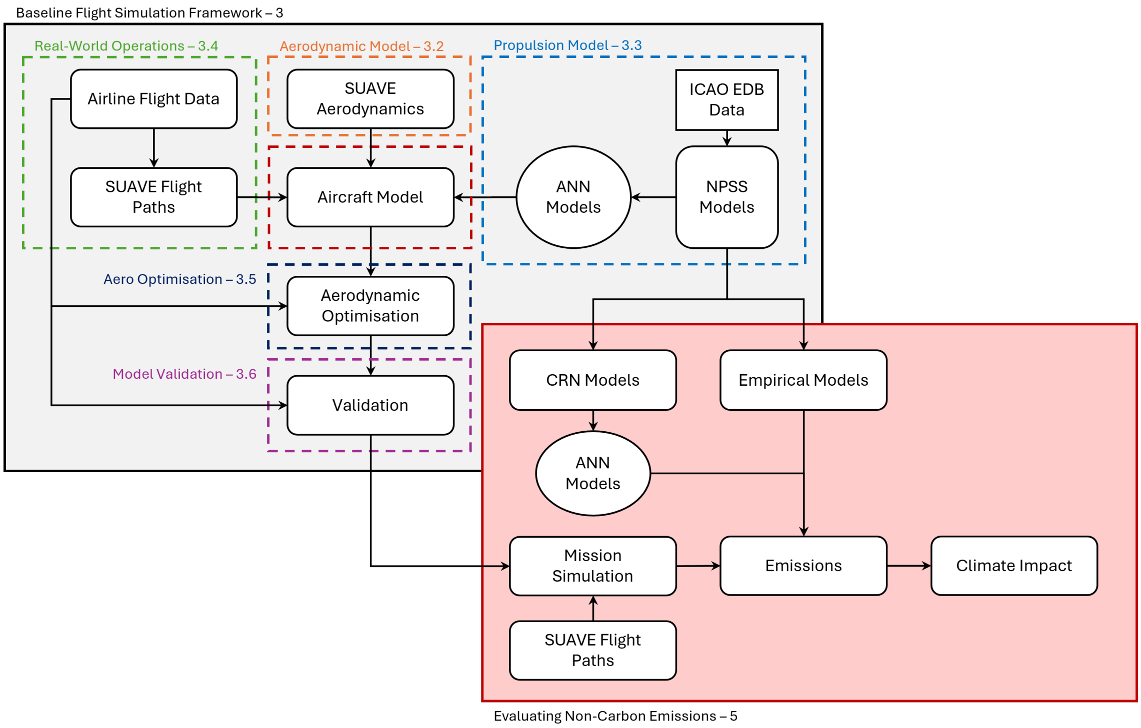

Figure 5.1: Modelling framework for evaluating non-CO_2 emissions and associated climate response of real-world operations

5.2 Chemical Reactor Network Emission Models

5.2.1 CFM56-7B26

The CRN combustor models were developed using Cantera [150], an open-source combustion modelling library available in both Python and C++. Cantera enables the construction of 0D and 1D combustion models using Perfectly Stirred Reactors (PSRs), which represent idealised reactors with spatially uniform thermochemical properties within a prescribed control volume. Although an individual PSR cannot capture axial variations of chemical composition of the working gas along the length of the combustor, a series of PSRs can be implemented to circumvent these 0D restrictions, creating a discretised pseudo-1D representation of the combustor flow. This approach was recently demonstrated by Villette et al. [108], who developed and validated a generalised three-zone CRN model to predict NO_x, CO, and UHC emissions for the CFM56-7B27, LEAP-1A26, and RR-Trent-772 turbofan engines.

The three-zone CRN architecture comprises a Primary Zone (PZ), Secondary Zone (SZ), and Dilution Zone (DZ) reactor. Peak temperatures occur within the PZ, after which the introduction of additional cooling air into the SZ and DZ progressively reduces the gas temperature. Three reservoirs – defined in Cantera as regions of infinite volume and constant thermodynamic state – were used to supply the igniter, fuel, and air streams. The igniter and fuel reservoirs were connected to the PZ reactor, while the air reservoir supplied all three zones. The DZ reactor was connected to an exhaust reservoir to impose outlet boundary conditions, ensuring appropriate pressure constraints and mass-flow balance across the network.

Ignition within the CRN was initiated using atomic hydrogen supplied as a Gaussian pulse to the fuel–air mixture in the PZ. Atomic hydrogen readily reacts with the surrounding mixture, generating sufficient heat release to initiate combustion. The igniter mass-flow rate, $\dot{m}$igniter, was defined using Equation 5.1, where $g(t)$ represents the Gaussian distribution, A_g defines the dimensionless amplitude of the mass-flow pulse, t_0 is the ignition start time, and τ is the characteristic ignition timescale [108]. Chemical reactions within the combustor were modelled using a reduced surrogate kerosene mechanism developed by Luche [156]. Fixed geometric inputs to the CRN model included the combustor cross-sectional area and length, while the operational inputs for each simulation were the combustor inlet total pressure (pt_3), inlet total temperature (T_{t3}), air mass flow rate ($\dot{m}_{\mathrm{air}}$), and FAR, all obtained from the NPSS propulsion system models described in Section 3.3.

$$\dot{m}_{\mathrm{igniter}} = \dot{m}_f \cdot g(t) \;\; \text{with} \;\; g(t) = A_g \cdot e^{-\left(\frac{t-t_0}{\tau}\right)^2} \tag{5.1}$$

A schematic of the three-zone CRN model employed by Villette et al. [108], and adopted for the CFM56-7B26 combustor in the present study, is shown in Figure 5.2(a). This figure illustrates the interconnections between the reservoirs and reactor zones, as well as the design variables used to optimise model accuracy, which are discussed in Section 5.2.3. The CRN architecture is shown alongside a schematic of the RQL combustion process implemented in the CFM56-7B26 engine in Figure 5.2(b), where ϕ denotes the equivalence ratio within each zone. This comparison highlights how the CRN structure captures the key thermochemical features of the underlying combustor design.

5.2.2 LEAP-1B27

The objective of the study by Villette et al. [108] was to develop a generalised CRN framework applicable to a wide range of modern commercial turbofan engines with minimal reliance on detailed combustor design information. The resulting model required only combustor inlet flow conditions with readily available geometric parameters such as combustor length and cross-sectional area. While this generalised approach enables broad applicability, it inherently limits the ability to capture engine-specific combustor features. This limitation was evident in the reduced accuracy of the LEAP-1A26 $\mathrm{NO_x}$ emission predictions reported by Villette et al. [108]. The LEAP-1A26 employs the more advanced TAPS-II combustor, which differs fundamentally from the conventional RQL combustor architecture used in earlier engines such as the CFM56 series [102].

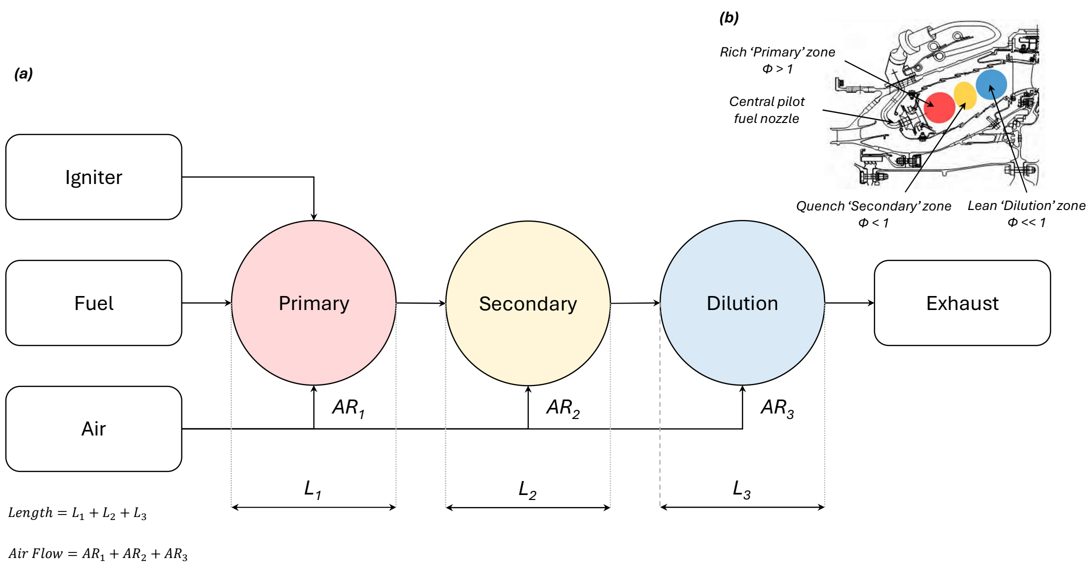

Figure 5.2: (a) CRN model architecture for CFM56-7B26 Cantera combustor model (b) RQL combustion process adapted from [102]

In contrast to the generalised scope of previous work, the present study focuses on predicting non-CO_2 emissions for two specific engine models: the CFM56-7B26 and the LEAP-1B27. To accurately represent the LEAP combustor, a new CRN architecture was developed to reflect the design principles of the TAPS-II system. Unlike RQL combustors, which rely on a single pilot fuel injection, the TAPS-II injector incorporates a central pilot surrounded by concentric main fuel nozzles. The pilot stage operates near stoichiometric conditions to ensure flame stability and is active across both low- and high-power regimes. The main stage consists of multiple radial jets discharging into a larger air swirler operating under lean conditions and is activated only at higher power settings. This staged configuration enables stable combustion with low CO and UHC emissions at low power, while achieving low NO_x emissions at high power through lean combustion in the main stage [102]. In addition, the TAPS-II combustor removes the need for large dilution holes [99], resulting in a shortened combustion chamber and an axially simplified two-zone combustion process compared to the three-zone structure characteristic of RQL combustors.

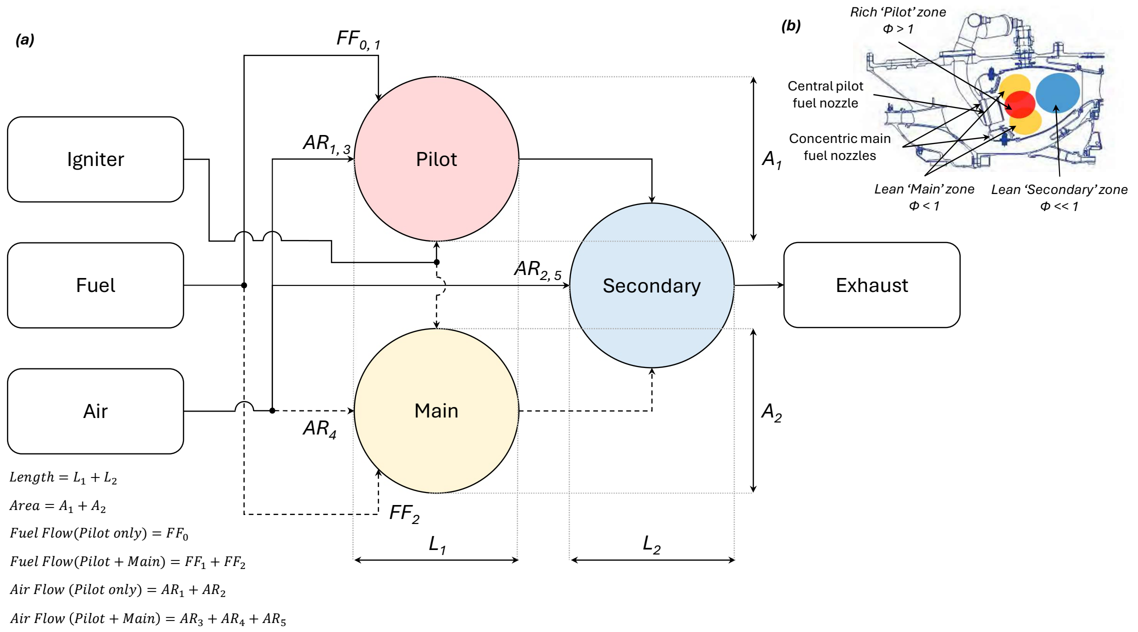

Figure 5.3: (a) CRN model architecture for LEAP-1B27 Cantera combustor model (b) TAPS-II combustion process adapted from [102]

The combustion process associated with the TAPS-II configuration is illustrated in Figure 5.3(b). The corresponding CRN architecture developed in this study is shown in Figure 5.3(a), together with the associated design variables. In the new architecture, the traditional PZ reactor is replaced by separate 'Pilot' and 'Main' reactors operating in parallel, while the DZ reactor is omitted. The main reactor, highlighted in yellow, and its associated flow connections (indicated by dashed arrows) are activated only beyond the combustor staging threshold, corresponding to throttle settings above 30% [99]. The effective cross-sectional area of the SZ is defined as the sum of the pilot and main reactor areas, $A1 + A2$.

5.2.3 Optimisation & Validation

Bayesian optimisation was applied to the CFM56-7B26 and LEAP-1B27 CRN models to identify the set of design parameters that minimised the discrepancy between predicted and measured NO_x, CO, and UHC emissions relative to the ICAO EDB values at the four SLS operating points. The optimisation objective was weighted towards NO_x emissions due to their dominant contribution to aviation climate impact. For the CFM56-7B26 CRN model, four design parameters were optimised: L_1, L_2, AR_1, and AR_2. In contrast, the LEAP-1B27 CRN model required optimisation of six parameters: L_1, A_1, AR_1, AR_3, AR_4, and FF_1. The introduction of the combustor staging threshold within the LEAP-1B27 CRN model necessitated a greater number of design variables to govern fuel-flow and air-supply distribution under high-power operating conditions, where the 'Main' reactor becomes active.

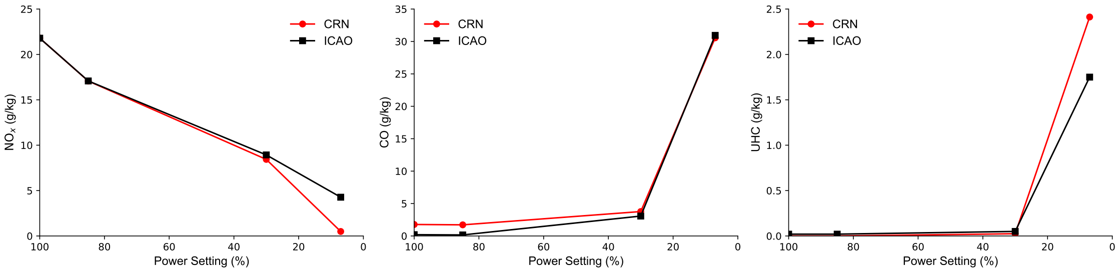

Figure 5.4: Validation of CFM56-7B26 CRN combustor model against ICAO data for (a) NO_x (b) CO (c) UHC emissions

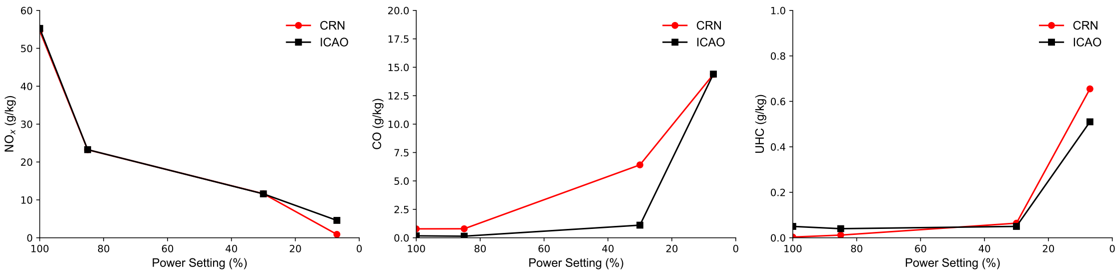

Figure 5.5: Validation of LEAP-1B27 CRN combustor model against ICAO data for (a) NO_x (b) CO (c) UHC emissions

Validation of the optimised CRN models against ICAO EDB data is presented in Figures 5.4 and 5.5 for the CFM56-7B26 and LEAP-1B27 engines, respectively. For the LEAP engine, the introduction of the revised CRN architecture resulted in notably improved emission predictions, particularly for NO_x and UHC, when compared to the generalised CRN model developed by Villette et al. [108]. This improvement demonstrates the importance of capturing engine-specific combustor features within the CRN framework.

In addition to non-CO_2 species, CO_2 and H_2O emissions were also predicted using the optimised CRN models. The predicted CO_2 emission indices ranged from 3068–3121 g/kg and 3099–3123 g/kg across the four SLS conditions for the CFM56-7B26 and LEAP-1B27 engines, respectively, while the corresponding H_2O emission indices ranged from 1314–1317 g/kg and 1315–1316 g/kg. These values differ slightly from the commonly reported emission indices for Jet A-1 fuel (3157 g/kg for CO_2 and 1260 g/kg for H_2O [123]). The discrepancy arises from two factors: differences between the surrogate kerosene fuel specification used in the combustion mechanism and that of Jet A-1, and the fact that the reported CO_2 emission index assumes complete oxidation of carbon, whereas the CRN model explicitly accounts for incomplete combustion through the formation of CO and UHC species.

5.3 ANN Surrogate Models

ANN surrogate models were developed to represent the CO_2, H_2O, and NO_x emission indices predicted by the Cantera-based CRN models, as well as the p_{t_3}, T_{t_3}, and FAR parameters extracted from the NPSS propulsion models. The latter inputs were required for implementation of the empirical P3–T3 NO_x prediction model described in Section 5.4.1. Each surrogate model was trained using a dataset comprising approximately 100,000 propulsion system operating points generated from coupled NPSS and Cantera simulations. The dataset spans the full range of altitude, Mach number, throttle setting, and ambient temperature conditions encountered within the real-world flight database.

The ANN architectures for each surrogate were optimised using the same Bayesian optimisation procedure described in Section 3.3.3. Performance metrics for the optimised models are summarised in Table 5.1, which reports the test-set MAE, RMSE, and MAPE values for each emission and thermodynamic parameter across both propulsion systems. To ensure a consistent comparison between the CRN-based and empirical NO_x prediction approaches, the same humidity correction factor applied to the empirical models (as described in Section 5.4) was also applied to the ANN-based CRN NO_x predictions.

Table 5.1: Surrogate model error metrics for thermodynamic parameters and emission predictions of the CFM56-7B26 and LEAP-1B27 propulsion systems.

Prop. System	**CFM56-7B26**			**LEAP-1B27**		
	MAE	**RMSE**	**MAPE**	**MAE**	**RMSE**	**MAPE**
T3	6.73×10^{-1}	1.02×10^{0}	0.108%	7.27×10^{-1}	1.37×10^{0}	0.102%
P3	4.23×10^{3}	7.90×10^{3}	0.480%	3.47×10^{3}	6.72×10^{3}	0.308%
FAR	3.13×10^{-5}	5.37×10^{-5}	0.167%	4.78×10^{-5}	7.16×10^{-5}	0.253%
CO_2	3.24×10^{-1}	4.68×10^{-1}	0.010%	4.65×10^{-1}	7.16×10^{-1}	0.015%
H_2O	9.31×10^{-2}	1.26×10^{-1}	0.007%	5.19×10^{-2}	8.67×10^{-2}	0.004%
NO_x	8.18×10^{-2}	1.45×10^{-1}	1.145%	1.15×10^{-1}	2.79×10^{-1}	1.967%

5.4 Empirical Emission Models

Having demonstrated the capabilities of the physics-based emission models, the following sections describe the conventional empirical methods that have been widely used for NO_x emission prediction. The comparison between novel physics-based methods and empirical methods is crucial in understanding how differences manifest in terms of non-CO_2 emission predictions at the flight and fleet level depending on the specific method used. The methods presented here expand upon the overview provided in Section 2.5.1, with particular emphasis on the implementation of the P3–T3, BFFM, and DLR empirical NO_x prediction models described by [103] and [105].

5.4.1 P3-T3

The P3–T3 method is an empirical formulation used to predict NO_x emissions as a function of the engine P_{t_3}, T_{t_3}, and FAR parameters. In the implementations described by Dubois and Paynter [103] and Awde and Stuart [34], ICAO EDB NO_x emission data are first used to define reference emission indices at SLS conditions. These reference values are subsequently corrected to account for changes in P_{t_3} and FAR at altitude, with T_{t_3} used as the interpolation variable. Although P_{t_3}, T_{t_3}, and FAR are typically proprietary engine parameters, the validated NPSS propulsion models developed in Section 3.3 provide physically consistent estimates of these quantities, enabling application of the P3–T3 method within the mission analysis framework. The formulation used to compute NO_x emission indices at altitude is given in Equation 5.2.

$$NO_{x,\,alt} = NO_{x,\,ref} \cdot \left(\frac{P_{3,\,alt}}{P_{3,\,ref}}\right)^{y} \cdot \left(\frac{FAR_{alt}}{FAR_{ref}}\right)^{z} \cdot e^{H} \tag{5.2}$$

Where subscripts *alt* and *ref* denote values at altitude and reference SLS conditions, respectively. The exponents y and z are combustor-specific and empirically derived by manufacturers [103]. Dubois and Paynter [103] report that y typically ranges from 0.2 to 0.5, with 0.5 supported by theory, while $z = 0$ for conventional rich-front-end single-annular combustors. Therefore, values of $y = 0.5$ and $z = 0$ were adopted, eliminating the FAR-based correction term. H represents the humidity correction factor. The humidity factor was calculated using Equation 5.3, where the humidity ratio ω was obtained from Equation 5.4, and the saturation vapour pressure p_{sat} from Equation 5.5. RH denotes the relative humidity, and T_{amb} is the ambient static temperature in degrees Celsius. The RH values were extracted from the MERRA-2 dataset [106].

$$H = 19 \cdot (0.00634 - \omega) \tag{5.3}$$

$$\omega = \frac{0.62197058 \cdot RH \cdot p_{sat}}{(p_{sat} \cdot 68.9473) - (RH - p_{sat})} \tag{5.4}$$

$$p_{sat} = \left(6.107 \times 10^{\frac{7.5 \cdot T_{amb}}{273.3 - T_{amb}}}\right) \cdot 68.9476 \tag{5.5}$$

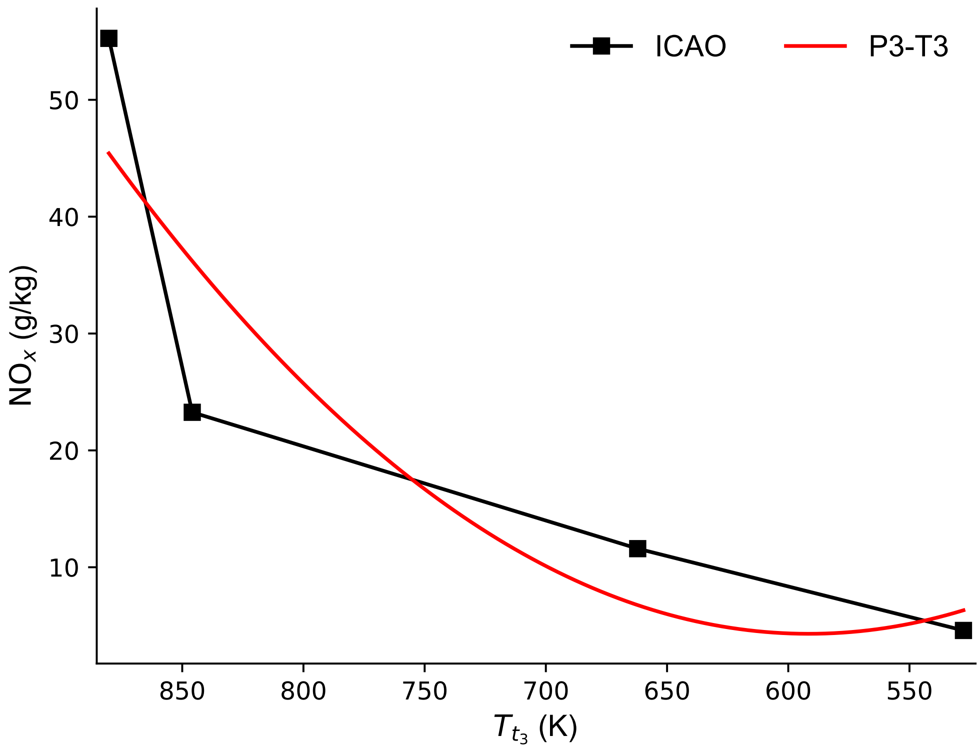

Figure 5.6: Second-degree polynomial used to generate NO_x emission index predictions as a function of T_{t_3} for the LEAP-1B27 engine

Reference NO_x emission indices, together with the corresponding P_{t_3} values, were obtained by fitting second-order polynomial curves to the ICAO EDB NO_x data as a function of T_{t_3}. The reference P_{t_3} values at SLS conditions were taken from the NPSS model predictions. An example of the polynomial fitting procedure is shown in Figure 5.6, which illustrates the fitted NO_x emission index at SLS as a function of T_{t_3} for the LEAP-1B27 engine.

5.4.2 BFFM

The BFFM is a simplified NO_x prediction approach that avoids the use of component-level thermodynamic parameters required by the P3–T3 method. Instead, it relies on readily available operational variables, including engine fuel flow, ambient pressure and temperature, and aircraft Mach number. The formulation used to predict NO_x emission indices at altitude using the BFFM is given in Equation 5.6.

$$NO_{x,alt} = NO_{x,ref} \cdot \left(\frac{\delta_{amb}}{\theta_{amb}}\right)^{0.5} \cdot e^{H} \tag{5.6}$$

Where p_{amb} denotes the ambient static pressure in Pascals and T_{amb} the ambient static temperature in Kelvin. Reference NO_x emission indices were obtained by interpolating a log–log fit of the ICAO EDB NO_x data against the corresponding fuel-flow values, also sourced from the EDB. Fuel-flow correction factors were applied at each SLS operating point to account for installation effects, following the methodology described by Awde and Stuart [34]. To account for changes in ambient conditions and flight speed, a reference fuel-flow value was calculated using Equation 5.7, where $\dot{m}_{fuel}$ represents the engine fuel flow and M the Mach number.

$$\dot{m}_{fuel,\,ref} = \dot{m}_{fuel,\,alt} \cdot \frac{\theta_{amb}^{3.8}}{\delta_{amb}} \cdot e^{0.2M^2} \tag{5.7}$$

5.4.3 DLR

The DLR NO_x prediction method follows a similar structure to the BFFM, but differs in its treatment of the underlying correlations and correction factors. In this approach, the ICAO EDB NO_x emission indices were fitted against the EDB fuel-flow values using a second-order polynomial. In addition, the pressure and temperature correction factors were formulated using total rather than static conditions. Unlike the BFFM, no fuel-flow correction factors were applied to account for installation effects. The resulting expressions used to compute the NO_x emission index and the corresponding reference fuel flow are given in Equations 5.8 and 5.9, respectively.

$$NO_{x,\,alt} = NO_{x,\,ref} \cdot \delta_{amb,\,t}^{0.4} \cdot \theta_{amb,\,t}^{3} \cdot e^{H} \tag{5.8}$$

$$\dot{m}_{fuel,\,ref} = \frac{\dot{m}_{fuel,\,alt}}{\delta_{amb,\,t} \cdot \sqrt{\theta_{amb,\,t}}} \tag{5.9}$$

5.5 Climate Impact Analysis

The climate impact of the simulated day of airline operations was assessed by quantifying the global mean surface temperature response induced by CO_2, NO_x, and H_2O emissions from the 2408 flights analysed. This section describes the methodology used to compute the RF of each species and the resulting temperature response, following the modelling framework proposed by Proesmans and Vos [123]. For completeness, selected equations previously introduced in Section 2.6 are reproduced here.

5.5.1 Average Temperature Response

To quantify climate impact, the 100-year average temperature response metric, ATR_{100}, was employed. ATR_{100} represents the mean global surface temperature change over a 100-year period resulting from radiative forcing due to emissions. This metric is well suited for assessing global warming impacts, as it directly links aviation emissions to surface temperature change while reducing sensitivity to the choice of time horizon. In addition, the 100-year averaging period provides a balanced representation of both long-lived species (e.g., CO_2) and short-lived species (e.g., H_2O). The formulation used to compute ATR_{100} is given in Equation 5.10.

$$ATR_{100} = \frac{1}{100} \int_{0}^{100} \Delta T(t) \cdot dt \tag{5.10}$$

The surface temperature response, $\Delta T(t)$, was computed by convolving the time-varying radiative forcing with a linear temperature impulse response function, $G_T(t)$, which captures the delayed thermal response of the climate system. This convolution yields the annual mean surface temperature change and is expressed in Equation 5.11.

$$\Delta T(t) = \int_{t_0}^{t} G_T(t - t') \cdot RF^*(t') \cdot dt' \quad \text{with} \quad G_T(t) = \frac{2.246}{36.8} \cdot e^{-t/36.8} \tag{5.11}$$

The normalised radiative forcing, $RF^*(t')$, represents the total climate forcing in a given year, scaled relative to the RF associated with a doubling of atmospheric CO_2 concentration (3.7 W/m^2). As defined in Equation 5.12, the total normalised forcing is obtained by summing the contributions from all species considered in this study (CO_2, NO_x, and H_2O). Each contribution is weighted by the species-specific efficacy, Eff_i, which represents the relative climate sensitivity, λ_i, of species i with respect to that of CO_2. The climate sensitivities and efficacies adopted for each species are summarised in Table 5.2.

$$RF^*(t) = \sum_{i}^{\text{all species}} RF_i^*(t) = \sum_{i}^{\text{all species}} \left(Eff_i \cdot \frac{RF_i(t)}{3.7} \right) \tag{5.12}$$

Table 5.2: Climate sensitivities λ_i and efficacies Eff_i of each species used for RF^* calculation

Species	CO_2	O_3	CH_4	H_2O
λ_i	0.73	1.00	0.86	0.83
Eff_i	1.00	1.37	1.18	1.14

5.5.2 Radiative Forcing Models

Carbon Dioxide

CO_2 emissions were predicted using the CRN combustor models, implemented via ANN surrogate representations. The resulting time series of CO_2 emissions was used to compute changes in atmospheric CO_2 concentration through a multi-exponential impulse response function, as defined in Equation 5.13.

$$\Delta \chi_{CO_2} = \int_{t_0}^{t} G_{\chi_{CO_2}}(t - t') \cdot E_{CO_2}(t') \cdot dt' \quad \text{with} \quad G_{\chi_{CO_2}}(t) = \sum_{j=0}^{5} \alpha_j \cdot e^{-t/\tau_j} \tag{5.13}$$

Where $E_{CO_2}(t')$ denotes the total CO_2 mass emitted in year t', while α_i and τ_i are the coefficients defined by Sausen and Schumann [122], representing the fractional contribution and characteristic lifetime of each response mode, respectively. These coefficients, which define the impulse response function $G_{\chi_{CO_2}}$, are listed in Table 5.3. The resulting change in atmospheric CO_2 concentration was then used to calculate the corresponding normalised radiative forcing using Equation 5.14, where $\chi_{CO_{2,0}}$ denotes the pre-industrial atmospheric CO_2 concentration, assumed to be 380 ppmv [123].

$$RF^*_{CO_2}(t) = \frac{1}{\ln 2} \cdot \ln \frac{\chi_{CO_{2,0}} + \Delta\chi_{CO_2}}{\chi_{CO_{2,0}}} \tag{5.14}$$

Table 5.3: Coefficients applied to the CO_2 impulse response function $G_{\chi_{CO_2}}$

i	**1**	**2**	**3**	**4**	**5**
α_j	0.0670	0.1135	0.1520	0.0970	0.0410
τ_j	∞	313.8	79.8	18.8	1.7

Nitrogen Oxides

Although NO_x is not itself a greenhouse gas, it influences the climate through a series of indirect effects. These include the formation of short-lived ozone (O_{3S}), which contributes to atmospheric warming, as well as depletion of long-lived ozone (O_{3L}) and methane (CH_4), both of which induce cooling effects. The combined impact of these mechanisms results in a net warming contribution from NO_x emissions. In this study, NO_x emissions were predicted at each discretised point along every flight trajectory using both the physics-based CRN combustor models (via ANN surrogates) and the P3–T3, BFFM, and DLR empirical methods. The RF associated with each NO_x-driven pathway was calculated using species-specific response functions and forcing factors that account for the altitude of emission. Short-lived effects are described by Equation 5.15, while long-lived effects are represented by Equation 5.16.

$$RF_{O_{3S}}(t,h) = s_{O_{3S}}(h) \cdot \left(\frac{RF_{ref}}{E_{ref}}\right)_{O_{3S}} \cdot E_{NO_x}(t) \tag{5.15}$$

$$\begin{gathered} RF_i(t,h) = s_i(h) \int_{t_0}^{t} G_i(t-t') \cdot E_{NO_x}(t') \cdot dt' \\ \text{with} \quad G_i(t) = A_i \cdot e^{-t/\tau} \quad \text{for } i = CH_4,\, O_{3L} \end{gathered} \tag{5.16}$$

Where $E_{NO_x}(t')$ denotes the total NO_x mass emitted in year t', $s(h)$ is an altitude-dependent forcing factor derived from the work of Dallara [130] and previously illustrated in Figure 2.22, and $(RF_{ref}/E_{ref})O3S$ represents the radiative forcing per unit NO_x emitted for short-lived ozone, taken as 1.01×10^{-11} $(W/m^2)/kg$. For the long-lived components, A_i denotes the radiative efficiency per unit NO_x emitted, with values of -1.21×10^{-13} $(W/m^2)/kg$ for long-lived ozone and -5.16×10^{-13} $(W/m^2)/kg$ for methane. The associated perturbation lifetime, τ, was set to 12 years [123].

Water Vapour

Water vapour emissions contribute directly to global warming and indirectly through contrail formation. While contrail-related impacts are not considered in the present study due to the absence of physics-based methods for incorporating engine nvPM effects, direct radiative forcing from water vapour emissions is included. H_2O emissions were predicted using the CRN combustor models implemented via ANN surrogates. Owing to the short atmospheric lifetime of water vapour, its radiative forcing was treated as an instantaneous effect, applied only in the year of emission.

$$RF_{H_2O}(t) = \left(\frac{RF_{ref}}{E_{ref}}\right)_{H_2O} \cdot E_{H_2O}(t) \tag{5.17}$$

Where $E_{H_2O}(t')$ denotes the total H_2O mass emitted in year t', and $(RF_{ref}/E_{ref})_{H_2O}$ was taken as 7.43×10^{-15} $(\mathrm{W/m^2})/\mathrm{kg}$. An altitude-dependent forcing factor was not applied to water vapour emissions [123], as the net climate impact within the troposphere and lower stratosphere is relatively small compared to that of CO_2 and NO_x emissions [130].

5.6 Case-Study Setup

5.6.1 Aircraft Operations

The operational schedule used for the case-study analysis comprised the 2408 B737-NG flights contained within the full flight database shown in Figure 3.5. Due to the limited availability of operational data for the B737-MAX, the same set of 2408 flights was also simulated using the B737-MAX aircraft model with an adjusted TOW to account for the increased OEW of the B737-MAX aircraft. This approach enabled a consistent, one-to-one comparison of aircraft performance across a full day of airline operations, facilitating a direct assessment of the potential benefits associated with fleet renewal.

5.7 Results & Discussion

This section presents the results and discussion associated with the evaluation of the operational schedule defined in Section 5.6.1, using the modelling framework outlined in Figure 5.1. The discussion is structured around the three primary research objectives of the study. First, the surface temperature response and ATR_{100} is examined for the B737-NG and B737-MAX operating schedules using the CRN-based emission models. This is followed by a comparative assessment of CRN-based and empirical NO_x prediction methods for each aircraft type. Finally, the implications of fleet renewal on the overall climate impact of the operating schedule are evaluated.

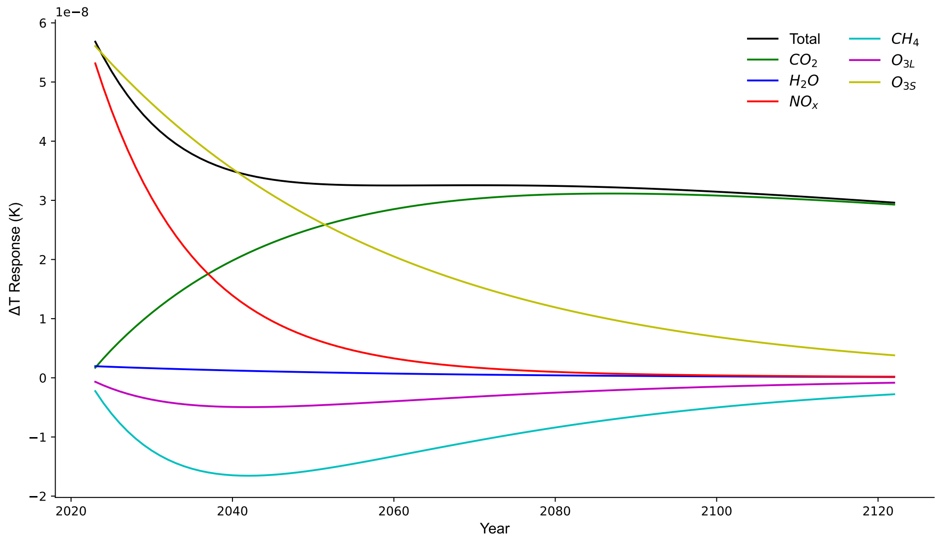

Figure 5.7: Surface temperature response results over 100-year period for the B737-NG flight schedule

5.7.1 Climate Impact

B737-NG

Figure 5.7 shows the surface temperature response over a 100-year period attributable to CO_2 and non-CO_2 emissions for the 2408 flights simulated using the B737-NG aircraft model. The total temperature response is dominated by NO_x emissions during the first decade following the emission event, driven primarily by the warming effect of short-lived ozone (O_{3S}). This contribution peaks in the year of emission (2023) and decreases steadily thereafter. The initial warming from O_{3S} is partially offset by the cooling effects associated with methane depletion (CH_4) and long-lived ozone (O_{3L}), which peak around 2040 before gradually decreasing over the remainder of the 100-year period. The equilibrium point between the warming contributions of NO_x and CO_2, which is defined as the time at which their respective temperature responses are equal, occurs in 2037 – approximately 14 years after the emission event. Beyond approximately 2080, the contribution of NO_x to the total temperature response becomes negligible.

In contrast, CO_2 emissions exhibit a substantially longer atmospheric lifetime and can influence global temperatures over centuries to millennia [35]. This behaviour is evident in Figure 5.7, where the CO_2-induced temperature response peaks around 2090 and declines only gradually thereafter, remaining significant at the end of the 100-year analysis period. Although H_2O emissions were included to demonstrate the capability of the physics-based emission modelling framework – particularly in the context of future contrail-related analyses – it is evident that the direct climate impact of water vapour emissions is minor relative to that of CO_2 and NO_x.

The ATR_{100} values for each emission species are summarised in Table 5.4, providing a balanced metric for comparing the relative warming and cooling contributions over the 100-

year period. The total ATR_{100} across all species for the 2408-flight schedule is 3.40×10^{-8} K, corresponding to an average ATR_{100} of 1.41×10^{-11} K per flight. CO_2 accounts for the majority of the total ATR_{100}, contributing 76.7%, followed by NO_x at 21.3%. H_2O emissions contribute the remaining 2% of the total ATR_{100}.

Table 5.4: Average Temperature Response results for each species analysed for the B737-NG flight schedule

Species	**Total**	**CO_2**	**H_2O**	**NO_x**	**CH_4**	**O_{3L}**	**O_{3S}**
ATR_{100} (K)	3.4×10^{-8}	2.6×10^{-8}	6.8×10^{-10}	7.2×10^{-9}	-9.5×10^{-9}	-2.8×10^{-9}	2.0×10^{-8}

B737-MAX

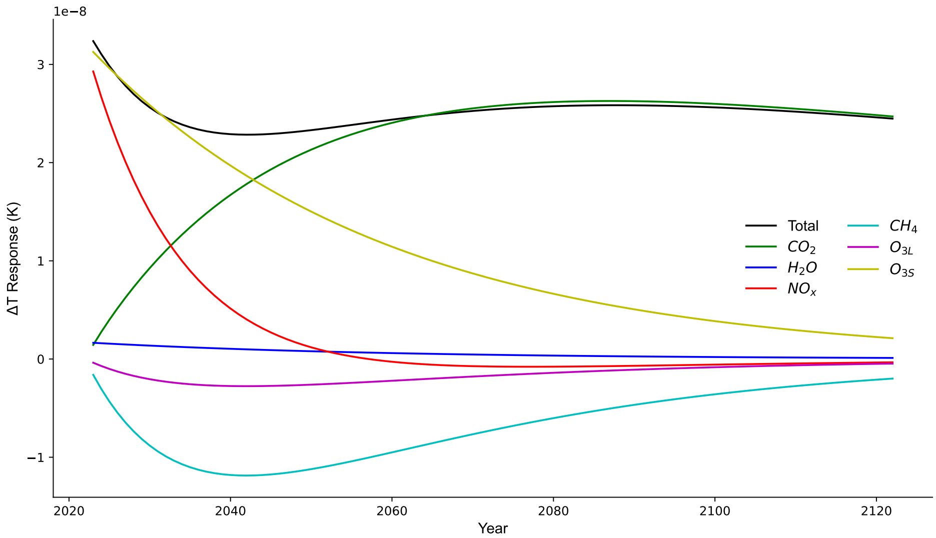

Figure 5.8: Surface temperature response results over 100-year period for the B737-MAX flight schedule

Figure 5.8 presents the surface temperature response over the same 100-year period as the preceding analysis, with all 2408 flights simulated using the B737-MAX aircraft model. Broadly similar trends are observed relative to the B737-NG case, including the dominance of NO_x-induced warming during the first 10–15 years following the emission event, after which the longer-lived CO_2-driven warming becomes the primary contributor to the total temperature response. However, clear differences emerge in the magnitude of the response, particularly before 2040, which are mainly attributable to a substantial reduction in NO_x-related warming. The reduced NO_x contribution for the B737-MAX aircraft arises from the adoption of the TAPS-II combustor, which produced significantly lower NO_x emissions under typical cruise conditions, as discussed in Section 5.7.2. As a result, CO_2 accounts for a proportionally larger share of the total temperature response across the 100-year period analysed when compared with the B737-NG aircraft, despite lower absolute emissions.

The ATR_{100} results for the 2408 B737-MAX flights are summarised in Table 5.5. The total ATR_{100} across all species is 2.51×10^{-8} K, corresponding to an average ATR_{100}

of 1.04×10^{-11} K per flight. CO_2 constitutes the dominant contribution, accounting for 87.6% of the total ATR_{100}. In contrast, NO_x contributes 10.1%, reflecting the reduced emission levels associated with the B737-MAX combustor design, while H_2O accounts for the remaining 2.3%.

Table 5.5: Average Temperature Response results for each species analysed for the B737-MAX flight schedule

Species	**Total**	**CO_2**	**H_2O**	**NO_x**	**CH_4**	**O_{3L}**	**O_{3S}**
ATR_{100} (K)	2.5×10^{-8}	2.2×10^{-8}	5.8×10^{-10}	2.5×10^{-9}	-6.8×10^{-9}	-1.6×10^{-9}	1.1×10^{-8}

The results demonstrate that non-CO_2 emissions not only contribute significantly to total climate impact, but also alter the relative importance of emission species across aircraft technologies. The transition from B737-NG to B737-MAX leads to a substantial reduction in NO_x-related warming, shifting the overall climate impact towards a greater dominance of long-lived CO_2 effects. This highlights how advancements in combustor and propulsion system design can modify both the magnitude and temporal characteristics of aviation-induced warming. Therefore, meaningful evaluation of aircraft technologies requires an integrated consideration of both CO_2 and non-CO_2 effects to fully capture these shifts in emissions behaviour. Such evaluations enable targeted mitigation strategies aligned with the temperature limits of the Paris Agreement.

5.7.2 Comparative Analysis of NO_x Prediction Models

This section quantifies the sensitivity of the predicted temperature response to the choice of NO_x emission modelling approach, comparing the physics-based CRN combustor model with the empirical P3–T3, BFFM, and DLR methods for both the B737-NG and B737-MAX aircraft.

B737-NG

Figure 5.9 illustrates the difference in surface temperature response over the 100-year analysis period for the 2408 B737-NG flights when NO_x emissions are predicted using the CRN model instead of the empirical methods. For example, the change in temperature response, ΔT, between two modelling approaches was calculated using Equation 5.18. The three empirical methods showed close agreement for the B737-NG aircraft, with only a modest increase in NO_x emissions predicted by the DLR method. In contrast, the CRN model predicted substantially higher NO_x emissions for the same flight schedule, resulting in a pronounced increase in the temperature response relative to all empirical approaches.

$$\text{Change in } \Delta T \text{ Response}_{CRN-P3T3} = \Delta T_{CRN} - \Delta T_{P3T3} \tag{5.18}$$

The peak difference in temperature response occurs in the year of emission and ranges from $2.57\text{–}2.77 \times 10^{-8}$ K for the CRN model relative to the empirical methods. This corresponds to a 48–52% increase in the net NO_x-induced temperature response and accounts for 45–49% of the total temperature response in the year of emission. Over the full 100-year

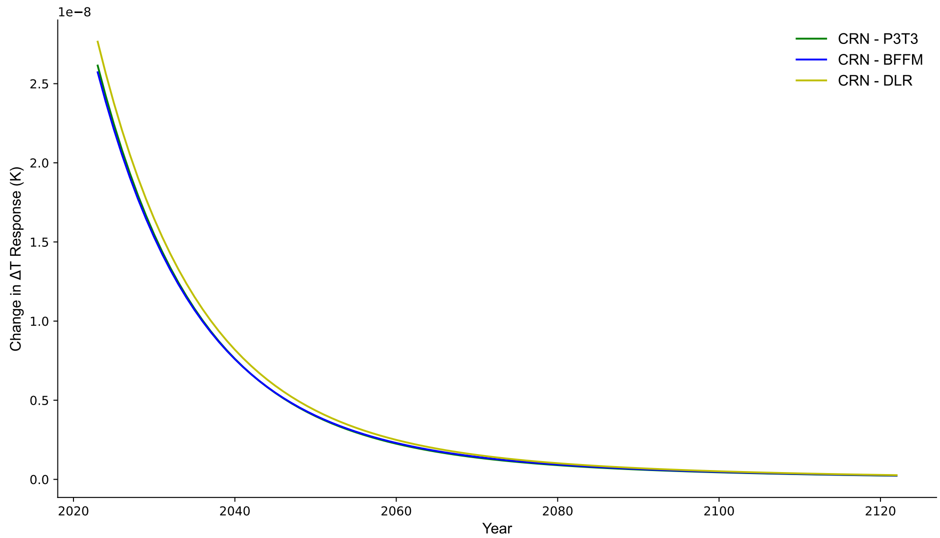

Figure 5.9: Change in surface temperature response for the CRN model compared to empirical models for the B737-NG flight schedule

period, the total ATR_{100} associated with the CRN model increased by $4.00–4.31 \times 10^{-9}$ K compared to the empirical approaches, representing a 13.4–14.6% increase in total ATR_{100}.

Such large discrepancies in predicted temperature response have important implications for climate impact assessments and warrant detailed investigation. Examination of individual flight profiles revealed that the primary source of divergence arises from higher NO_x emissions predicted by the CRN model during cruise. To explore this behaviour, NO_x emission indices were analysed across the full throttle range and compared against the ICAO EDB reference values.

Figure 5.10 compares the CRN-predicted NO_x EI values with those obtained from the empirical methods and the ICAO EDB data. As discussed in Section 5.4, the empirical methods rely on curve fits to the four EDB operating points, with additional corrections applied to account for changes in altitude, temperature, pressure, and flight speed. In contrast, the CRN results in Figure 5.10 demonstrate that NO_x EI does not follow the near-linear trend implied by the EDB data. This deviation is most pronounced at throttle settings between 40–80% of maximum power, corresponding to the typical cruise operating regime.

Within this region, the CRN model predicts an initial increase in NO_x EI, reaching a peak value of approximately 36 g/kg at a throttle setting near 57%. This behaviour arises from a combination of combustion physics and the mathematical definition of the emission index in Equation 5.19. As illustrated on the secondary axis of Figure 5.10, the PZ temperature initially increases as throttle is reduced, reaching stoichiometric conditions ($\phi = 1$) at approximately 77% throttle. This leads to maximum flame temperatures and elevated NO_x formation rates [102, 99]. Although residence time decreases due to reduced mixture density, this reduction is insufficient to offset the increased NO_x formation. Simultaneously, the reduction in combustor fuel flow causes the NO_x EI to increase, as the

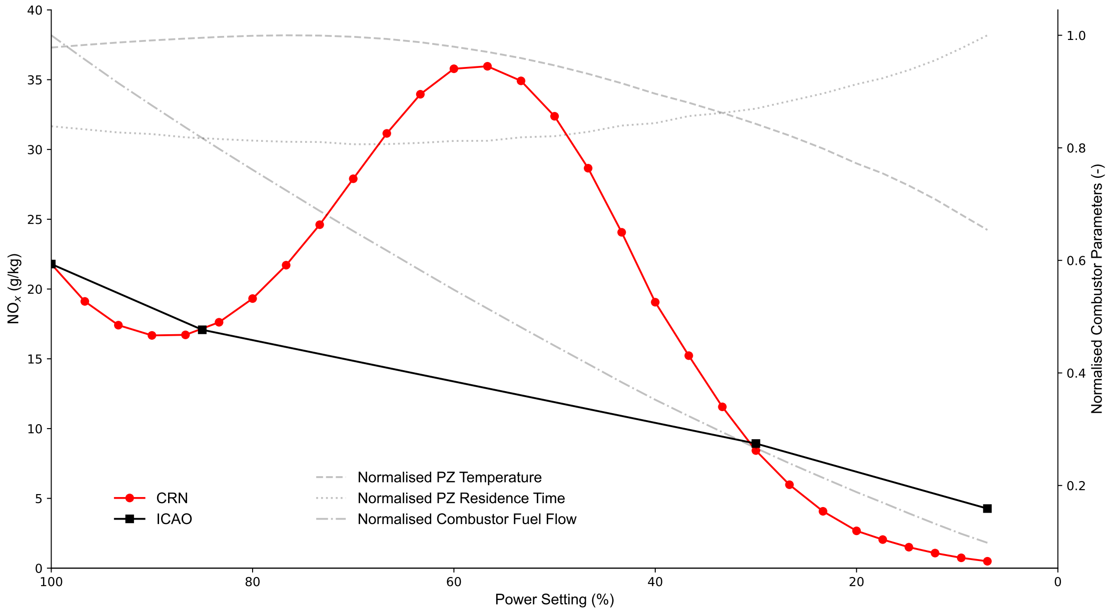

Figure 5.10: CRN NO_x predictions over full operating range compared to the four ICAO EDB values for the CFM56-7B26 engine

mass of NO_x formed remains high while the denominator of the EI definition decreases.

$$EI_{NO_x} = \frac{\dot{m}_{NO_x}}{\dot{m}_{fuel}} \tag{5.19}$$

The peak NO_x EI does not coincide with the absolute maximum combustor temperature; however, temperatures remain sufficiently high to sustain strong thermal NO formation rates while fuel flow has decreased substantially. Maximum thermal NO formation typically occurs at equivalence ratios slightly below stoichiometric conditions, due to elevated temperatures combined with increased oxygen availability [101], a trend captured by the CRN model. As the throttle is reduced further and the PZ mixture becomes leaner, flame temperatures fall below the threshold required for significant NO_x production, and the EI subsequently decreases.

As a result, the CRN model predicts significantly higher cruise NO_x emissions than the empirical methods, which are unable to capture this non-linear behaviour due to their reliance on limited interpolation data. This leads to substantial differences in the NO_x-related temperature response for the B737-NG aircraft. It is noteworthy that ICAO has recently acknowledged the large uncertainty in NO_x EI values within the cruise operating regime and has proposed the inclusion of an additional EDB measurement point at a 57.5% power setting [107]. Such data would provide critical validation for physics-based CRN models such as the one developed in this study.

B737-MAX

Figure 5.11 presents the change in surface temperature response for all 2408 B737-MAX flights when NO_x emissions are predicted using the CRN model instead of the empirical methods. In contrast to the B737-NG results, the CRN model predicted lower NO_x emis-

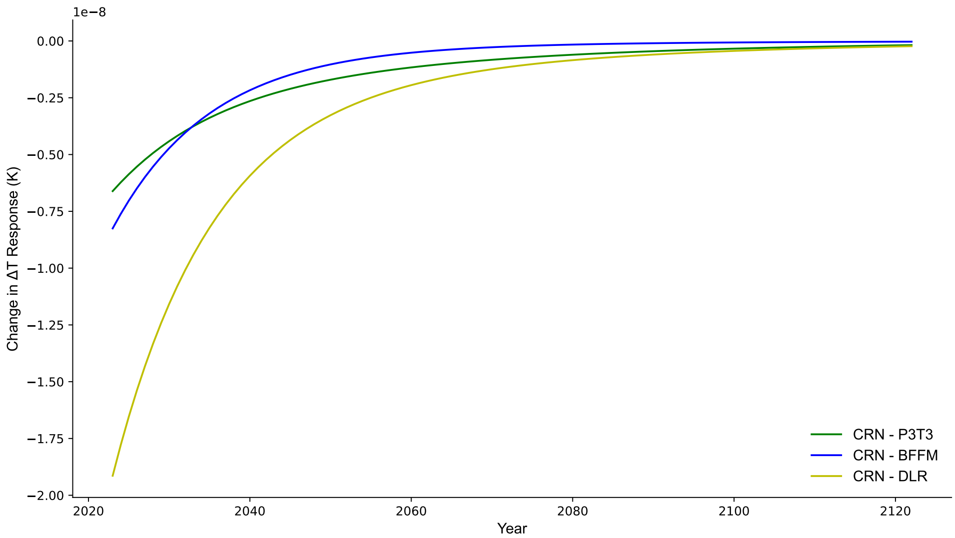

Figure 5.11: Change in surface temperature response for the CRN model compared to empirical models for the B737-MAX flight schedule

sions for the B737-MAX aircraft, leading to a reduced temperature response relative to all three empirical approaches. The P3–T3 and BFFM methods yielded close agreement, with peak differences in temperature response relative to the CRN model ranging from -0.66×10^{-8} to -0.83×10^{-8} K, respectively. These differences correspond to an 18–22% reduction in the net NO_x-induced temperature response and a 17–20% reduction in the total temperature response in the year of emission when using the CRN model.

The distinct shapes of the temperature response curves, highlighted by the intersection of the P3–T3 and BFFM curves in Figure 5.11, arise from differences in the temporal and spatial distribution of NO_x emissions predicted by each method. These differences alter the relative weighting of short-lived ozone formation versus long-lived methane and ozone depletion through altitude-dependent forcing factors, influencing the magnitude and evolution of the NO_x-related temperature response over the 100-year period.

The DLR method predicted substantially higher temperature responses than all other models, with the peak difference relative to the CRN model reaching -1.91×10^{-8} K. This corresponds to a 39% reduction in the net NO_x temperature response and a 37% reduction in the total temperature response in the year of emission when adopting the CRN model. The elevated NO_x emissions predicted by the DLR method are primarily due to higher reference fuel-flow values during cruise, calculated using Equation 5.9, which frequently resulted in approximately double the NO_x emissions compared to the P3–T3 and BFFM methods. This sensitivity is exacerbated by the steep increase in NO_x EI at high power settings for the LEAP engine, as shown by the ICAO NO_x curve in Figure 5.12. Although the DLR method also produced higher reference fuel-flow values for the B737-NG aircraft, the near-linear NO_x EI trend for the CFM56 engine resulted in comparatively smaller discrepancies. Over the full 100-year period, the total ATR_{100} associated with the CRN model is reduced by 1.13×10^{-9} to 3.14×10^{-9} K relative to the empirical methods, corresponding to a 4.3–11.1% decrease in total ATR_{100}.

To further investigate these differences, NO_x EI values were analysed across the full throttle range and compared with the ICAO EDB reference data. Figure 5.12 shows the CRN-predicted NO_x EI values for the B737-MAX aircraft alongside the EDB data. As observed for the CFM56 engine, the four EDB points are insufficient to characterise the non-linear behaviour of the combustor between the reported power settings. For the LEAP engine, this limitation is further compounded by the staged nature of the TAPS-II combustor.

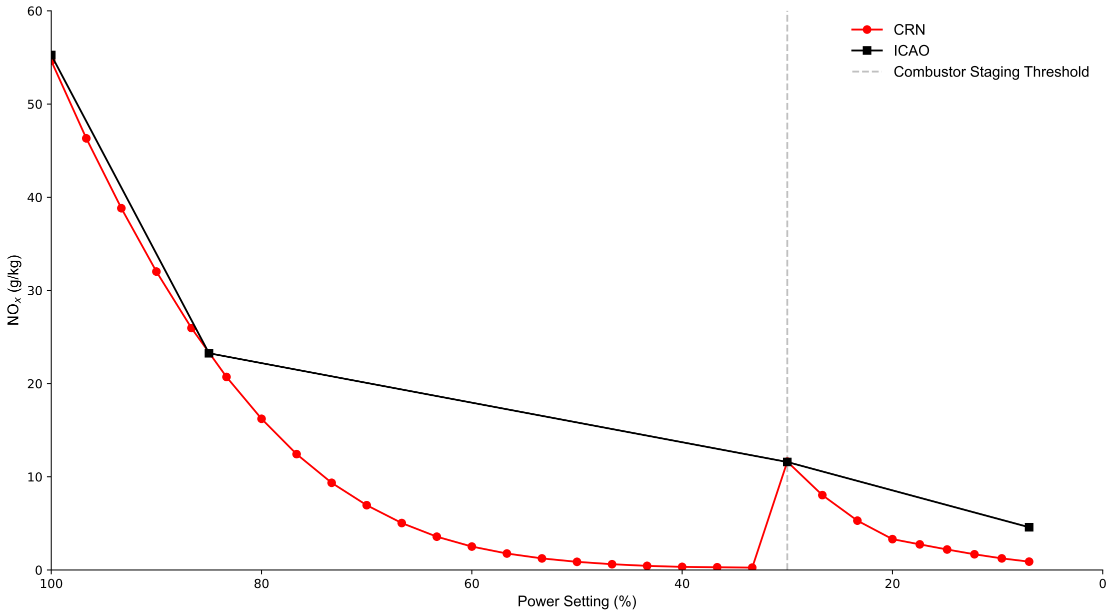

Figure 5.12: CRN NO_x predictions over full operating range compared to the four ICAO EDB values for the LEAP-1B27 engine

As discussed in Section 5.2.2, the TAPS-II combustor operates in two distinct modes: a pilot-only mode at low power and a combined pilot–main mode beyond a staging threshold of approximately 30% throttle. This transition is clearly evident in Figure 5.12, where a step change in NO_x formation occurs as the main fuel injector becomes active. Analysis of the CRN reactor temperatures indicates that activation of the main stage leads to a reduction in peak flame temperature and a more uniform temperature distribution across the combustor, resulting in substantially lower NO_x formation rates. This behaviour is consistent with experimental observations of the TAPS-II combustor reported in the literature [102, 99]. Further confidence in the CRN predictions for the LEAP-1B27 engine is provided by the close qualitative agreement with the NO_x emission trends reported by Foust et al. [102], where a similar characteristic EI profile to that shown in Figure 5.12 was observed.

Building on these observed differences between aircraft technologies, the comparison of CRN and empirical NO_x prediction methods demonstrates that accurately capturing such shifts in emissions behaviour remains a significant challenge. The results show that simplified empirical approaches can introduce substantial and configuration-dependent errors, with the potential to either under-predict or over-predict NO_x-related climate impacts depending on the engine and operating conditions. This inconsistency limits their ability to reliably distinguish between technologies with differing combustor characteristics. As a result, higher-fidelity modelling approaches are required to ensure that variations in non-CO_2 emissions are represented consistently, particularly in the context of comparative environmental assessments.

5.7.3 Impact of Fleet Renewal on Climate Response

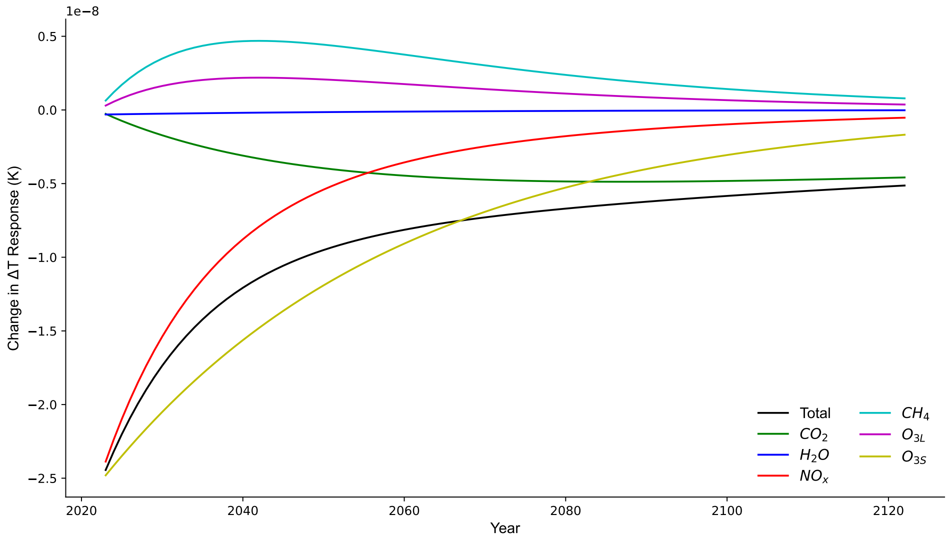

Figure 5.13: Change in temperature response for B737-MAX flight schedule relative to B737-NG schedule using CRN models

The impact of fleet renewal was quantified by evaluating the difference in surface temperature response over the 100-year analysis period when the previously defined schedule of 2408 flights was operated using B737-MAX aircraft instead of B737-NG aircraft, as shown in Figure 5.13. A substantial reduction in NO_x-related climate impacts was observed, with the peak difference in temperature response reaching -2.39×10^{-8} K in the year of emission. This corresponds to a 55% reduction in the peak net NO_x-induced warming and a 58% reduction in the peak total temperature response relative to the B737-NG schedule.

Over longer timescales, reductions in CO_2-related warming become increasingly influential. At the end of the 100-year period, the total temperature response was reduced by -0.51×10^{-8} K for the single day of airline operations, primarily due to lower CO_2 emissions associated with the improved fuel efficiency of the B737-MAX aircraft. This corresponds to a 17.2% reduction in the total temperature response at the end of the analysis period.

Changes in ATR_{100} values are summarised in Table 5.6. The most pronounced reduction was associated with NO_x, for which the ATR_{100} decreased by 65.0%, reflecting the substantially lower NO_x emissions produced by the B737-MAX aircraft. The CO_2-related ATR_{100} was reduced by 15.7%, consistent with expected reductions in fuel burn relative to the B737-NG aircraft. When considering the combined effects of CO_2, H_2O, and NO_x, the total ATR_{100} was reduced by 26.2%. These results highlight that fleet renewal with more advanced technologies could have a significant beneficial effect on aviation's climate impact over a 100-year period. Furthermore, the temperature response in the near-term can be substantially reduced with the introduction of B737-MAX aircraft due to the larger NO_x-related ATR reductions, which dominate global warming effects within the first 15 years of the emission event.

Table 5.6: Change in Average Temperature Response values for B737-MAX schedule relative to B737-NG schedule

Species	**Total**	$\mathbf{CO_2}$	$\mathbf{H_2O}$	$\mathbf{NO_x}$	$\mathbf{CH_4}$	$\mathbf{O_{3L}}$	$\mathbf{O_{3S}}$
$\mathbf{ATR_{100}}$ ($\times 10^{-9}$ **K**)	-8.9	-4.1	-0.11	-4.7	2.7	1.3	-8.6
$\mathbf{ATR_{100}}$ (%)	-26.2	-15.7	-15.7	-65.0	28.3	44.2	44.2

When applied to fleet-level analysis, these findings demonstrate that the climate benefits of fleet renewal are strongly influenced by reductions in non-CO_2 emissions, in addition to improvements in fuel efficiency. In particular, decreases in NO_x emissions lead to disproportionately large reductions in near-term warming, while CO_2 reductions dominated long-term climate outcomes. However, the magnitude of these benefits was highly sensitive to the emission modelling approach used, with empirical methods potentially misrepresenting the true impact of fleet renewal strategies. This has important implications for the evaluation of aviation sustainability measures within emerging non-CO_2 regulatory frameworks, where robust and consistent quantification of both short- and long-term climate effects is essential for informed decision-making.

5.8 Key Findings & Interpretation

This study demonstrates the importance of high-fidelity, physics-based approaches for quantifying the climate impact of non-CO_2 emissions from real-world aircraft operations. By applying a validated flight simulation framework to airline operations, key differences between conventional empirical methods and physics-based CRN models were identified, with significant implications for climate impact assessment and environmental decision-making.

A comparative analysis of the CRN and empirical NO_x prediction models found substantial differences in surface temperature response for both B737-NG and B737-MAX aircraft. For the B737-NG, the CRN model predicted higher NO_x emissions, resulting in a 13.4–14.6% increase in total ATR over a 100-year period. In contrast, the CRN model predicted lower NO_x emissions for the B737-MAX aircraft, corresponding to ATR reductions of 4.3–11.1%. These discrepancies were primarily driven by divergence in NO_x emission indices during cruise conditions. These findings demonstrate that methodological choice can significantly influence the predicted climate impact of aircraft operations, with direct consequences for the robustness of sustainability assessments and emissions reporting frameworks.

A comparative analysis of the B737-NG and B737-MAX climate response over an identical flight schedule found significant climate-related benefits for fleet renewal when using the CRN model predictions. Introduction of B737-MAX aircraft was found to reduce the total ATR by 26.2% over a 100-year period, whereas the NO_x-related ATR was reduced by 65.0%. These results highlight fleet renewal as an effective strategy for reducing aviation's climate impact, particularly when assessed using higher-fidelity emissions modelling approaches.

This study has important implications for emerging emissions monitoring and regulatory frameworks. New MRV regulations introduced by the EU intend to include non-CO_2 emissions within the ETS framework, where it is intended that the NEATS tool will be used to predict emissions using conventional empirical methods. For emissions-based regulatory mechanisms to be effective, accurate emission prediction methodologies are essential. The divergence between the physics-based methods developed in this study against the empirical methods highlights potential concerns with the proposed NEATS methodology. This is particularly relevant when considering the differences in the CRN and empirical models when applied to the B737-NG and B737-MAX aircraft, as the empirical models may significantly under-predict the climate related benefits associated with fleet renewal. From a policy perspective, incorporating more accurate NO_x prediction methods could further incentivise fleet renewal strategies for airlines through reduction of emission-related penalties, further reducing the climate impact of the aviation industry. However, further validation is required, particularly under cruise conditions where uncertainty remains high. This highlights the need to integrate higher-fidelity modelling approaches into sustainability-focused regulatory tools to ensure that mitigation strategies are both accurately assessed and effectively incentivised.

The framework also provides a foundation for extending the analysis to consider contrail formation and fuel-specific climate impacts, enabled through CRN-based predictions of UHC and H_2O emissions. Furthermore, implementation of detailed fuel specifications within CRN models facilitates thorough analysis of low aromatic and/or low sulphur fuels, which influence contrail formation [110]. This capability is important for supporting future assessments of strategies aimed at reducing the overall climate impact of aviation in the context of anticipated sector growth and introduction of SAF-related regulations, such as ReFuelEU [91]. Overall, this work supports the development of more reliable tools for quantifying non-CO_2 climate impacts, enabling improved environmental decision-making in the transition towards more sustainable aviation systems.

Chapter 6

Conclusions

6.1 Contributions to Knowledge

The research presented in this thesis contributes to knowledge in aircraft performance, emissions, and climate impact modelling. The primary novelty lies in the development of modelling approaches that combine physics-based aircraft, propulsion, and combustion simulation with real-world operational data. This enables current and future aircraft technologies to be assessed under representative airline operations, rather than through isolated design-mission assumptions alone.

The first contribution is the development of an operationally representative aircraft modelling framework for assessing energy consumption and emissions across realistic flight schedules. By integrating measured airline flight data with validated physics-based aircraft and propulsion models, the framework extends conceptual aircraft assessment beyond design-point or nominal design-range analysis. This provides a basis for evaluating aircraft technologies in the context of operational deployment across an airline network.

The second contribution is the development of a fleet-scale framework for evaluating alternative aviation decarbonisation pathways. While hydrogen aircraft modelling and SAF pathway assessment have previously been considered as separate problems, this thesis integrates aircraft performance modelling, fuel pathway analysis, and real-world airline operations within a single comparative methodology. This provides a methodological basis for using conceptual aircraft modelling to support data-driven fleet-planning in the context of decarbonisation pathways.

The third contribution is the development of configuration-tailored CRN emissions models for improved NO_x prediction. Rather than applying a generic or highly simplified reactor network, the CRN architecture was adapted to represent combustors with different operating characteristics. This provides a more physically informed approach to one-dimensional combustion modelling and improves the representation of NO_x formation processes relative to empirical methods and generalised model architectures.

The fourth contribution is the integration of physics-based emissions prediction with climate impact assessment for real-world aircraft operations. By coupling operational flight simulation, CRN-based NO_x modelling, and climate response calculations, the thesis establishes a framework for assessing how emissions modelling fidelity influences the estimated climate impact of aircraft technologies and fleet renewal strategies. This supports more physically representative evaluation of non-CO_2 effects in future emissions monitoring and policy contexts.

Overall, the thesis provides a physically grounded, operationally representative, and computationally efficient modelling framework for evaluating future aircraft technologies and fuel pathways. The contribution is not limited to individual model components, but lies in the integration of aircraft design, propulsion modelling, emissions prediction, operational deployment, and climate impact assessment within a scalable framework for aviation decarbonisation analysis.

6.2 Decarbonisation Pathways

The analysis of alternative fuel pathways demonstrates that the relative performance of hydrogen and sustainable aviation fuels depends strongly on the system boundary considered. While hydrogen-powered aircraft incur operational penalties associated with increased structural mass and volumetric constraints, these disadvantages are offset at the system level by the high efficiency of green hydrogen production pathways. For the aircraft configurations and fuel pathway assumptions assessed, hydrogen configurations can achieve lower overall energy demand than synthetic drop-in fuels when evaluated on a well-to-wake basis.

In contrast, the SAF pathways considered exhibit substantially higher upstream energy requirements, shifting the decarbonisation burden from aircraft performance to fuel production. Although near-term SAF pathways provide operational compatibility and competitive energy performance, their long-term scalability is constrained by feedstock availability and lifecycle considerations. This highlights a fundamental trade-off between operational feasibility and long-term sustainability across fuel pathways.

The results further indicate that advancements in airframe and propulsion efficiency reduce the relative penalties associated with hydrogen storage, suggesting that next-generation aircraft configurations may improve the viability of hydrogen-powered operations. In particular, the integration of technologies such as intercooling and recuperation provides incremental but meaningful reductions in total energy demand, reinforcing the importance of coupled airframe-propulsion optimisation.

Overall, these findings demonstrate that meaningful assessment of aviation decarbonisation strategies requires a holistic evaluation of both aircraft-level performance and upstream energy systems. Approaches that focus solely on in-flight efficiency risk underestimating the broader energy implications of fuel choice. As a result, system-level modelling frameworks that capture real-world operational behaviour are essential for informing technology development and policy decisions aimed at minimising lifecycle energy demand and reducing pressure on renewable energy infrastructure.

6.3 Non-Carbon Emissions

The results demonstrate that the choice of emissions modelling methodology has a substantial influence on the predicted climate impact of aviation, particularly for nitrogen oxides. Physics-based CRN models capture variations in combustor behaviour and operating conditions that are not resolved by conventional empirical correlations, leading to systematically different predictions of emission indices under real-world flight conditions. As a result, simplified methods may misrepresent both the magnitude and direction of non-CO_2 climate impacts.

This has important implications for the evaluation of mitigation strategies. In particular, the climate benefits associated with technological improvements and fleet renewal are shown to be highly sensitive to the underlying emissions model. Higher-fidelity approaches reveal stronger reductions in non-CO_2 warming effects for newer aircraft configurations, indicating that empirical methods may underestimate the climate advantages of modern propulsion systems. Consequently, accurate representation of NO_x formation processes is essential for robust comparison of the climate impact associated with different aircraft technologies.

The findings also highlight a critical gap in current emissions monitoring and regulatory frameworks. Existing approaches, which rely predominantly on empirical methods, may not provide sufficient accuracy for policy mechanisms that aim to mitigate non-CO_2 climate effects. This introduces the risk of misaligned incentives, where mitigation strategies are either under- or over-valued due to modelling limitations. Incorporating higher-fidelity emissions prediction methods into regulatory tools would improve the reliability of climate impact assessments and support more effective policy design.

More broadly, the integration of CRN-based emissions modelling within an operational aircraft simulation framework enables a consistent, physics-based assessment of both CO_2 and non-CO_2 impacts. This provides a foundation for extending analysis to additional climate-relevant processes, including contrail formation and fuel-dependent effects, thus supporting more comprehensive evaluation of future aircraft technologies. Overall, these results demonstrate that advancing the fidelity of non-CO_2 emissions modelling is essential for accurately quantifying aviation's climate impact and for informing both technology development and policy decisions.

When considered alongside the decarbonisation pathway analysis, these findings show that assessments of future aircraft technologies are strongly dependent on modelling scope. The fuel pathway analysis demonstrates that system-level energy demand can be dominated by upstream production assumptions, while the non-CO_2 analysis demonstrates that climate impact estimates are sensitive to the fidelity of emissions modelling. Therefore, technology comparisons based only on aircraft-level fuel burn or simplified emissions methods may misrepresent the relative benefits of hydrogen aircraft, SAF pathways, and fleet renewal strategies.

6.4 Research Questions

1. *How can physics-based aircraft, propulsion, and combustion models be integrated with real-world flight data to accurately predict aircraft performance and emissions across complete flight schedules?*

Physics-based aircraft, propulsion, and combustion models can be integrated with real-world flight data by using operational data to define mission-specific boundary conditions, calibrate uncertain model parameters, and validate predicted performance over complete flight schedules. In this thesis, measured airline data were used to reconstruct representative trajectories and operating conditions, enabling aircraft performance and emissions to be evaluated under realistic operational variability rather than idealised design assumptions.

The main mechanism enabling this integration was the coupling of physics-based aircraft, propulsion, and combustion models with reduced-order surrogate models. The physics-based models preserved consistency between aircraft state, engine operating condition, fuel flow, and emissions formation, while the surrogate models provided the computational speed required for fleet-scale mission analysis. CRN emissions models were then driven by propulsion model outputs, allowing NO_x predictions to be linked directly to mission-specific engine operating conditions.

This approach demonstrated that detailed aircraft, propulsion, and combustion models can be applied across large operational datasets without prohibitive computational cost. It therefore provides a practical method for assessing aircraft energy consumption, CO_2, and NO_x emissions under the conditions in which aircraft are actually operated.

2. *To what extent do aircraft technology level, hydrogen tank gravimetric index, and engine cycle enhancements influence the performance of hydrogen-powered aircraft relative to SAF-powered counterparts?*

Aircraft technology level, hydrogen tank gravimetric index, and engine cycle enhancements strongly influence the performance of hydrogen-powered aircraft relative to SAF-powered counterparts, with tank gravimetric index being the dominant design parameter. Lower gravimetric index values increase the mass and volume penalties associated with LH_2 storage, which increases aircraft size, operating empty mass, and mission energy consumption.

The effect of gravimetric index is coupled to the underlying aircraft technology level. Improved airframe and propulsion efficiency reduce the fuel mass and storage volume required for each mission, thereby reducing the relative penalty of LH_2 storage. Engine cycle enhancements, such as intercooling and recuperation, provide additional performance benefits, but these are secondary to the combined influence of aircraft efficiency and storage-system performance.

The results show that hydrogen aircraft competitiveness cannot be assessed from storage assumptions or design-range performance alone. Its viability relative to SAF-powered aircraft depends on the interaction between storage technology, aircraft efficiency, and mission requirements. Fleet-level operational analysis is therefore required to identify where hydrogen configurations offer system-level advantages and where SAF-powered aircraft remain the more practical decarbonisation pathway.

3. *How does the use of physics-based non-CO_2 emissions models at the mission level affect the estimated climate impact of aircraft operations when compared with empirical approaches?*

The use of physics-based non-CO_2 emissions models at the mission level materially changes the estimated climate impact of aircraft operations when compared with empirical approaches. The CRN models produced different NO_x emission indices across the flight envelope, particularly during cruise, where empirical methods rely on extrapolation from limited ground-based certification data.

The direction of this difference depended on combustor architecture and operating regime. For the RQL combustor, the CRN model predicted higher NO_x emissions due to increased thermal NO formation under cruise conditions. For the TAPS-II combustor, the configuration-tailored CRN model predicted lower NO_x emissions by representing staged combustion behaviour that is not captured by empirical fuel-flow-based correlations.

These differences propagated through the radiative forcing and surface temperature response calculations, changing both the magnitude and interpretation of the estimated climate impact. The results therefore show that empirical approaches may under- or over-predict non-CO_2 effects depending on combustor design and mission operating conditions. This demonstrates the importance of physics-based emissions modelling for robust climate assessment of modern aircraft technologies, particularly outside the certification envelope.

4. *To what extent can fleet renewal strategies reduce the overall climate impact of commercial aircraft operations, when accounting for both CO_2 and non-CO_2 effects under realistic operational conditions?*

Fleet renewal can substantially reduce the overall climate impact of commercial aircraft operations by lowering both fuel consumption and emissions. Under realistic operating schedules, newer aircraft reduce CO_2 emissions through improved fuel efficiency, producing long-term reductions in climate impact over the 100-year assessment period.

The timing of the benefit depends strongly on the inclusion of non-CO_2 effects. Reductions in NO_x emissions provide larger relative benefits in the near term because NO_x-driven climate effects occur over shorter timescales than CO_2. The estimated magnitude of this benefit is sensitive to the emissions modelling approach, with CRN-based methods indicating larger non-CO_2 reductions than empirical methods for the fleet renewal case assessed.

The results therefore show that fleet renewal is an effective mitigation strategy, but its climate benefit may be misrepresented if non-CO_2 effects or emissions modelling fidelity are neglected. Accurate assessment requires mission-level performance and emissions modelling under representative operations, especially where non-CO_2 effects are relevant to policy, reporting, or fleet-planning decisions.

6.5 Uncertainty & Limitations

6.5.1 Input & Parameter Uncertainty

Input uncertainty arises from both measured operational data and assumed model parameters. The QAR data used to reconstruct flight trajectories and validate fuel consumption predictions were sampled at 1 Hz for the B737-NG aircraft and between 0.08–0.33 Hz for the B737-MAX aircraft. Instrument tolerances were small for the principal flight-state variables, with altitude recorded to within ± 1 ft, Mach number to within ± 0.001, and fuel flow to within ± 8 lb/hr per engine. The altitude and Mach number uncertainties are small relative to those introduced by the trajectory reconstruction process, where flight paths were approximated using linear segments. Fuel-flow uncertainty is more consequential, as it propagates directly into model validation, tank-to-wake energy consumption, CO_2 emissions, and fuel-flow-based NO_x estimates.

Further uncertainty is introduced by assumed parameters used in the hydrogen aircraft, engine, fuel pathway, and emissions models. For the LH_2 configurations, storage-system gravimetric index, tank structural assumptions, and insulation requirements directly affect aircraft mass, payload capability, and mission energy consumption. Similarly, the predicted benefit of intercooling and recuperation depends on uncertain heat-exchanger performance assumptions. For both SAF and LH_2 pathways, well-to-wake energy demand is strongly dependent on assumed upstream production efficiencies, which can influence the relative ranking of fuel pathways. These uncertainties were mitigated by deriving input assumptions from published literature where available and, where appropriate, bounding the analysis using pessimistic and optimistic parameter values.

The emissions modelling also depends on uncertain input parameters. The CRN models require assumptions regarding reactor zone geometry, residence time, and air–fuel distribution, which were calibrated using Bayesian optimisation against ICAO emissions data. However, the available validation data are limited to a small number of ground-based certification points, increasing uncertainty when interpolating between operating conditions or extrapolating to cruise conditions. This limitation also affects empirical NO_x methods, which are similarly derived from sparse certification data and simplified correction procedures, reducing confidence when either approach is applied outside the certification envelope.

6.5.2 Model Sensitivity

The model outputs were most sensitive to parameters that directly affect aircraft mass, fuel pathway efficiency, combustor operating conditions, and climate response. For the LH_2 aircraft, storage-system gravimetric index was the dominant sensitivity. Lower gravimetric index values increased storage mass and volume, which increased aircraft size, operating empty mass, and mission energy consumption. This sensitivity was moderated by aircraft technology level, since more efficient aircraft required less fuel and were therefore less affected by the relative storage penalty. The results were also sensitive to mission range and trajectory characteristics, reinforcing the need to assess alternative-fuel aircraft over representative airline operations rather than isolated design missions.

Well-to-wake energy estimates were particularly sensitive to assumed upstream fuel production efficiencies. This was most evident for power-to-liquid and DAC-based SAF pathways, where multiple energy-intensive conversion steps strongly influenced total energy demand. Although the assumed pathway efficiencies affect the absolute values and relative rankings, they are applied as post-processing parameters within the framework. The analysis can therefore be updated readily as production technologies, regional electricity assumptions, or literature estimates change.

Emissions and climate impact results were sensitive to the selected propulsion and emissions modelling assumptions. Fuel-flow predictions affect emitted mass, CO_2 emissions, and fuel-flow-based empirical NO_x estimates, while CRN NO_x predictions are sensitive to combustor inlet temperature, pressure, and fuel–air ratio. These sensitivities are particularly important at cruise power settings, where small changes in combustor state can produce appreciable differences in predicted NO_x formation. The resulting climate impact estimates are also sensitive to the chosen emissions model and ATR time horizon, since changes in NO_x emission indices propagate through the radiative forcing and surface temperature response calculations.

Overall, the absolute values of energy consumption, emissions, and ATR remain sensitive to modelling assumptions. However, the main comparative conclusions are driven by dominant physical and methodological dependencies: LH_2 competitiveness depends strongly on storage-system performance, well-to-wake pathway rankings depend strongly on upstream fuel production efficiency, and non-CO_2 climate estimates depend materially on the selected NO_x emissions model. These sensitivities define the principal drivers that should be prioritised when interpreting the results and refining the framework.

6.5.3 Model Limitations

The modelling framework contains limitations associated with operational representation, model transferability, emissions prediction, and climate response modelling. Alternative aircraft configurations were evaluated using common mission trajectories to ensure consistent comparison between fuel pathways and aircraft technologies. However, this does not account for configuration-specific operational optimisation, such as changes in cruise altitude, speed schedule, or step-climb strategy. In addition, the absence of directly measured take-off weight data for prospective aircraft designs required aircraft mass to be estimated from operational and design assumptions, limiting the precision of mission-level energy and emissions estimates.

The aerodynamic, propulsion, and surrogate modelling approaches also constrain the transferability of the framework. Empirical drag prediction methods and calibration factors are most reliable for aircraft configurations close to the conventional narrow-body design space, and may not fully capture the effects of modified hydrogen aircraft geometries. Similarly, ANN surrogate models provide rapid approximations of NPSS propulsion models, but are limited to the operating conditions and engine architectures represented in their training data. New aircraft or propulsion configurations therefore require updated model calibration, surrogate training, and validation before application.

The CRN combustion models improve the physical representation of NO_x formation relative to empirical methods, but remain simplified representations of combustor behaviour. The combustor flow field is represented using discretised reactor zones with prescribed mixing, residence time, and air distribution assumptions, rather than resolving full three-dimensional reacting flow. As a result, local recirculation, wall cooling, fuel spray behaviour, turbulence–chemistry interaction, and spatial temperature gradients are not explicitly captured.

The climate impact assessment is limited by the use of reduced-order radiative forcing and temperature response models. These enable rapid evaluation across large operational datasets, but do not fully resolve spatial and temporal variability in atmospheric chemistry and meteorology. Furthermore, contrail formation is not considered in the modelling framework. Consequently, the calculated ATR values should be interpreted as comparative climate impact indicators rather than exact predictions of realised climate response.

These modelling choices reflect a trade-off between physical fidelity and computational efficiency, enabling fleet-scale scenario analysis at the conceptual design phase while avoiding the computational cost of high-fidelity CFD or chemistry–climate modelling. These limitations do not undermine the comparative value of the framework, but they mean that the results should be interpreted primarily as relative technology and pathway comparisons rather than exact predictions of realised fleet climate impact. Future work should therefore target these dominant sources of uncertainty and model-form limitation, while preserving the operationally representative and computationally scalable structure required for fleet-level scenario analysis.

6.6 Future Work

The framework developed in this thesis provides a basis for extending operationally representative aircraft performance, emissions, and climate impact assessment to a wider range of future technologies. Future work should prioritise the dominant sources of uncertainty identified in this chapter while preserving the computational efficiency required for fleet-scale scenario analysis.

The decarbonisation pathway analysis should be extended to a broader range of aircraft technology levels, fuel pathways, and propulsion architectures. In particular, next-generation narrow-body aircraft with substantially improved aerodynamic and propulsion efficiency should be assessed, since the results demonstrated a strong coupling between aircraft efficiency and hydrogen tank gravimetric index. This would enable more robust evaluation of long-term LH_2 viability relative to SAF pathways and other prospective low-carbon aircraft concepts. Further work should also examine sensitivity to updated upstream production efficiencies, regional electricity mixes, and evolving assumptions for fuel availability and infrastructure requirements.

Further validation of the CRN NO_x emissions models is also required. Additional validation data at intermediate power settings and, where possible, cruise-representative combustor conditions would improve confidence in extrapolation beyond the ICAO certification points. Higher-fidelity CRN architectures or CFD simulations could also be used to benchmark the simplified reactor network models and assess the influence of mixing, residence time, and spatial temperature distributions on predicted NO_x formation.

The non-CO_2 modelling framework should be extended to include physics-based nvPM predictions combined with contrail formation models. Coupling CRN-based combustion modelling with soot formation methods would enable more complete assessment of fuel-dependent non-CO_2 effects. This is particularly important for SAF pathways, where reduced aromatic and sulphur content may influence nvPM emissions and contrail formation. Incorporating these effects would allow future studies to evaluate decarbonisation strategies using a more complete representation of aviation climate impact.

Finally, the framework should be integrated within fleet-level optimisation studies. Coupling the aircraft and emissions models with fleet allocation, network optimisation, or mixed-integer linear programming methods would enable climate-optimised fleet transition strategies to be assessed under operational, economic, infrastructure, and sustainability constraints. This would extend the present work from comparative scenario analysis towards decision-support tools for identifying optimal aviation decarbonisation pathways while accounting for both CO_2 and non-CO_2 effects.

Bibliography

[1] European Commission. Roadmap to a single european transport area — towards a competitive and resource efficient transport system. Technical Report COM(2011) 144 final, European Commission, 2011.

[2] European Commission. 'fit for 55': delivering the eu's 2030 climate target on the way to climate neutrality. Technical Report COM(2021) 550 final, European Commission, 2021.

[3] Airlines for Europe (A4E), ACI Europe, ASD Europe, CANSO Europe, and ERA. Destination 2050: A route to net zero european aviation. Technical report, Destination 2050 Consortium, 2021.

[4] Air Transport Action Group. Waypoint 2050: Second edition. Technical report, ATAG, 2021.

[5] Jenny Osborne-Kinch, Dermot Coates, and Luke Nolan. The aircraft leasing industry in ireland: Cross-border flows and statistical treatment. Technical Report Quarterly Bulletin No. 1, Central Bank of Ireland, 2017.

[6] Department of Transport. Ireland's action plan for aviation emissions reduction. Technical report, Government of Ireland, 2019.

[7] Central Statistics Office. Overseas travel statistics, 2023. URL `https://www.cso.ie/en/statistics/tourismandtravel/airandseatravelstatistics/`. Accessed: 2026-04-28.

[8] International Civil Aviation Organization. ICAO and United Nations sustainable development goals, 2026. URL `https://www.icao.int/icao-and-united-nations-sustainable-development-goals`. Accessed: 2026-04-01.

[9] Clean Sky 2 Joint Undertaking and Fuel Cells and Hydrogen Joint Undertaking. Hydrogen–powered aviation: A fact-based study of hydrogen technology, economics, and climate impact by 2050. Technical report, Clean Sky 2 JU and FCH JU, 2020.

[10] Transport & Environment. Airline emissions growth out of control, 2019. URL `https://www.transportenvironment.org/articles/airline-emissions-growth-out-control`. Accessed: 2026-04-29.

[11] European Parliament and Council of the European Union. Establishing a scheme for greenhouse gas emission allowance trading within the community and amending council directive 96/61/EC. Technical Report Directive 2003/87/EC, Official Journal of the European Union, 2003.

[12] D.S. Lee, D.W. Fahey, A. Skowron, M.R. Allen, U. Burkhardt, Q. Chen, S.J. Doherty, S. Freeman, P.M. Forster, J. Fuglestvedt, A. Gettelman, R.R. De León, L.L. Lim, M.T. Lund, R.J. Millar, B. Owen, J.E. Penner, G. Pitari, M.J. Prather, R. Sausen, and L.J. Wilcox. The contribution of global aviation to anthropogenic climate forcing for 2000 to 2018. *Atmospheric Environment*, 244:117834, January 2021. doi: 10.1016/j.atmosenv.2020.117834.

[13] Boeing. Sustainability report. Technical report, The Boeing Company, 2022.

[14] Airbus. Airbus reveals new zero-emission concept aircraft, 2020. URL `https://www.airbus.com/en/newsroom/press-releases/2020-09-airbus-reveals-new-zero-emission-concept-aircraft`. Accessed: 2026-04-28.

[15] United Nations Framework Convention on Climate Change. Paris agreement. Technical report, UNFCCC, 2015.

[16] Roger Teoh, Zebediah Engberg, Ulrich Schumann, Christiane Voigt, Marc Shapiro, Susanne Rohs, and Marc E. J. Stettler. Global aviation contrail climate effects from 2019 to 2021. *Atmospheric Chemistry and Physics*, 24(10), May 2024. doi: 10.5194/acp-24-6071-2024.

[17] European Commission. Guidance document: The accreditation and verification regulation – verification guidance for EU ETS aviation. Technical report, European Commission, 2026.

[18] Rolls-Royce plc. CTO joint statement, 2024. URL `https://www.rolls-royce.com/~/media/Files/R/Rolls-Royce/documents/news/press-releases/cto-joint-statement-22-07-2024.pdf`. Accessed: 2025-12-26.

[19] European Union Aviation Safety Agency (EASA), European Environment Agency (EEA), and Eurocontrol. European aviation environmental report 2019. Technical report, EASA, EEA and Eurocontrol, 2019.

[20] John D. Anderson. *Aircraft Performance and Design*. McGraw–Hill, 1st edition, 1999.

[21] J. Sun, J. Hoekstra, and J. Ellerbroek. Aircraft drag polar estimation based on a stochastic hierarchical model. In *Proceedings of the 8th SESAR Innovation Days*, Salzburg, Austria, December 2018.

[22] J. D. Mattingly. *Elements of Gas Turbine Propulsion*. McGraw–Hill, 2nd edition, 1996.

[23] International Air Transport Association. The global commercial aircraft fleet. Technical report, IATA, 2025.

[24] Rolls-Royce. *The Jet Engine*. Wiley, 5th edition, 2015.

[25] H. I. H. Saravanamuttoo, G. F. C. Rogers, H. Cohen, and P. V. Straznicky. *Gas Turbine Theory*. Prentice Hall, 6th edition, 2009.

[26] U.S. Department of Energy. Sustainable aviation fuel: Review of technical pathways. Technical Report DOE/EE–2041, U.S. Department of Energy, 2020.

[27] Intergovernmental Panel on Climate Change. 2006 IPCC guidelines for national greenhouse gas inventories, volume 2: Energy. Technical report, IPCC, 2006.

[28] ASTM International. Standard specification for aviation turbine fuel containing synthesized hydrocarbons. Technical Report ASTM D7566-22, ASTM International, 2022.

[29] R. G. Grim, Z. Huang, M. T. Guarnieri, J. R. Ferrell, L. Tao, and J. A. Schaidle. Electrifying the production of sustainable aviation fuel: The risks, economics, and environmental benefits of emerging pathways including CO_2. *Energy & Environmental Science*, 15(11):4698–4812, 2022. doi: 10.1039/D2EE02439J.

[30] Air Transport Action Group. Waypoint 2050: Fueling net zero. Technical report, ATAG, 2021.

[31] B. C. Tashie-Lewis and S. G. Nnabuife. Hydrogen production, distribution, storage and power conversion in a hydrogen economy – a technology review. *Chemical Engineering Journal Advances*, 8:100172, 2021. doi: 10.1016/j.ceja.2021.100172.

[32] R. W. Howarth and M. Z. Jacobson. How green is blue hydrogen? *Energy Science & Engineering*, 9(10):1676–1687, 2021. doi: 10.1002/ese3.956.

[33] International Energy Agency. Global hydrogen review 2022. Technical report, IEA, 2022.

[34] M. Awde and C. Stuart. Characterizing the full climate impact of individual real-world flights using a linear temperature response model. *Aerospace*, 12(2):121, 2025. doi: 10.3390/aerospace12020121.

[35] Intergovernmental Panel on Climate Change. Climate change 2021: The physical science basis. contribution of working group I to the sixth assessment report of the ipcc. Technical report, IPCC, 2021.

[36] B. Kärcher. Formation and radiative forcing of contrail cirrus. *Nature Communications*, 9:1824, 2018. doi: 10.1038/s41467-018-04068-0.

[37] L. Durdina, B. T. Brem, M. Elser, D. Schönenberger, F. Siegerist, and J. G. Anet. Reduction of nonvolatile particulate matter emissions of a commercial turbofan engine

at the ground level from the use of a sustainable aviation fuel blend. *Environmental Science & Technology*, 55(21):14576–14585, 2021. doi: 10.1021/acs.est.1c04744.

[38] Britannica Editors. contrail, 2026. URL `https://www.britannica.com/science/vapor-trail`. Accessed: 2026-04-01.

[39] R. E. G. Davies and P. Birtles. *De Havilland Comet: The World's First Jet Airliner*. Paladwr Press, 1999.

[40] A. S. J. van Heerden, M. D. Guenov, and A. Molina-Cristóbal. Evolvability and design reuse in civil jet transport aircraft. *Progress in Aerospace Sciences*, 108:121–155, 2019.

[41] Federal Aviation Administration. Airworthiness certification, 2025. URL `https://www.faa.gov/aircraft/air_cert/airworthiness_certification`. Accessed: 2025-11-28.

[42] T. Chau and D. W. Zingg. Aerodynamic design optimization of a transonic strut-braced-wing regional aircraft. *Journal of Aircraft*, 59(1), 2021. doi: 10.2514/1.C036389.

[43] M. K. Bradley and C. K. Droney. Subsonic ultra green aircraft research: Phase II – volume II – hybrid electric design exploration. Technical Report NASA/CR–2015-218704/Volume II, NASA, 2015.

[44] J. Gould. A future aircraft design, supercomputed, 2023. URL `https://www.nasa.gov/aeroresearch/a-future-aircraft-design-supercomputed`. Accessed: 2025-11-28.

[45] D. P. Wells, G. M. Gatlin, J. C. June, and T. V. Marien. Nasa transonic truss-braced wing studies. In *Proceedings of the 34th Congress of the International Council of the Aeronautical Sciences (ICAS 2024)*, Florence, Italy, 2024.

[46] R. H. Liebeck. Design of the blended wing body subsonic transport. *Journal of Aircraft*, 41(1):10–25, 2004. doi: 10.2514/1.9084.

[47] J. Felder, M. Tong, and J. Chu. Sensitivity of mission energy consumption to turboelectric distributed propulsion design assumptions on the N3-X hybrid wing body aircraft. In *48th AIAA/ASME/SAE/ASEE Joint Propulsion Conference & Exhibit*, Atlanta, GA, USA, 2012. doi: 10.2514/6.2012-3701.

[48] A. Magrini, E. Benini, H.-D. Yao, J. Postma, and C. Sheaf. A review of installation effects of ultra-high bypass ratio engines. *Progress in Aerospace Sciences*, 119:100680, 2020. doi: 10.1016/j.paerosci.2020.100680.

[49] D. Mo, I. Roumeliotis, C. Mourouzidis, S. Kissoon, and Y. Liu. Assessment of performance boundaries and operability of low specific thrust GUHBPR engines for EIS2025. *Journal of Engineering for Gas Turbines and Power*, 144(7), May 2022. doi: 10.1115/1.4054405.

[50] S. M. Jones, W. J. Haller, and M. T.-H. Tong. An N+3 technology level reference propulsion system. Technical Report NASA/TM—2017-219501, NASA, 2017.

[51] F. S. Mastropierro, J. Sebastiampillai, F. Jacob, and A. Rolt. Modeling geared turbofan and open rotor engine performance for year-2050 long-range and short-range aircraft. *Journal of Engineering for Gas Turbines and Power*, 142(4), April 2020. doi: 10.1115/1.4045077.

[52] S. Reitenbach, A. Krumme, T. Behrendt, M. Schnös, T. Schmidt, S. Hönig, R. Mischke, and E. Mörland. Design and application of a multidisciplinary predesign process for novel engine concepts. *Journal of Engineering for Gas Turbines and Power*, 141 (1), January 2019. doi: 10.1115/1.4040750.

[53] R. A. Clark, C. Perron, J. C. Tai, B. J. Airdo, and D. N. Mavris. Development of an open rotor propulsion system model and power management strategy. In *AIAA SCITECH 2023 Forum*, National Harbor, Maryland, USA, January 2023. doi: 10.2514/6.2023-0309.

[54] A. Dorsey and A. Uranga. Design space exploration of future open rotor configurations. In *AIAA Propulsion and Energy 2020 Forum*, August 2020. doi: 10.2514/6.2020-3680.

[55] CFM International. RISE: A step change in aircraft propulsion, 2021. URL `https://www.geaerospace.com/sites/default/files/brochure-rise-a-step-change-in-aircraft-propulsion.pdf`. Accessed: 2026-04-28.

[56] L. Larsson, T. Grönstedt, and K. G. Kyprianidis. Conceptual design and mission analysis for a geared turbofan and an open rotor configuration. In *ASME 2011 Turbo Expo: Turbine Technical Conference and Exposition*, pages 359–370, Vancouver, British Columbia, Canada, May 2011. American Society of Mechanical Engineers. doi: 10.1115/GT2011-46451.

[57] C. Gallagher, C. J. Stuart, and S. Spence. Advanced propulsion system evaluation for real-world short-haul operations: Open rotor vs. UHBPR turbofan. In *AIAA AVIATION FORUM AND ASCEND 2024*, Las Vegas, Nevada, USA, July 2024. doi: 10.2514/6.2024-3990.

[58] P. Wheeler and S. Bozhko. The more electric aircraft: Technology and challenges. *IEEE Electrification Magazine*, 2(4):6–12, December 2014. doi: 10.1109/MELE.2014.2360720.

[59] B. J. Brelje and J. R. R. A. Martins. Electric, hybrid, and turboelectric fixed-wing aircraft: A review of concepts, models, and design approaches. *Progress in Aerospace Sciences*, 104:1–19, January 2019. doi: 10.1016/j.paerosci.2018.06.004.

[60] J. C. Gladin, D. Trawick, D. Mavris, M. Armstrong, D. Bevis, and K. Klein. Fundamentals of parallel hybrid turbofan mission analysis with application to the electrically variable engine. In *2018 AIAA/IEEE Electric Aircraft Technologies Symposium (EATS)*, Cincinnati, OH, USA, July 2018. doi: 10.2514/6.2018-5024.

[61] C. Perullo, D. Trawick, M. Armstrong, J. C. Tai, and D. N. Mavris. Cycle selection and sizing of a single-aisle transport with the electrically variable engine (EVE) for fleet level fuel optimization. In *AIAA SciTech Forum, 55th AIAA Aerospace Sciences Meeting*, Grapevine, Texas, USA, January 2017. doi: 10.2514/6.2017-1923.

[62] A. R. Gnadt, R. L. Speth, J. S. Sabnis, and S. R. H. Barrett. Technical and environmental assessment of all-electric 180-passenger commercial aircraft. *Progress in Aerospace Sciences*, 105:1–30, February 2019. doi: 10.1016/j.paerosci.2018.11.002.

[63] Rob E. Wolleswinkel, R. de Vries, M. Hoogreef, and Roelof Vos. A new perspective on battery-electric aviation, part i: Reassessment of achievable range. In *AIAA SCITECH 2024 Forum*, Orlando, Florida, USA, January 2024. doi: 10.2514/6.2024-1489.

[64] International Energy Agency. The future of hydrogen: Seizing today's opportunities. Technical report, IEA, 2019.

[65] J. Mukhopadhaya and D. Rutherford. Performance analysis of evolutionary hydrogen-powered aircraft. Technical report, International Council on Clean Transportation (ICCT), 2022.

[66] A. Baroutaji, T. Wilberforce, M. Ramadan, and A. G. Olabi. Comprehensive investigation on hydrogen and fuel cell technology in the aviation and aerospace sectors. *Renewable and Sustainable Energy Reviews*, 106:31–40, May 2019. doi: 10.1016/j.rser.2019.02.022.

[67] J. Huete and P. Pilidis. Parametric study on tank integration for hydrogen civil aviation propulsion. *International Journal of Hydrogen Energy*, 46(74):37049–37062, October 2021. doi: 10.1016/j.ijhydene.2021.08.194.

[68] D. Verstraete. On the energy efficiency of hydrogen-fuelled transport aircraft. *International Journal of Hydrogen Energy*, 40(23):7388–7394, 2015. doi: 10.1016/j.ijhydene.2015.04.055.

[69] J. E. Fesmire et al. Development and validation of cryogenic foam insulation for LH2 subsonic transports. Technical Report NASA-CR-165404, National Aeronautics and Space Administration (NASA), 1981.

[70] GE Vernova. Hydrogen for power generation. Technical Report GEA34805, GE Vernova, 2025.

[71] D. Cecere, E. Giacomazzi, and A. Ingenito. A review on hydrogen industrial aerospace applications. *International Journal of Hydrogen Energy*, 39(20):10731–10747, 2014. doi: 10.1016/j.ijhydene.2014.04.126.

[72] B. Khandelwal, P. Sekaran, A. Karakurt, V. Sethi, and R. Singh. A review of hydrogen as a fuel for future air transport. In *48th AIAA/ASME/SAE/ASEE Joint Propulsion Conference & Exhibit*, Atlanta, Georgia, USA, July 2012. doi: 10.2514/6.2012-4267.

[73] BBC. Rolls-royce tests a jet engine running on hydrogen, 2022. URL `https://www.bbc.com/news/business-63758937`. Accessed: 2026-04-28.

[74] P. Murthy, B. Khandelwal, V. Sethi, and R. Singh. Hydrogen as a fuel for gas turbine engines with novel micromix type combustors. In *47th AIAA/ASME/SAE/ASEE Joint Propulsion Conference & Exhibit*, San Diego, California, USA, July 2011. doi: 10.2514/6.2011-5806.

[75] H. H.-W. Funke, N. Beckmann, and S. Abanteriba. An overview on dry low NO_x micromix combustor development for hydrogen-rich gas turbine applications. *International Journal of Hydrogen Energy*, 44(13):6978–6990, 2019. doi: 10.1016/j.ijhydene.2019.01.161.

[76] N. Tekin, M. Ashikaga, A. Horikawa, and H. Funke. Enhancement of fuel flexibility of industrial gas turbines by development of innovative hydrogen combustion systems. In *10th International Gas Turbine Conference*, 2021.

[77] Jan Roskam. *Airplane Design Part VI: Preliminary Calculation of Aerodynamic, Thrust and Power Characteristics*. The University of Kansas, 1990.

[78] S. Karpuk and A. Elham. Comparative study of hydrogen and kerosene commercial aircraft with advanced airframe and propulsion technologies for more sustainable aviation. *Journal of Aerospace Engineering*, 237(9):2074—-2091, 2022. doi: 10.1177/09544100221144342.

[79] G. D. Brewer. *Hydrogen Aircraft Technology*. CRC Press, 1st edition, 1991.

[80] Arthur H. Lefebvre and Dilip R. Ballal. *Gas Turbine Combustion: Alternative Fuels and Emissions*. CRC Press, 3rd edition, 2010.

[81] Alexandre Capitão Patrão, Carlos Xisto, Isak Jönsson, Anders Lundbladh, and Tomas Grönstedt. Compact heat exchangers for hydrogen-fueled aero engine intercooling and recuperation. *Applied Thermal Engineering*, 234:122538, 2024. doi: 10.1016/j.applthermaleng.2024.122538.

[82] Alexander Görtz and Daniel Silberhorn. Thermodynamic potential of turbofan engines with direct combustion of hydrogen. In *33rd Congress of the International Council of the Aeronautical Sciences, ICAS 2022*, September 2022. URL `https://www.icas.org/icas_archive/ICAS2022/data/papers/ICAS2022_0499_paper.pdf`.

[83] William M. Kays and Alexander L. London. *Compact Heat Exchangers*. Krieger Publishing, 3rd edition, 1998.

[84] R. Martinez-Val, J. Roa, E. Perez, and C. Cuerno. Effects of the mismatch between design capabilities and actual aircraft utilization. *Journal of Aircraft*, 48(6):1921–1927, 2011. doi: 10.2514/1.C031348.

[85] M. Kousoulidou and L. Lonza. Biofuels in aviation: Fuel demand and CO_2 emissions evolution in Europe toward 2030. *Transportation Research Part D: Transport and Environment*, 46:166–181, 2016. doi: 10.1016/j.trd.2016.03.018.

[86] M. Micheli, D. Moore, V. Bach, and M. Finkbeiner. Life-cycle assessment of power-to-liquid kerosene produced from renewable electricity and CO_2 from direct air capture in germany. *Sustainability*, 14(17), 2022. doi: 10.3390/su141710658.

[87] K. O. Ploetner, M. Urban, A. Roth, G. Tay, and A. Habersetzer. Fulfilling long-term emission reduction goals in aviation by alternative fuel options: An evolutionary approach. In *2018 Aviation Technology, Integration, and Operations Conference (AIAA AVIATION Forum)*, Atlanta, Georgia, USA, 2018. doi: 10.2514/6.2018-3990.

[88] I. Abrantes, A. F. Ferreira, A. Silva, and M. Costa. Sustainable aviation fuels and imminent technologies – CO_2 emissions evolution towards 2050. *Journal of Cleaner Production*, 313:127937, 2021. doi: 10.1016/j.jclepro.2021.127937.

[89] A. Navarrete, N. Pavlenko, and J. O'Malley. SAF policy scorecard: Evaluating state-level sustainable aviation fuel policies in the united states. Technical report, International Council on Clean Transportation (ICCT), 2024.

[90] M. Ballesteros, R. Neiva, G. Horton, A. Pons, K. Lokesh, L. Casullo, A. Kauffmann, G. Giannelos, M. Kemp, and N. Kusnierkiewicz. Investment scenario and roadmap for achieving aviation green deal objectives by 2050. Technical report, European Parliament, Policy Department for Structural and Cohesion Policies, 2022.

[91] European Commission. Proposal for a regulation of the european parliament and of the council on ensuring a level playing field for sustainable air transport. Technical Report COM(2021) 561 final, European Commission, 2021.

[92] Y. Zhou, S. Searle, and N. Pavlenko. Current and future cost of E-kerosene in the united states and europe. Technical report, International Council on Clean Transportation (ICCT), 2022.

[93] Concawe. Sustainable biomass availability in the EU to 2050. Technical report, Concawe, 2022.

[94] E. Cabrera and J. M. Melo de Sousa. Use of sustainable fuels in aviation – a review. *Energies*, 15(7), 2022. doi: 10.3390/en15072440.

[95] S. Searle, N. Pavlenko, A. Kharina, and J. Giuntoli. Long-term aviation fuel decarbonization: Progress, roadblocks, and policy opportunities. Technical report, International Council on Clean Transportation (ICCT), 2019.

[96] International Energy Agency. Electricity 2026. Technical report, IEA, 2024.

[97] International Energy Agency. World energy outlook 2024. Technical report, IEA, 2024.

[98] International Transport Forum. The potential of E-fuels to decarbonise ships and aircraft. Technical Report 111, OECD Publishing, 2023.

[99] Y. Liu andX. Sun, V. Sethi, D. Nalianda, Y.-G. Li, and L. Wang. Review of modern low emissions combustion technologies for aero gas turbine engines. *Progress in Aerospace Sciences*, 94:12–45, 2017. doi: 10.1016/j.paerosci.2017.08.001.

[100] Q. Shen, Y. Huang, F. Xing, H. Peng, and Z. Lin. A physics based reactor network model of rql combustors. In *Global Power and Propulsion Forum 2017*, Shanghai, China, October 2017. URL `https://gpps.global/wp-content/uploads/2021/01/GPPS-SHA17-193.pdf`.

[101] G. S. Samuelsen. Rich burn–quick mix–lean burn (rql) combustor. Technical report, National Energy Technology Laboratory (NETL), 2006. Accessed: 2025-12-03.

[102] M. Foust, D. Thomsen, R. Stickles, C. Cooper, and W. Dodds. Development of the GE aviation low emissions TAPS combustor for next generation aircraft engines. In *50th AIAA Aerospace Sciences Meeting including the New Horizons Forum and Aerospace Exposition*, Nashville, Tennessee, USA, January 2012. doi: 10.2514/6.2012-936.

[103] D. Dubois and G. Paynter. "fuel flow method2" for estimating aircraft emissions. In *SAE Technical Paper Series*, 2006. doi: 10.4271/2006-01-1987.

[104] H. Aygun and O. Turan. Analysis of cruise conditions on energy, exergy and NO_x emission parameters of a turbofan engine for middle-range aircraft. *Energy*, 267: 126468, 2023. doi: 10.1016/j.energy.2022.126468.

[105] M. Schaefer and S. Bartosch. Overview on fuel flow correlation methods for the calculation of NO_x, CO and HC emissions and their implementation into aircraft performance software. Technical report, German Aerospace Center (DLR), 2013.

[106] NASA Global Modeling and Assimilation Office (GMAO). inst3_3d_asm_Np: MERRA-2 3D instantaneous assimilation, meteorology on pressure levels, 2015.

[107] T. Rindlisbacher and U. Ziegler. Icao's work on NO_x emissions regulation. In *ICAO Environmental Report 2025*. International Civil Aviation Organization (ICAO), Montreal, Canada, 2025.

[108] S. Villette, D. Adam, A. Alexiou, N. Aretakis, and K. Mathioudakis. A simplified chemical reactor network approach for aeroengine combustion chamber modeling and preliminary design. *Aerospace*, 11(1), 2023. doi: 10.3390/aerospace11010022.

[109] K. Ziaja, D. Lieder, J. Göing, J. Friedrichs, and F. di Mare. Design approach for hybrid electric propulsion concepts of mid-range aircraft including sustainable aviation fuels. In *34th Congress of the International Council of the Aeronautical Sciences, ICAS 2024*, Florence, Italy, September 2024. URL `https://www.icas.org/icas_archive/icas2024/data/papers/icas2024_1069_paper.pdf`.

[110] T. Bräuer, C. Voigt, D. Sauer, S. Kaufmann, V. Hahn, M. Scheibe, H. Schlager, F. Huber, P. Le Clercq, R. H. Moore, and B. E. Anderson. Reduced ice number concentrations in contrails from low-aromatic biofuel blends. *Atmospheric Chemistry and Physics*, 21(22):16817–16826, 2021. doi: 10.5194/acp-21-16817-2021.

[111] R. Lamioni, A. Mariotti, M. V. Salvetti, and C. Galletti. Predictive surrogate model for NO_x emissions in gas turbine systems fed with ammonia/hydrogen blends. In *46th MEETING OF THE ITALIAN SECTION OF THE COMBUSTION INSTITUTE, ASICI 2024*, Bari, Italy, 2024. URL `https://www.combustion-institute.it/proceedings/XXXXVI-ASICI/papers/46proci2024.V3.pdf`.

[112] A. Korsunovs, O. Garcia-Afonso, and E. Tunc. Validation of a multi-physics simulation platform for engine emissions modelling. *International Journal of Engine Research*, 2021. doi: 10.1177/14680874211064383.

[113] L. Zhou, Y. Song, W. Ji, and H. Wei. Machine learning for combustion. *Energy and AI*, 7:100128, 2022. doi: 10.1016/j.egyai.2021.100128.

[114] J. C. Corbin, T. Schripp, B. E. Anderson, G. J. Smallwood, P. LeClercq, E. C. Crosbie, S. Achterberg, P. D. Whitefield, R. C. Miake-Lye, Z. Yu, A. Freedman, M. Trueblood, D. Satterfield, W. Liu, P. Oßwald, C. Robinson, M. A. Shook, R. H. Moore, and P. Lobo. Aircraft-engine particulate matter emissions from conventional and sustainable aviation fuel combustion: Comparison of measurement techniques for mass, number, and size. *Atmospheric Measurement Techniques*, 15(10):3223–3244, 2022. doi: 10.5194/amt-15-3223-2022.

[115] A. M. Boies, M. E. J. Stettler, J. J. Swanson, T. J. Johnson, J. S. Olfert, M. Johnson, M. L. Eggersdorfer, T. Rindlisbacher, J. Wang, K. Thomson, G. Smallwood, Y. Sevcenco, D. Walters, P. I. Williams, J. Corbin, A. A. Mensah, J. Symonds, R. Dastanpour, and S. N. Rogak. Particle emission characteristics of a gas turbine with a double annular combustor. *Aerosol Science and Technology*, 49(9):842–855, 2015. doi: 10.1080/02786826.2015.1078452.

[116] U. Schumann. On conditions for contrail formation from aircraft exhausts. *Meteorologische Zeitschrift*, 5(1):4–23, 1996. doi: 10.1127/metz/5/1996/4.

[117] K. Wolf, N. Bellouin, and O. Boucher. Long-term upper-troposphere climatology of potential contrail occurrence over the paris area derived from radiosonde observations. *Atmospheric Chemistry and Physics*, 23:287–309, 2023. doi: 10.5194/acp-23-287-2023.

[118] H. Mannstein, P. Spichtinger, and K. Gierens. A note on how to avoid contrail cirrus. *Aviation, Space, and Environmental Medicine*, 10(5):421–426, 2005. doi: 10.1016/j.trd.2005.04.012.

[119] J. Sun and E. Roosenbrand. Fast contrail estimation with OpenSky data. *Journal of Open Aviation Science*, 1(2), 2023. doi: 10.59490/joas.2023.7264.

[120] U. Schumann. A contrail cirrus prediction model. *Geoscientific Model Development*, 5(3):543–580, 2012. doi: 10.5194/gmd-5-543-2012.

[121] V. B. Stephens, J. Bedwell, A. J. Josephson, K. Oldham, and D. O. Lignell. SootLib: A soot model library for combustion simulation. *SoftwareX*, 22:101375, 2023. doi: 10.1016/j.softx.2023.101375.

[122] R. Sausen and U. Schumann. Estimates of the climate response to aircraft CO_2 and NO_x emissions scenarios. *Climatic Change*, 44:27–58, 2000. doi: 10.1023/A:1005579306109.

[123] P.-J. Proesmans and R. Vos. Airplane design optimization for minimal global warming impact. *Journal of Aircraft*, 59(5), 2022. doi: 10.2514/1.C036529.

[124] R. Teoh, U. Schumann, C. Voigt, T. Schripp, M. Shapiro, Z. Engberg, J. Molloy, G. Koudis, and M. E. J. Stettler. Targeted use of sustainable aviation fuel to maximize climate benefits. *Environmental Science & Technology*, 56(23):17246–17255, 2022. doi: 10.1021/acs.est.2c05781.

[125] R. J. Millar, Z. R. Nicholls, P. Friedlingstein, and M. R. Allen. A modified impulse-response representation of the global near-surface air temperature and atmospheric concentration response to carbon dioxide emissions. *Atmospheric Chemistry and Physics*, 17:7213–7228, 2017. doi: 10.5194/acp-17-7213-2017.

[126] J. S. Fuglestvedt and T. Berntsen. A simple model for scenario studies of changes in climate, version 1.0. Technical Report CICERO-WP-1999/2, CICERO Center for International Climate and Environmental Research, 1999.

[127] R. B. Skeie, J. S. Fuglestvedt, T. Berntsen, G. P. Peters, R. Andrew, M. Allen, and S. Kallbekken. Perspective has a strong effect on the calculation of historical contributions to global warming. *Environmental Research Letters*, 12(2):024022, 2017. doi: 10.1088/1748-9326/aa5b0a.

[128] E. S. Dallara, I. M. Kroo, and I. A. Waitz. Metric for comparing lifetime average climate impact of aircraft. *AIAA Journal*, 49(8), 2011. doi: 10.2514/1.J050763.

[129] V. Grewe, C. Frömming, S. Matthes, S. Brinkop, M. Ponater, S. Dietmüller, P. Jöckel, H. Garny, E. Tsati, K. Dahlmann, O. A. Søvde, J. Fuglestvedt, T. K. Berntsen, K. P. Shine, E. A. Irvine, T. Champougny, and P. Hullah. Aircraft routing with minimal climate impact: The REACT4C climate cost function modelling approach (v1.0). *Geoscientific Model Development*, 7:175–201, 2014. doi: 10.5194/gmd-7-175-2014.

[130] E. S. Dallara. *Aircraft Design for Reduced Climate Impact*. PhD thesis, Stanford University, Stanford, CA, USA, 2011.

[131] V. Grewe and K. Dahlmann. How ambiguous are climate metrics? and are we prepared to assess and compare the climate impact of new air traffic technologies? *Atmospheric Environment*, 2015. doi: 10.1016/j.atmosenv.2015.02.039.

[132] D. P. Wells, B. L. Howard, and L. A. McCullers. The flight optimization system weights estimation method. Technical Report NASA/TM–2017–219627/Volume I, NASA Langley Research Center, 2017.

[133] M. Drela. TASOPT 2.00 transport aircraft system optimization technical description. Technical report, Massachusetts Institute of Technology, 2010.

[134] L. S. Nunez, J. C. Tai, and D. N. Mavris. The environmental design space: Modeling and performance updates. In *AIAA Scitech 2021 Forum*, January 2021. doi: 10.2514/6.2021-1422.

[135] T. W. Lukaczyk, A. D. Wendorff, M. Colonno, T. D. Economon, J. J. Alonso, T. H. Orra, and C. Ilario. SUAVE: An open-source environment for multi-fidelity conceptual vehicle design. In *16th AIAA/ISSMO Multidisciplinary Analysis and Optimization Conference*, Dallas, Texas, USA, June 2015. doi: 10.2514/6.2015-3087.

[136] E. M. Botero, M. A. Clarke, R. M. Erhard, J. T. Smart, J. J. Alonso, and A. Blaufox. Aerodynamic verification and validation of suave. In *AIAA SciTech 2022 Forum*, San Diego, California, USA, 2022. doi: 10.2514/6.2022-1929.

[137] D. Owens. Weissinger's model of the nonlinear lifting-line method for aircraft design. In *36th AIAA Aerospace Sciences Meeting and Exhibit*, Reno, Nevada, USA, January 1998. doi: 10.2514/6.1998-597.

[138] L. R. Miranda, R. D. Elliot, and W. M. Baker. A generalized vortex lattice method for subsonic and supersonic flow applications. Technical Report NASA-CR-2865, NASA, 1977.

[139] B. J. Cantwell. Fundamentals of compressible flow, 2022. URL `https://web.stanford.edu/~cantwell/AA210A_Course_Material/AA210A_Course_BOOK/AA210_Fundamentals_of_Compressible_Flow_BOOK_Brian_J_Cantwell_Jan_2022.pdf`. Accessed: 2026-04-28.

[140] John K. Lytle. The numerical propulsion system simulation: An overview. Technical Report NASA/TM-2000-209915, NASA Glenn Research Center, Cleveland, OH, USA, 2000.

[141] W. P. J. Visser and M. J. Broomhead. GSP, a generic object-oriented gas turbine simulation environment. In *ASME Turbo Expo 2000: Power for Land, Sea, and Air*, Munich, Germany, 2000. doi: 10.1115/2000-GT-0002.

[142] E. S. Hendricks and J. S. Gray. pyCycle: A tool for efficient optimization of gas turbine engine cycles. *Aerospace*, 6(8), 2019. doi: 10.3390/aerospace6080087.

[143] *GT-SUITE: Engine Performance Application Manual*. Gamma Technologies, 2018.

[144] Alexios Alexiou and T. Tsalavoutas. *Introduction to Gas Turbine Modelling with PROOSIS*. Empresarios Agrupados Internacional, 1st edition, 2011.

[145] S. Vannoy and C. P. Cadou. Development and validation of an NPSS model of a small turbojet engine. In *52nd AIAA/SAE/ASEE Joint Propulsion Conference*, Salt Lake City, Utah, USA, July 2016. doi: 10.2514/6.2016-5063.

[146] S. M. Jones. An introduction to thermodynamic performance analysis of aircraft gas turbine engine cycles using the numerical propulsion system simulation code. Technical Report NASA/TM—2007-214690, NASA, 2007.

[147] J. S. Schutte. *Simultaneous Multi-Design Point Approach to Gas Turbine On-Design Cycle Analysis for Aircraft Engines*. PhD thesis, Georgia Institute of Technology, Atlanta, GA, USA, 2009.

[148] E. S. Hendricks. Development of an open rotor cycle model in NPSS using a multi-design point approach. Technical Report NASA/TM-2011-217064, NASA Glenn Research Center, Cleveland, OH, USA, 2011.

[149] C. Perullo and D. N. Mavris. Assessment of vehicle performance using integrated NPSS hybrid electric propulsion models. In *50th AIAA/ASME/SAE/ASEE Joint Propulsion Conference*, Cleveland, Ohio, USA, July 2014. doi: 10.2514/6.2014-3489.

[150] David G Goodwin, Harry K Moffat, Ingmar Schoegl, Raymond L Speth, and Bryan W Weber. Cantera: An object-oriented software toolkit for chemical kinetics, thermodynamics, and transport processes, 2025.

[151] *CHEMKIN-Pro: Chemical Kinetics Simulation Software Documentation*. ANSYS Inc., 2022.

[152] A. Cuoci, A. Frassoldati, T. Faravelli, and E. Ranzi. OpenSMOKE++: An object-oriented framework for the numerical simulation of reactive systems with detailed kinetics. *Computer Physics Communications*, 192:237–264, 2015. doi: 10.1016/j.cpc.2015.02.014.

[153] *COSILAB: A Software Package for the Detailed Simulation of Combustion Processes*. Rotexo GmbH & Co. KG, 2022.

[154] *ANSYS Fluent: Combustion Modelling Capabilities*. ANSYS Inc., 2023.

[155] U. Schumann. Formation, properties and climatic effects of contrails. *Comptes Rendus Physique*, 6(4–5):549–565, 2005. doi: 10.1016/j.crhy.2005.05.002.

[156] J. Luche. *Obtention de modèles cinétiques réduits de combustion – Application à un mécanisme du kérosène*. PhD thesis, Université d'Orléans, 2003.

[157] S. Mohammadi, V.-H. Bui, W. Su, and B. Wang. Surrogate modeling for solving OPF: A review. *Sustainability*, 16(22):9851, 2024. doi: 10.3390/su16229851.

[158] J. Pelmatti, L. Brevault, M. Balesdent, and El-Ghazali Talbi. Mixed variable gaussian process-based surrogate modeling techniques: Application to aerospace design. *Journal of Aerospace Information Systems*, 18(11):813–837, 2021. doi: 10.2514/1.I010965.

[159] C. E. Rasmussen and C. K. I. Williams. *Gaussian Processes for Machine Learning*. MIT Press, 2006.

[160] I. Goodfellow, Y. Bengio, and A. Courville. *Deep Learning*. MIT Press, 2016.

[161] D. Samadian, I. B. Muhit, and N. Dawood. Application of data-driven surrogate models in structural engineering: A literature review. *Archives of Computational Methods in Engineering*, 32:735–784, 2024. doi: 10.1007/s11831-024-10152-0.

[162] P. Ren, C. Stuart, M. Zhang, R. Inomata, K. Nakamura, I. Morita, and S. Spence. Investigation of the surrogate model in an ANN–meanline hybrid model for radial turbine performance prediction. *Journal of Gas Turbines and Power*, 15(2):9–18, 2024. doi: 10.38036/jgpp.15.2_9.

[163] M. Austern and W. Zhou. Asymptotics of cross-validation. *Annales de l'Institut Henri Poincaré, Probabilités et Statistiques*, 61(4):2804–2865, 2025. doi: 10.1214/24-AIHP1488.

[164] Boeing Commercial Airplanes. Airport planning: 3-View drawings for boeing commercial aircraft, 2025. URL `https://www.boeing.com/commercial/airports/3-view`. Accessed: 2025-12-08.

[165] C. Brady. *The Boeing 737 Technical Guide*. Chris Brady, 2021.

[166] R. S. Shevell. *Fundamentals of Flight*. Prentice-Hall, 1st edition, 1983.

[167] S. J. Schneider. Analysis of turbine blade relative cooling flow factor used in the subroutine coolit based on film cooling correlations. Technical Report NASA/TM—2015-218738, NASA, 2015.

[168] CFM International. *Training Manual: LEAP-1B Engine Systems, Version 1.0, CTC-623 – Level 3*, 2017.

[169] R. P. Thacker and N. J. Blaesser. Modeling of a modern aircraft through calibration techniques. In *AIAA Aviation 2019 Forum*, Dallas, Texas, USA, June 2019. doi: 10.2514/6.2019-2984.

[170] Ryanair DAC. Our fleet, 2025. URL `https://corporate.ryanair.com/about-us/our-fleet/`. Accessed: 2025-12-10.

[171] Ryanair Holdings plc. Ryanair annual report 2023. Technical report, Ryanair Holdings plc, 2023.

[172] Energy Department of Climate and the Environment. National hydrogen strategy. Technical report, Government of Ireland, 2023.

[173] Flightradar24 AB. Flightradar24 live flight tracker – real-time flight tracker map, 2024. URL `https://www.flightradar24.com/data/airlines/fr-ryr/fleet`. Accessed: 2024-04-15.

[174] Y. Bicer and I. Dincer. Life cycle evaluation of hydrogen and other potential fuels for aircrafts. *International Journal of Hydrogen Energy*, 42(16):10722–10738, 2017. doi: 10.1016/j.ijhydene.2016.12.119.

[175] T. Weidner, V. Tulus, and G. Guillén-Gosálbez. Environmental sustainability assessment of large-scale hydrogen production using prospective life cycle analysis. *International Journal of Hydrogen Energy*, 48(22):8310–8327, 2023. doi: 10.1016/j.ijhydene.2022.11.044.

[176] E. C. M. Ruijgrok, E. J. van Druten, and B. H. Bulder. Cost evaluation of north sea offshore wind post 2030. Technical report, North Sea Wind Power Hub, 2019.

[177] N. Brazzola, A. Patt, and J. Wohland. Definitions and implications of climate-neutral aviation. *Nature Climate Change*, 12:761–767, 2022. doi: 10.1038/s41558-022-01404-7.